RICE UNIVERSITY

Functions of CML24:
A Potential Calcium Sensor of Arabidopsis

by

Yu-Chang Tsai

A THESIS SUBMITTED
IN PARTIAL FULFILLMENT OF THE
REQUIREMENTS FOR THE DEGREE

Doctor of Philosophy

APPROVED, THESIS COMMITTEE:

Janet Braam, Professor, Chair
Biochemistry and Cell Biology

Michael Gustin, Professor
Biochemistry and Cell Biology

Bonnie Bartel, Ralph and Dorothy
Looney Professor
Biochemistry and Cell Biology

James McNew, Associate Professor
Biochemistry and Cell Biology

Ramon Gonzalez, William W. Akers
Assistant Professor
Chemical and Biomolecular
Engineering

HOUSTON, TEXAS
April 2010

Abstract

Functions of CML24:
A Potential Calcium Sensor of Arabidopsis

by

Yu-Chang Tsai

Plants sense environmental conditions and respond by changing development and physiology. Calcium (Ca^{2+}) is a second messenger thought to play a critical role in plant responses to developmental and environmental stimuli. Calmodulin (CaM) is the prototypical Ca^{2+} sensor that is highly conserved among eukaryotes. The Arabidopsis genome encodes 50 CaM-like (CML) proteins in addition to CaM. CML functions remain largely unknown. *CML24* expression is strongly upregulated by diverse stimuli. The encoded protein shares characteristics with CaM, including primary sequence similarity, predicted tertiary structure, and Ca^{2+}-induced conformational change. Plants with epigenetically silenced *CML24* are delayed in the transition to flowering and have altered ion sensitivity.

To further understand CML24 function, I employed genetic, biochemical, cellular, and physiological approaches. Mass spectroscopy analyses suggest that CML24 cysteines may form disulfides; therefore, CML24 may have the capability of transducing oxidative, in addition to Ca^{2+}, signals. Apparent loss- and gain-of-function *cml24* point mutants were identified and determined to have alterations in the timing of flowering induction. Despite the physiological consequences of the cml24 mutant amino acid substitutions, the mutant proteins retain the ability to undergo Ca^{2+}-dependent conformational changes. *cml24* mutants are defective in expression of the

regulatory genes, *CONSTANS* and *FLOWERING LOCUS C* (*FLC*) and have aberrant nitric oxide (NO) accumulation. Altered NO levels underlie *FLC* enhanced expression in the late-flowering *cml24* mutants and contribute in part to delayed flowering. NO-associated 1 (NOA1), not arginine-dependent NO synthase or nitrate reductase, is implicated, through an indirect mechanism, in NO accumulation in *cml24* mutants. CML24 directly binds and may increase the enzymatic activity of Autophagy 4b (ATG4b), a cysteine protease that regulates autophagy, the cellular "self eating" process by which eukaryotic cells remove damaged and nonessential cytoplasmic components. Fluorescence imaging and western analysis of autophagy markers and seedling growth assays in response to nutrient-limitation indicate that the *cml24* mutants may have defects in autophagy regulation.

Together, this work implicates CML24 as a potential Ca^{2+} and redox sensor in the regulation of NO accumulation and, through direct interaction with ATG4b, in the regulation of autophagy progression.

Acknowledgements

I would like to express my appreciation to my mentor, Dr. Janet Braam for her professional guidance and support. She has taught me to think, present and write logically, even giving me the opportunity to compose my own research. Without her support and encouragement, these works would not be preceded and done.

I would like to thank the members of my committee, Drs. Michael Gustin, Bonnie Bartel, and James McNew for providing me with valuable suggestions. I thank Dr. Ramon Gonzalez for his willingness to serve on my committee.

I would like to thank the labs of Drs. Bartel, Bennett, Covington, Gustin, McNew, Shamoo, Silberg, Stern, and Wagner for the use of equipment that made this work possible.

I would like to thank my collaborators, Drs. Alex Webb (circadian rhythm analysis), Kendal Hirschi (amino acid analysis), David Salt (ionomics analysis), Dan Klessing (NOA1 interaction analysis), Pernilla Wittung-Stafshede, Erik Sedlák (CML24 protein stability analysis), and Olivier Lichtarge and Angela Wilkins (ET analysis) for helping on my research. I would like to thank Drs. Ohsumi and Bassham for providing ATG8 antibody and GFP-ATG8 transgenics, respectively.

I would like to thank previous and current Braam lab members. Thank you to Liz and Nikkí for helping on CaM and CML24 projects, even after you graduated. Thank you to Melissa and Luis for sharing your knowledge on microscopy and pathogen analysis. Thank you to Wassim, Se, Wang, and Bernadette for all the scientific and non-scientific conversations. Thank you to Kalie for making a joyful working environment.

I would like to thank Rice and BCM TSA friends for providing lots of entertainment after the stressful work. Thank you to Chun-jen for the all the conversations and sharing information.

I would like to thank my family for their support, especially my wife, Fu-Jung, for being companion all the time.

Financial support for this work was provided by the National Science Foundation (NSF MCB 0817976).

Table of contents

Chapter 1: Introduction 1
1.1 Calcium signaling and calcium sensors 1
1.1.1 Ca^{2+} as a signal 1
1.1.2 Ca^{2+} sensors 2
1.1.3 CML24 4
1.2 Transition to flowering regulation 7
1.2.1 Four pathways regulate transition to flowering in Arabidopsis 7
1.2.2 Nitric oxide: role in regulating the transition to flowering 9
1.3 NO biosynthesis and accumulation 10
1.3.1 NO synthases in animals 10
1.3.2 NO synthesis in plants 10
1.4 Autophagy 13
1.4.1 Autophagy overview 13
1.4.2 Autophagy regulation 14
1.4.3 Autophagy in plants 15
1.4.4 The role of ATG4 and ATG8 in autophagy 15
Chapter 2: Materials and Methods 22
2.1 Plant material and growth conditions 22
2.1.1 Manipulation of nitrogen source in the culture media 22
2.2 Phenotype characterization 23
2.2.1 Analysis of transition to flowering 23
2.2.2 Analysis of nitric oxide accumulation 23
2.2.3 Amino acid analysis sample preparation 24
2.2.4 Analysis of Inductively Coupled Plasma-Mass Spectroscopy (ICP-MS) ... 24
2.2.5 Analysis of root length 26
2.3 Genetic analysis 26
2.3.1 Identification of T-DNA insertion plants 26
2.3.2 Identification of *cml24* point mutants 26
2.3.4 Double mutant generation and identification 29
2.3.5 Plant DNA isolation 29
2.3.6 Plant RNA isolation 29
2.3.7 Reverse transcription (RT) 30
2.3.8 Quantitative RT-PCR (Q-PCR) 30
2.4 Protein manipulations 32
2.4.1 Protein extraction and quantification 32
2.4.2 CML24, cml24-2, and cml24-4 protein generation and purification 33
2.4.3 GST-ATG4b protein generation and purification 34
2.4.4 His-ATG8e-HA protein generation and purification 35
2.4.5 Ca^{2+}-induced mobility shift 36
2.4.6 GST pull-down analysis 37
2.4.7 ATG8a antibody purification 37
2.4.8 ATG8e antibody generation and purification 39

2.4.9 *In vitro* ATG4 activity analysis 41
2.4.10 Nitrate reductase activity analysis 42
2.4.11 Western blot analysis 43
2.4.12 MALDI-TOF mass spectroscopy 44
2.5 Fluorescence microscopy 45
2.5.1 GFP-ATG8e green fluorescent protein visualization 45
2.5.2 Monodansylcadaverine staining and visualization 45
Chapter 3: Arabidopsis Potential Calcium Sensors Regulate Nitric Oxide Levels and Transition to Flowering 47
3.1 *CML24* regulates the transition to flowering 49
3.1.1 *CML24* is required for photoperiod regulation of the transition to flowering 49
3.1.2 *CML23* contributes to flowering regulation under long days 53
3.1.3 Double mutants of *cml23* and *cml24* are defective in the autonomous pathway 53
3.1.4 *cml23* and *cml24* mutations affect *CO* and *FLC* transcript levels 53
3.1.5 The *cml24* late flowering mutants accumulate elevated nitric oxide (NO) . 60
3.2 Amino acid content in the *cml* mutants 64
3.2.1 Free arginine levels in *cml* mutants do not correlate with NO accumulation 64
3.2.2 *cml24* mutants accumulate cystine 66
3.2.3 *cml24* mutants have altered threonine levels 67
3.3 Ionomics analysis 69
3.4 Conclusion 69
Chapter 4: *CML24*: Role in NO Accumulation 71
4.1 *CML24* and putative *NOS/NOA1* pathway 71
4.2 *CML24* and *NOA1* pathway 72
4.2.1 *CML24* and mitochondrial/chloroplast NO production pathway 75
4.3 CML24 and Nitrate Reductase 76
4.3.1 The *cml24* mutants do not have alter *NIA1* and *NIA2* transcript levels 78
4.3.2 The *cml24* mutants do not have altered nitrate reductase activity levels 78
4.4 Conclusion 80
Chapter 5: Biochemical Analysis of CML24 82
5.1 CML24 structure 82
5.1.1 CML24 changes conformation upon Ca^{2+} binding 85
5.1.2 CML24 can form a disulfide bond 88
5.1.3 CML24 protein stability 99
5.2 CML24-ATG4 interactions 99
5.2.1 ATG4b identified as a CML24 interaction partner in yeast two hybrid screen 100
5.2.2 CML24 is pulled down with GST-ATG4b 100
5.2.2 Mutated cml24 proteins interact with GST-ATG4b 104
5.2.3 CaM does not bind ATG4b-GST 105
5.2.4 Evolutionary trace analysis of ATG4b 105
5.3 Conclusion 107
Chapter 6: CML24 and Autophagy Regulation 109

6.1 CML24 effects on ATG4b activity 109
6.1.1 CML24 effects on recombinant ATG4b activity *in vitro* 109
6.1.2 *cml24* mutant tissue extracts have altered His-ATG8e-HA activity..... 118
6.2 Monitoring autophagy in *cml24* mutants with fluorescence imaging..... 121
6.2.1 The *cml24* mutants have altered monodansylcadaverine fluorescence 122
6.2.2 GFP-ATG8e fluorescence analysis..... 127
6.3 The *cml24* mutants have altered ATG8 protein accumulation 136
6.3.1 The *cml24* mutants have altered endogenous ATG8 accumulation levels 137
6.3.2 The *cml24* mutants show altered GFP-ATG8e accumulation patterns..... 142
6.4 *cml24* mutants have aberrant root elongation 146
6.5 Conclusion 149
Chapter 7: Discussion and Future Perspectives 153

Figures and Tables

Fig 1.1 CML23 and CML24 are calmodulin-like proteins 3
Fig 1.2 Output image from the BAR Cell eFP Browser shows the predicted subcellular localization of CML23 and CML24 6
Fig 1.3 Four pathways regulate the transition to Flowering: photoperiod, autonomous, vernalization, and GA 8
Fig 1.4 Schematic of NO accumulation in plant cells 11
Fig 1.5 Schematic of yeast ATG4 and ATG8 roles in autophagy progression 16
Fig 1.6 Amino acid sequence alignment and phylogenic tree of ATG8s 17
Fig 1.7 Genevestigator reported *ATG8* expression patterns obtained from Arabidopsis microarray experiments 20
Fig 1.8 Plant ATG4 proteins lack the analogous oxidation-sensitive Cys78 of human ATG4 and have an additional CaM-binding motif 21
Table 2.1 The formula of different growth media 25
Table 2.2 SALK T-DNA insertion mutation and *cml24* point mutants identification 27
Table 2.3 Q-PCR primers list 31
Fig. 2.1 ATG8a antibody purification 38
Fig. 2.2 Anti-ATG8e sera reaction with plant extract proteins 40
Table 3.1 *cml24* point mutations and mutant flowering phenotype 48
Fig 3.1 *CML23* and *CML24* are required for appropriate timing of the transition to flowering 50
Fig 3.2 The *cml24-2* mutation is dominant with respect to time to flowering transition 52
Fig 3.3 Four pathways regulate the transition to flowering: photoperiod, autonomous, vernalization, and gibberellin (GA) 54
Fig 3.4 Regulation of flowering time gene expression in *cml* mutants 55
Fig 3.5 Regulation of flowering time gene expression in *cml* mutants 59
Fig 3.6 *CML23* and *CML24* regulate NO accumulation in leaves and the altered NO levels are responsible for elevated *FLC* transcript levels 61
Fig 3.7 Exogenous NO scavenger (cPTIO) and NO donor (SNP) affect Col-0 and *cml23/cml24* double mutants flowering time in short photoperiods 63
Fig 3.8 Arg, Cys2, and Thr amino acid content in wild type (Col-0) and *cml* mutants 65

Fig 3.9 Aspartate-derived amino acids biosynthesis and degradation 68
Fig 4.1 L-NMMA does not repress NO accumulation 73
Fig 4.2 NOA1 is required for NO accumulation but is dispensable for the delay of flowering caused by *cml24-4* 74
Fig 4.3 β-ATPase protein accumulation levels in wild type, *cml24* and *noa1* 77
Fig 4.4 *NIA* transcript and nitrate reductase activity analysis in wild type and *cml* mutants 79
Fig 5.1 Multiple alignment and phylogenetic analysis of CML24 homologous protein in other plant species 83,84
Fig 5.2 Comparison of wild-type and mutant CML24 isoform migration in SDS-PAGE 86
Fig 5.3 Assessment of the number of reduced Cys in recombinant CML24 proteins 89
Table 5.1 Predicted trypsin digestion fragments of CML24 90
Fig 5.4 Prediction of CML24 three-dimensional structure 91
Fig 5.5 MALDI-TOF-MS analysis of trypsin-digested CML24 protein 93
Fig 5.6 MALDI-TOF-MS analysis of trypsin-digested CML24 protein 95
Fig 5.7 CML24 has potential to form multimers 97
Fig 5.8 Unfolding of CML24 monitored by CD at 220nm 98
Fig 5.9 Purified GST and GST-ATG4b protein 101
Fig 5.10 CML24 binds GST-ATG4b *in vitro* independent of calcium 102
Fig 5.11 Plant ATG4 proteins lack the analogous oxidation-sensitive Cys78 of human ATG4 and have an additional CaM-binding motif 103
Fig 5.12 Evolutionary trace analysis of plant ATG4b 106
Fig 6.1 His-ATG8e-HA protein purification 110
Fig 6.2 ATG4b activity *in vitro* 112
Fig 6.3 Effect of temperature on ATG4b cysteine protease activity *in vitro* 113
Fig 6.4 Addition of CML24 to test effects on ATG4b in vitro activity on His-ATG8e-HA substrate 115
Fig 6.5 CML24 may enhances ATG4b activity 117
Fig 6.6 The *cml24* mutant extracts may have altered ATG4 activity assayed as His-ATG8-HA cleavage *in vitro* 119

Fig 6.7 MDC staining of the root tips of wild type (Col-0), *cml24-2*, *cml24-4*, and *atg7-1* 123
Fig 6.8 MDC staining of the root tips and mature root cells of wild type (Col-0), *cml24-2*, *cml24-4*, and *atg7-1* 125
Fig 6.9 MDC staining of the root tips of wild type (RLD) and *CML24* overexpressing (*O1*) and underexpressing (*U1*) transgenics 128
Fig 6.10 Effect of darkness on behavior of GFP-ATG8e fluorescence in stably transformed roots 130
Fig 6.11 GFP-ATG8e fluorescence of darkness and nitrogen depleted treated mature root cells 133
Fig 6.12 GFP-ATG8e fluorescence in control (0h) and nitrogen depleted and autophagy inhibitor, E64d, treated roots (12h) 135
Fig 6.13 ATG8 protein accumulation in Col-0, *cml24-2*, *cml24-4*, and *atg4a4b* 138
Fig 6.14 ATG8a protein accumulation in short photoperiod growth Col, *cml24-2*, *cml24-4*, and *atg4a4b* 141
Fig 6.15 GFP-ATG8e accumulation in plants transferred to nitrogen-depleted media ... 144
Fig 6.16 *cml24* and *atg4a4b* mutants have abnormal root growth in response to nitrogen and carbon availability media 148
Fig 7.1 A proposed model for the function of CML24 154
Appendix A1 Amino acid content in wild type and *cml* mutants 171
Appendix A2 Ion Accumulations in *cml23* and *cml24* mutants 172

Abbreviations

abscisic acid	ABA
acetonitrile	ACN
Asparagine	Asn
Aspartate	Asp
autophagy-related	ATG
Arabidpsos nitric oxide synthase1	*Atnos1*
calcium	Ca^{2+}
calmodulin	CaM
cauliflower mosaic virus	*CaMV*
circular dichroism	CD
CaM-like	*CML*
CONSTANS	*CO*
Arabidopsis thaliana Ecotype Columbia-0	Col-0
Concanamycin A	ConA
2-(4-carboxyphenyl)-4,4,5,5-tetramethylimidazoline-1-oxyl-3-oxide	cPTIO
Cysteine	Cys
cystine	Cys2
4-amino-5-methylamino-2',7'-difluorofluorescein diacetate	DAF-FM DA
Diethylpyrocarbonate	DEPC
diothiothreitol	DTT
(2S,3S)-trans-Epoxysuccinyl-L-leucylamido-3-methylbutane ethyl ester	E64d
ethylenediaminetetraacetic acid	EDTA
electronic fluorescent pictograph	eFP
ethyleneglycotetraacetic acid	EGTA
Enzyme-linked immunosorbant assay	ELISA
ethylmethanesulfonate	EMS
endothelial NOS	eNOS
Electron paramagnetic resonance	EPR
Expressed sequence tag	EST
evolutionary trace	ET
ethanol	EtOH
N,N'-di(2-hydroxybenzyl) ethylenediamine-N,N'-diacetic acid monohydro-chloride hydrate	Fe-HBED
FLAVIN-BINDING, KELCH REPEAT, F-BOX	*FKF1*
Flowering Locus C	*FLC*
FRIGIDA	*FRI*
Flowering Locus T	*FT*
gibberellin	GA
growth controlled by abscisic acid2	*gca2*

Green Fluorescence Protein	GFP
GIGANTEA	*GI*
class 1 non-symbiotic hemoglobin	*GLB1*
class 2 non-symbiotic hemoglobin	*GLB2*
Glutamic acid	Glu
Glycine	Gly
glutathione	GSH
glutathione S-transferase	GST
Guanosine triphosphate	GTP
β-glucuronidase	GUS
hydrogen peroxide	H_2O_2
Hemagluttinin	HA
hydrochloric acid	HCl
histidine	His
High performance liquid chromatography	HPLC
horseradish peroxidase	HRP
Heat Shock protein Cognate 70	HSC70
iodoacetamide	IAM
Inductively Coupled Plasma-Mass Spectroscopy	ICP-MS
isoleucine	Ile
inducible NOS	iNOS
isopropyl 1-thio-b-D-galactopyanoside	IPTG
LUMINIDEPENDENS	*LD*
lithium dodecyl sulfate	LDS
Nω-Nitro-L-arginine methyl ester hydrochloride	L-NAME
N^G-monomethyl-L-arginine monoacetate	L-NMMA
Nω-Nitro-L-arginine	L-NNA
Lysine	Lys
Matrix-assisted laser desorption/ionization Time-of-flight mass spectrometry	MALDI-TOF
monodansylcadaverine	MDC
2-(*N*-morpholino) ethanesulphonic acid	MES
Methionine	Met
Murashige and Skoog	MS
nicotinamide adenine dinucleotide phosphate (reduced)	NADPH
Sodium Hydroxide	NaOH
Nitrate Reductase	*NIA1, NIA2*
Neuronal NOS	nNOS
Nitric Oxide	NO
NO-Associated 1	NOA1

NO synthase	NOS
nitric oxide overproducer1	*nox1*
Activated NR	NR_{act}
Total NR	NR_{max}
CML24 overexpressing	*O1*
Polyacrylamide Gel Electrophoresis	PAGE
Phosphate-Buffered Saline	PBS
Polymerase Chain Reaction	PCR
Phosphatidyl-Ethanolamine	PE
PHOTOPERIOD-INDEPENDENT EARLY FLOWERING 1	*PIE1*
Purdue Ionomics Information Management System	PiiMS
Ras-cAMP-dependent protein kinase A	PKA
Phenylmethylsulfonyl fluoride	PMSF
Plant nutrient	PN
Plant nutrient with 0.5% sucrose	PNS
Parts Per Million	PPM
Plant nutrient without nitrogen with 0.5% sucrose	PS
Quantitative real-time PCR	Q-PCR
Ras-related small GTPase	Rag
Rap1 interacting factor 1 homolog	RIF1
Arabidopsis thaliana Ecotype RLD	RLD
Reactive Oxygen Species	ROS
Reverse transcription	RT
Sinapinic Acid	SA
S-Adenosylmethionine	SAM
sodium dodecyl sulfate	SDS
Sodium Nitroprusside	SNP
Suppressor of Overexpression of Constans1	*SOC1*
Subcellular location database of Arabidopsis	SUBA
Tris, acetate, EDTA	TAE
Tris Buffered Saline	TBS
Transfer DNA	T-DNA
Transmission Electron Microscopy	TEM
Trifluoro acetic acid	TFA
Threonine	Thr
Targeting Induced Local Lesions in Genomes	TILLING
Target of Rapamycin	TOR
Tris hydroxymethylaminoethane	Tris
CML24 underexpressing transgenics	*U1, U2*
VERNALIZATION INSENSITIVE 3	*VIN3*

VERNALIZATION1	*VRN1*
Wild Type	WT
Yeast extract, Tryptone media	YT

Chapter 1: Introduction

Plants are nonmotile yet thrive in diverse environments. Plants sense local environmental conditions and can undergo physiological changes that enable adaption. Upon stresses such as drought, flooding, light, temperature, wounding, touch, and biotic stresses, plants use different strategies to perceive and respond to them. Knowledge of how plants respond to different environmental stimuli would likely have practical application toward improvement in agricultural practices. Stress-induced calcium (Ca^{2+}) signaling is critical in triggering plant, as well as animal, cell responses. How Ca^{2+} signals are sensed and the mechanisms by which they induce cellular changes remain incompletely understood. I used reverse genetics, biochemistry, and cell biological approaches to shed light on the functions of one Ca^{2+} sensor protein, CML24, in Arabidopsis. This work reveals that this Ca^{2+} sensor functions in diverse aspects of plant physiology, including regulation of the transition to flowering, nitric oxide (NO) accumulation, and autophagy.

1.1 Calcium signaling and calcium sensors

1.1.1 Ca^{2+} as a signal

Stimulus-induced increases in cytosolic Ca^{2+} have been implicated in regulating plant growth, development, and responses to environmental stimuli (Reed et al., 1993; Yang and Poovaiah, 2003). Changes in Ca^{2+} levels may also regulate intracellular processes, including polarized growth, cell division, vesicle trafficking and fusion, and gene expression (Clapham, 1995; Cyert, 2001; Reddy, 2001). In unstimulated plant cells, the cytosolic Ca^{2+} concentration is in the nanomolar range. Cytosolic Ca^{2+} levels can rise to micromolar levels after cellular stimulation (Bootman and Berridge, 1995). Elevated

cytosolic Ca^{2+} occurs only transiently because high levels of Ca^{2+} could cause precipitation of cellular phosphate necessary for energy metabolism (Sze et al., 2000). Cytosolic Ca^{2+} increases occur through regulated influx from extracellular sources or intracellular stores. Resulting cytosolic Ca^{2+} increases can vary in frequency, amplitude, location, and source. These characteristics are thought to contribute to the Ca^{2+} "signature" and may confer specificity of the cellular responses. However, it remains unclear how Ca^{2+} signals are perceived in plant cells and how perception leads to appropriate cellular responses.

1.1.2 Ca^{2+} sensors

Cytosolic Ca^{2+} levels are likely perceived by Ca^{2+}-binding proteins (Kim et al., 2009). There are four classes of Ca^{2+}-binding proteins: (I) Calmodulins (CaM) with four EF hand Ca^{2+}-binding domains, (II) CaM-like (CML) proteins, which share significant sequence similarity with CaM but may differ in EF hand number, (III) Ca^{2+}-binding proteins that do not contain EF hands, and (IV) Ca^{2+}-dependent protein kinases, which are found only in plants and protozoa (Day et al., 2002; Reddy, 2001; Reddy et al., 2002).

In the Arabidopsis genome, there are ~232 genes encoding putative Ca^{2+}-binding proteins (Day et al., 2002). Seven genes encode CaM and 50 encode CML proteins (McCormack and Braam, 2003).

CaM is a highly conserved acidic 17 kDa protein of 148 amino acids (Figure 1.1) that is ubiquitous in eukaryotes. CaM contains two pairs of helix-loop-helix Ca^{2+}-binding domains connected by an alpha helix linker region (McCormack et al., 2005).

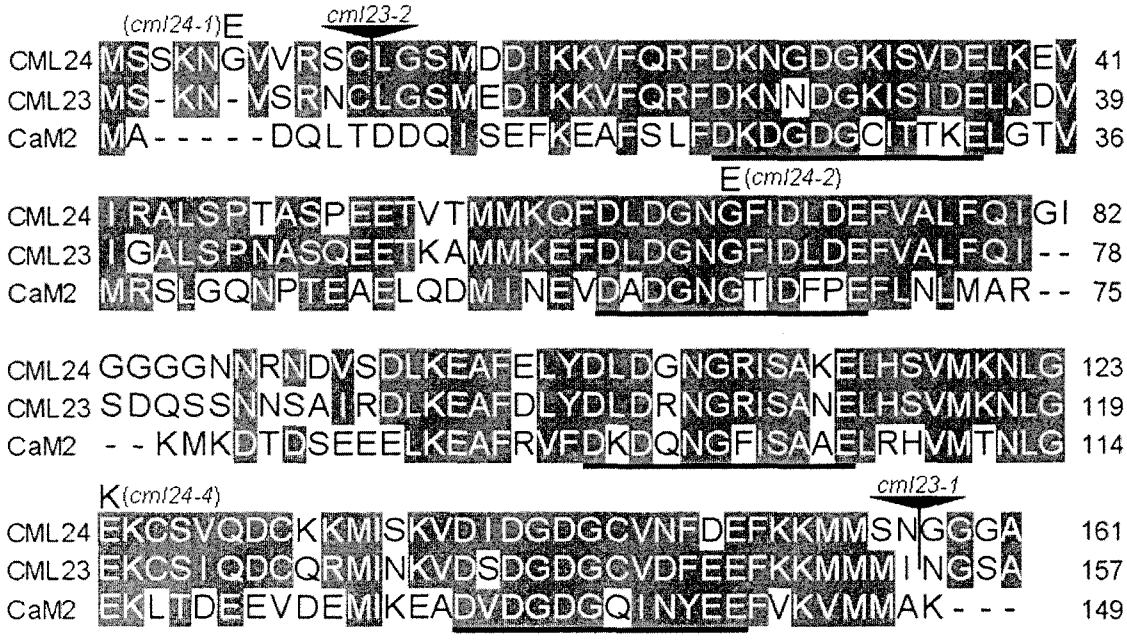

Fig 1.1 CML23 and CML24 are calmodulin-like proteins. Amino acid sequence alignment of Arabidopsis CML24 (At5g37770), CML23 (At1g66400), and one of the calmodulins, CaM2 (At2g41110). Shaded amino acids indicate sequence similarity, underlines delineate EF-hand Ca^{2+} binding loops, letters above the CML24 sequence indicate the amino acid substitutions in the *cml24-1*, *cml24-2*, and *cml24-4* mutants, the solid triangles indicate the two independent insertion sites of the T-DNA insertions in *CML23*. Amino acid numbers are on the right.

Despite the central role proposed for Ca^{2+} signaling in plant biology and the identification of the large number of potential Ca^{2+} sensors, functional studies have been reported for only a few *CMLs*. *cml42* mutants have abnormal trichome branching (Dobney et al., 2009), whereas overexpression of *CML43* accelerates the plant immune response to bacterial pathogens (Chiasson et al., 2005). CML19 (CENTRIN2) plays a role in homologous recombination and nucleotide excision repair in Arabidopsis (Liang et al., 2006; Molinier et al., 2004). A high throughput protein microarray approach to identify CaM and CML target proteins revealed that binding partners may be largely specific to one or a few CaMs/CMLs (Popescu et al., 2007a; Popescu et al., 2007b).

1.1.3 CML24

CML24 shares 44% amino acid identity with CaM and has 4 EF hands (Braam and Davis, 1990; Khan et al., 1997) (Figure 1.1). Like CaM, CML24 binds Ca^{2+} and undergoes Ca^{2+}-dependent changes in conformation (Delk et al., 2005). In addition, in the presence of Ca^{2+}, CML24 exposes hydrophobic domains similarly to CaM (Delk et al., 2005). Therefore, CML24 has characteristics of a CaM-related Ca^{2+} sensor. Northern analysis and quantitative real-time PCR (Q-PCR) indicate that *CML24* mRNA accumulates after heat shock, touch, wounding, dark, cold, H_2O_2, abscisic acid (ABA), and auxin (Braam, 1992; Braam and Davis, 1990; Delk et al., 2005; Polisensky and Braam, 1996). The Arabidopsis electronic fluorescent pictograph (eFP) based on microarray data reports similar *CML24* expression characteristics (Winter et al., 2007). Heat and cold shock induction of *CML24* expression is blocked in the presence of a Ca^{2+} chelator (Braam, 1992; Polisensky and Braam, 1996), suggesting that Ca^{2+} increases are necessary for inducing *CML24* expression, at least by temperature shocks.

A *CML24 GUS* transgenic (*CML24::GUS*) reported expression in tissues and organs undergoing growth, vascular tissue, floral organs, stomata, trichomes, and hydathodes (Delk et al., 2005). Transgenic plants with epigenetically silenced *CML24* have higher growth tolerance to exogenous $CoCl_2$, $MgCl_2$, $ZnSO_4$, and Na_2MoO_4 than wild type (Delk et al., 2005). These *CML24*-underexpressing transgenics are also less sensitive to ABA inhibition of germination and seedling growth (Delk et al., 2005). In long-day photoperiods, *CML24*-underexpressing transgenics are delayed in the transition to flowering relative to wild type (Delk et al., 2005). These results indicate that CML24 is critical for diverse aspects of plant physiology. However, the biochemical and cellular functions of CML24 remain unknown.

CML24's closest paralog, CML23, shares 78% amino acid identity with CML24 and also contains 4 EF hands (Figure 1.1). Based on Q-PCR and *CML23::GUS* transgenic analysis, *CML23* expression patterns are similar to those of *CML24*, but *CML23* transcripts accumulate to only about 7% the level of *CML24* mRNA (Delk et al., 2005).

The subcellular location database of Arabidopsis proteins (SUBA) (Heazlewood et al., 2007) reports that CML24 may localize on plasma membrane, based on mass spectroscopy analysis (Benschop et al., 2007). In addition, primary sequence analysis predicts that CML24 may localize in the cytosol, mitochondria, and nucleus (SUBA, Figure 1.2). The sequence-based predicted localization of CML23 is very similar to that of CML24, except that CML23 is also predicted to be in the chloroplast (Figure 1.2). The strong amino acid sequence conservation between CML23 and CML24, similar expression characteristics (Delk et al., 2005; Tsai et al., 2007), and protein localization

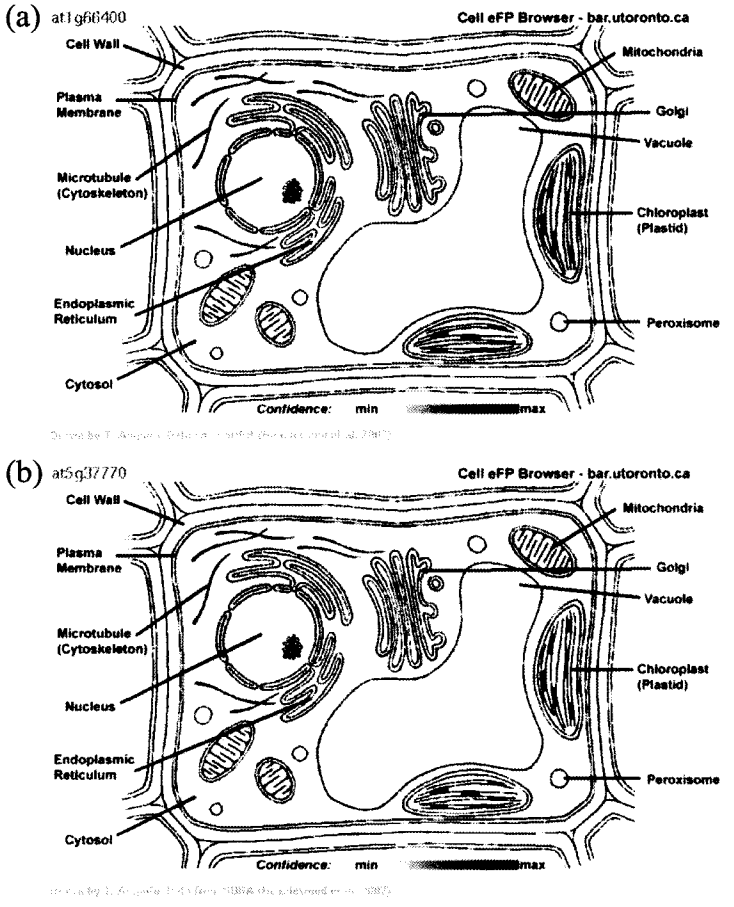

Fig 1.2 Output image from the BAR Cell eFP Browser shows the predicted subcellular localization of CML23 (a) and CML24 (b). (a) CML23 is predicted to be in the cytosol, nucleus, chloroplast, and mitochondria based on primary amino acid sequence motifs. (b) CML24 is localized on the plasma membrane by mass spectroscopy analysis and in the cytosol, nucleus, and mitochondria by primary amino acid sequence prediction. The color intensity indicates the confidence of the prediction. www.bar.utoronto.ca (Heazlewood et al., 2007).

predictions lead to the hypothesis that CML23 and CML24 may share overlapping functions.

1.2 Transition to flowering regulation

1.2.1 Four pathways regulate transition to flowering in Arabidopsis

Flowering is the developmental turning point from the vegetative to the reproductive phase. The induction of flowering is critical for plant reproductive strategy and redistribution of nutrients. The transition to flowering is regulated by four major pathways: long-day photoperiod, autonomous, vernalization (or extended cold), and gibberellin (GA) pathways (Figure 1.3) (Jack, 2004; Putterill et al., 2004). Changes in cytosolic Ca^{2+} may play roles in at least a subset of these regulatory pathways because light, circadian rhythms, low temperatures, and GA are stimuli that affect cytosolic Ca^{2+} levels (Baum et al., 1999; Dodd et al., 2005; Gilroy, 1996; Love et al., 2004; Polisensky and Braam, 1996).

Long days (>16-hours of light) accelerate the timing of the transition to flowering of Arabidopsis. The coincidence of *CONSTANS* (*CO*) RNA accumulation late in the day controlled by the circadian clock and light-stabilization of CO protein that occurs only in long days leads to functional CO promotion of flowering (Koornneef et al., 1991; Moon et al., 2003; Reed et al., 1993; Valverde et al., 2004). CO induces *Flowering Locus T* (*FT*) and *Suppressor of Overexpression of Constans1* (*SOC1*) transcription. FT and SOC1 act positively to drive the transition to flowering. *FT* and *SOC1* are negatively regulated by *Flowering Locus C* (*FLC*). *FLC* expression is inhibited by activation of the autonomous and vernalization pathways. Autonomous pathway mutants transition to flowering later

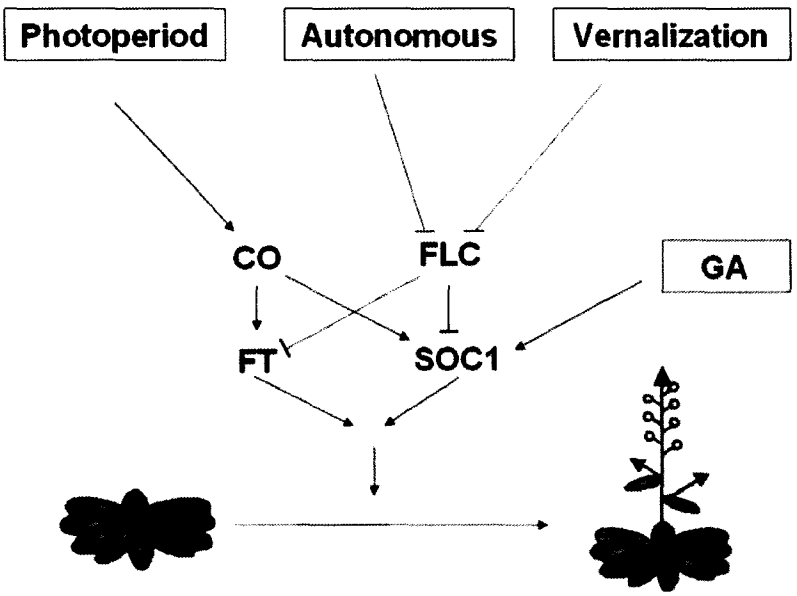

Fig 1.3 Four pathways regulate the transition to flowering: photoperiod, autonomous, vernalization, and GA. Four major genes, *CO*, *FT*, *SOC1*, and *FLC* are controlled by the different pathways and mediate the timing of the transition to flowering in Arabidopsis.

than wild type. A long period of low temperature vernalization also promotes flowering.

In addition, *SOC1* can be up-regulated by GA. GA biosynthesis mutants are delayed in the transition to flowering compared to wild type in short days (Moon et al., 2003; Wilson et al., 1992).

1.2.2 Nitric oxide: role in regulating the transition to flowering

Increased nitric oxide (NO) accumulation correlates with a delay in the transition to flowering, whereas reduced NO correlates with early flowering. An NO overproducing mutant (*nox1*), which has a defective chloroplast phosphoenolpryuvate/phosphate translocator gene, displays a delay in the transition to flowering relative to wild type (He et al., 2004a). In addition, exogenous NO provided by an NO donor, sodium nitroprusside (SNP), inhibits flowering and promotes vegetative growth (He et al., 2004b). In contrast, the *noa1* mutant, which under some conditions accumulates low NO, flowers earlier than wild type (Guo et al., 2003). Enhanced scavenging of NO by overexpression of non-symbiotic hemoglobins (*GLB1*, *GLB2*) (Hebelstrup and Østergaard-Jensen, 2008) causes an earlier transition to flowering relative to wild type. Conversely, transgenic plants with silenced *GLB1* expression are delayed in flowering time (Hebelstrup and Østergaard-Jensen, 2008). Reduced *GLB1* expression also causes the appearance of aerial rosettes on lateral meristems of the inflorescence, or flowering stem (Hebelstrup and Østergaard-Jensen, 2008).

NO represses Arabidopsis flowering by altering flowering gene expression. Photoperiod pathway genes, *CO* and *LFY,* are down regulated in *nox1,* delaying the transition to flowering (He et al., 2004a). NO also promotes expression of *FLC*, consistent with a delay in flowering. Reduced accumulation of NO in *noa1* correlates

with higher *LFY* and *CO* transcript levels and lower *FLC* transcript levels than wild type (He et al., 2004a). Flowering time of *nox1* is not accelerated by GA application; therefore, *nox1* and NO may regulate Arabidopsis transition to flowering independently of GA.

1.3 NO biosynthesis and accumulation

1.3.1 NO synthases in animals

NO is synthesized by three different NO synthase (NOS) isoforms, neuronal NOS (nNOS), endothelial NOS (eNOS), and inducible NOS (iNOS), in animals (Alderton et al., 2001). NOS catalyzes the conversion of L-arginine to NO and citrulline. nNOS and eNOS have CaM-binding domains and require Ca^{2+}/CaM-binding for NO production. (Alderton et al., 2001; Stuehr et al., 2004). iNOS tightly binds to CaM and is insensitive to intracellular Ca^{2+} fluctuations. To study NOS functions, several non-selective L-arginine analogs (L-NMMA, L-NAME, and L-NNA) have been widely used to inhibit NOS activity (Young et al., 2000).

1.3.2 NO synthesis in plants

To date, no gene or protein with significant sequence similarity to the animal NO synthases have been found in Arabidopsis. The documentation of NO accumulation leads to the outstanding question of how NO is produced in plant cells. There are two major proposed enzymatic pathways for NO production in plants (Figure 1.4). Both NO-Associated 1 (NOA1) and nitrate reductase have been implicated in NO production pathways.

NOA1 in Arabidopsis was identified by similarity to a snail protein required for snail NO synthesis (Guo et al., 2003; Huang et al., 1997). *noa1* mutants are reported to be

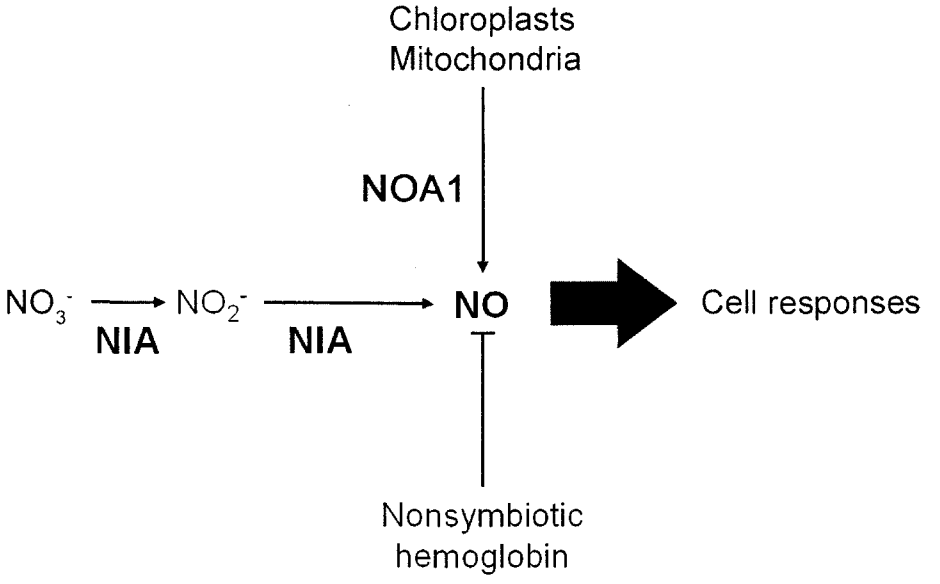

Fig 1.4 Schematic of NO accumulation in plant cells. NO can be produced from mitochondria, chloroplasts, or nitrate/nitrite by NOA1 or nitrate reductase (encoded by *NIA* genes). Nonsymbiotic hemoglobin acts as a NO scavenger. Adapted from (Lamotte et al., 2005)

defective in NO production and accumulate only about 20% the NO level found in wild type under some conditions. However, H_2O_2, indole-3-butyric acid, and zeatin induced NO levels in *noa1* are similar to those of wild type (Arnaud et al., 2006; Bright et al., 2006; Tun et al., 2008). Originally, some data indicated that NOA1 may be in mitochondria (Guo and Crawford, 2005; Zemojtel et al., 2006a; Zemojtel et al., 2006b). However, more recently NOA1, also called RIF1, was localized to chloroplasts (Flores-Pérez et al., 2008). NOA1 also has been localized in diatom chloroplasts, and higher NO production occurs in NOA1-overexpressing transgenic diatoms (Vardi et al., 2008). NOA1 contains a GTP-binding domain, has GTPase activity, and an additional C-terminal RNA-binding domain essential for complementing the *noa1* phenotype (Moreau et al., 2008; Sudhamsu et al., 2008). *rif1-1* has also been identified as a *NOA1* allele. *rif1-1* has defects in chloroplast structure and function (Flores-Pérez et al., 2008). Although recombinant NOA1 was originally reported to have NO synthase activity *in vitro* (Guo et al., 2003), the data are not reproducible (Crawford et al., 2006). The physiological functions of NOA1 and its role in nitric oxide accumulation are still unclear.

NO production in plants may also derive from nitrate reductase activity (Yamasaki and Sakihama, 2000). The major function of nitrate reductase is nitrogen assimilation with a role in converting nitrate to nitrite (Figure 1.4). Nitrite can be converted to NO by various mechanisms. When nitrite accumulates to high levels, nitrate reductase itself can catalyze one electron reduction of nitrite using NAD(P)H as an electron donor to produce NO. Nitrite accumulation and consequent NO production occurs during hypoxia in the dark with nitrate-fertilized plants (Rockel et al., 2002). In Arabidopsis, nitrate reductase is encoded by two genes, *NIA1* and *NIA2* (Wilkinson and

Crawford, 1993). Although NIA1 only contributes 10% of the nitrate reductase enzyme activity, NIA1 is required for NO production in guard cells (Bright et al., 2006). Nitrate reductase-dependent NO synthesis also plays a role in cold tolerance in Arabidopsis (Zhao et al., 2009). *nia1nia2* double mutants have less cold tolerance and accumulate lower NO levels than wild type and *noa1* (Zhao et al., 2009).

Mitochondria and chloroplasts are also reported sources of NO production in plants (Jasid et al., 2006; Planchet et al., 2005). In tobacco leaves and suspension cells, mitochondrial electron transport is the major electron donor for reduction of nitrite to NO (Planchet et al., 2005). Electron paramagnetic resonance (EPR)-detected NO production occurs in soybean chloroplasts supplied with nitrite or L-arginine (Jasid et al., 2006). The NO production can be blocked by adding a photosynthetic electron transport inhibitor or L-arginine analogs (Jasid et al., 2006). These results indicate that nitrite can be converted to NO in mitochondria and chloroplasts. However, which protein(s) participate in the conversion remains unclear.

1.4 Autophagy

1.4.1 Autophagy overview

Autophagy is a cellular degradation process that removes cytoplasmic contents and recycles components to promote cellular remodeling and continue growth under nutrient-limiting conditions. Macroautophagy (here called autophagy) is the process by which bulk cytosolic contents and organelles are segregated into double-membrane autophagosomes (Robinson et al., 1998). Autophagosomes are transported to the vacuole, and the outer membrane fuses to the vacuolar membrane. The vacuolar-localized

structures surrounded by the single inner membrane, autophagic bodies, are then degraded by vacuolar enzymes.

Autophagy is not only important for recycling nutrients but also for degradation of damaged or superfluous proteins and organelles during normal growth conditions. Mitochondria, chloroplasts, and peroxisomes are major sources of reactive oxygen species (ROS) production, and ROS may contribute to organelle malfunction. Damaged mitochondria and excess peroxisomes can be selectively degraded by autophagy (Kim et al., 2007; Yu et al., 2008). Abnormal mitochondria accumulate in mice mutants defective in autophagy (Komatsu et al., 2006). In autophagy-defective plants, constitutive oxidative stress is apparent even under nonstarvation conditions (Xiong et al., 2007). In mice, lipid stores increase when autophagy is inhibited, as autophagy promotes lipid degradation for energy generation during nutrient deprivation (Singh et al., 2009).

1.4.2 Autophagy regulation

Autophagy progression includes induction, cargo selection, vesicle formation, fusion, and degradation (He and Klionsky, 2009). TOR (target of rapamycin) and Ras-cAMP-dependent protein kinase A (PKA) are the two well-characterized autophagy regulatory pathways in yeast and mammals (He and Klionsky, 2009; Schmelzle et al., 2004). TOR is a central repressor of autophagy. In response to amino acids, TOR is activated by the Ras-related small GTPase (Rag) protein and suppresses downstream autophagy (Kim et al., 2008; Sancak et al., 2008; Wullschleger et al., 2006). In response to the presence of glucose, Ras-cAMP-PKA can downregulate autophagy; this process is parallel to the TOR signal pathway (Schmelzle et al., 2004).

1.4.3 Autophagy in plants

In plants, autophagy can be induced by sucrose starvation, nitrogen depletion, senescence, and darkness (Bassham et al., 2006; Rose et al., 2006). Thus, autophagy induction appears to be related to carbon and nitrogen balance in Arabidopsis.

The Arabidopsis genome encodes one *AtTOR* gene with 49% amino acid sequence similarity to mammalian mTOR (Menand et al., 2002; Menand et al., 2004). Unlike mTOR, which is expressed in most mammalian cells, AtTOR is expressed only in undifferentiated plant cells (Menand et al., 2002) and is essential for embryonic development (Deprost et al., 2005).

1.4.4 The role of ATG4 and ATG8 in autophagy

Much of the autophagy machinery is conserved among yeast, animals and plants. ATG4 is a cysteine protease (Yoshimoto et al., 2004) that acts on ATG8 at two steps (Figure 1.5). In yeast, ATG4 first cleaves the ATG8 carboxyl-terminal arginine (R) exposing a glycine (G) residue (Figure 1.5). The ubiquitin E1-like enzyme, ATG7, activates the G residue of ATG8 and conjugates an E2-like protein, ATG3, to the ATG8 G residue. The G residue of ATG8 is then conjugated to the amino group of phosphatidylethanolamine (PE) which is thought to promote ATG8 association with and expansion of autophagosome membranes (Kirisako et al., 2000a). The second activity of ATG4 is to release ATG8 from PE, regenerating free ATG8 (Figure 1.5).

Plants also have ATG4, ATG8, ATG7 and ATG3, however, the regulation of ATG4 action on ATG8 is predicted to be more complicated. The Arabidopsis genome encodes 9 *ATG8* genes. Seven ATG8s (ATG8a-g) are predicted to require ATG4-

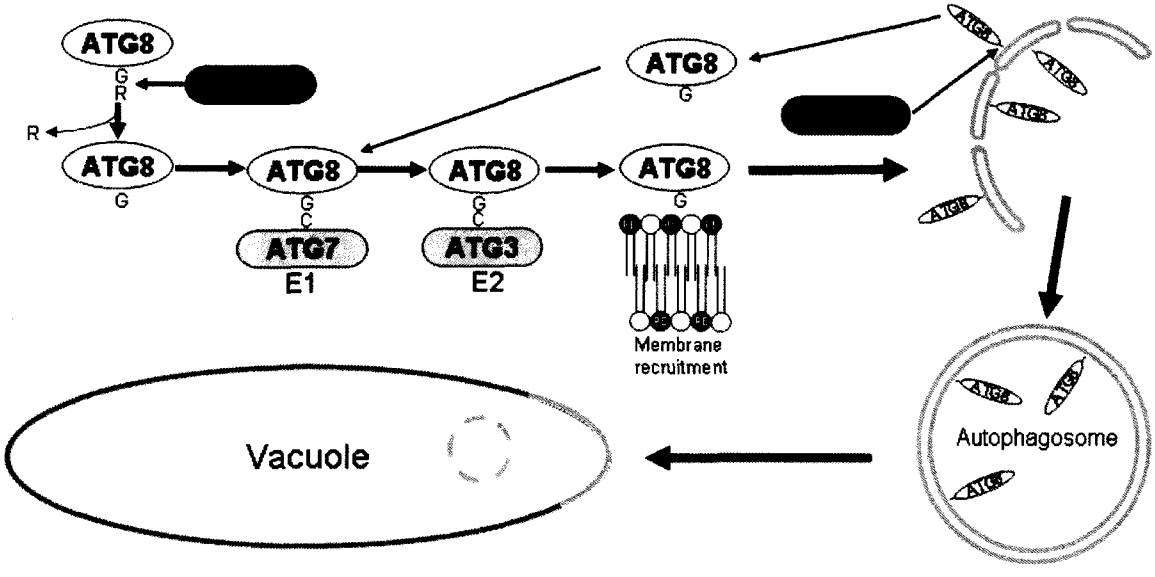

Fig 1.5 Schematic of yeast ATG4 and ATG8 roles in autophagy progression. Newly synthesized ATG8 carboxyl-terminal Arg (R) is removed by ATG4 protease, leaving a Gly (G) residue at the carboxyl terminus. The ATG8-G is activated by the E1 enzyme, ATG7, and then transferred to E2 enzyme, ATG3. Finally, ATG8 conjugates with PE and starts autophagosome membrane recruitment. ATG4 is required for ATG8-PE deconjugation. (Figure adapted from http://www.nibb.ac.jp/annual_report /2004/090.html)

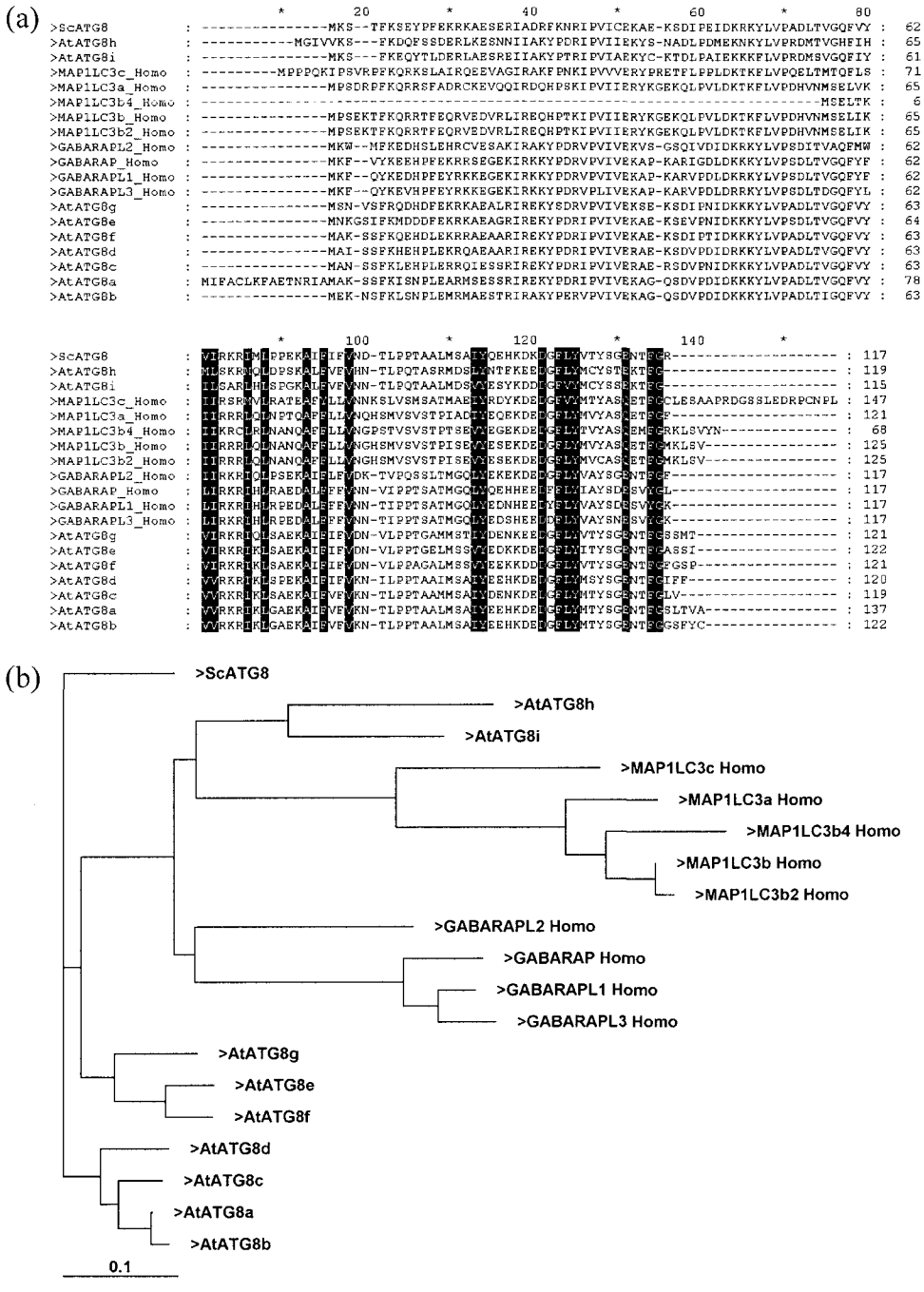

Fig 1.6 Amino acid sequence alignment and phylogenic tree of ATG8s. (a) The ATG8 amino acid sequence alignment was generated by ClustalX with output from GeneDoc. The black boxes indicate the identical amino acids. (b) The phylogenetic tree was generated by ClustalX using the Neighbor-Joining method with output from TreeView. At, Sc, and Homo represent Arabidopsis, yeast, and human, respectively. The distance indicated by "0.1" refers to the percent sequence divergence.

dependent maturation similarly to that described in yeast. However, ATG8h and ATG8i are synthesized with carboxyl-terminal G's and therefore are predicted to be independent of the ATG4-catalyzed maturation step (Fujioka et al., 2008; Tanida et al., 2004a). Phylogenetic comparative analysis of *ATG8* genes indicates that the Arabidopsis *ATG8h* and *ATG8i* are most closely related to human *ATG8* (Figure 1.6) (Slavikova et al., 2005). Further complexity in ATG8 function in Arabidopsis may derive from differential *ATG8* expression patterns in development and in response to diverse stimuli (Figure 1.7, Genevestigator).

The two distinct activities of ATG4 appear to be antagonistic with respect to the regulation of autophagy progression. Whereas the first action of ATG4 in ATG8 maturation may promote autophagy progression, the second action, removal of ATG8 from membranes, would likely prevent autophagy progression. Therefore, one might expect that ATG4 activity would require regulation. Consistent with this expectation, ATG4 activity in human cells has been found to be inhibited by oxidation (Scherz-Shouval et al., 2007). H_2O_2 production, stimulated by starvation, leads to superoxide generation; superoxide induces autophagy (Chen et al., 2009b). Cys78 of human ATG4 is oxidized in the presence of H_2O_2 and this oxidation inhibits ATG4 activity (◊, Figure 1.8) (Scherz-Shouval et al., 2007). ATG4 activity becomes constitutive if Ala or Ser are substituted for Cys78 and autophagy progression is defective (Scherz-Shouval et al. 2007). Thus, ATG4 activity inhibition by oxidation is likely to be required for mature autophagosome formation because excess ATG4b activity would theoretically prevent ATG8 accumulation on autophagosome membranes. Although plant ATG4s contain the homologous catalytic Cys residue (◊, Figure 1.8), plant ATG4s lack the analogous Cys78

required for redox regulation (◈, Figure 1.8). If plant ATG4s lack the ability to be regulated directly by oxidation, we predict that there exist alternative regulatory mechanisms in plants.

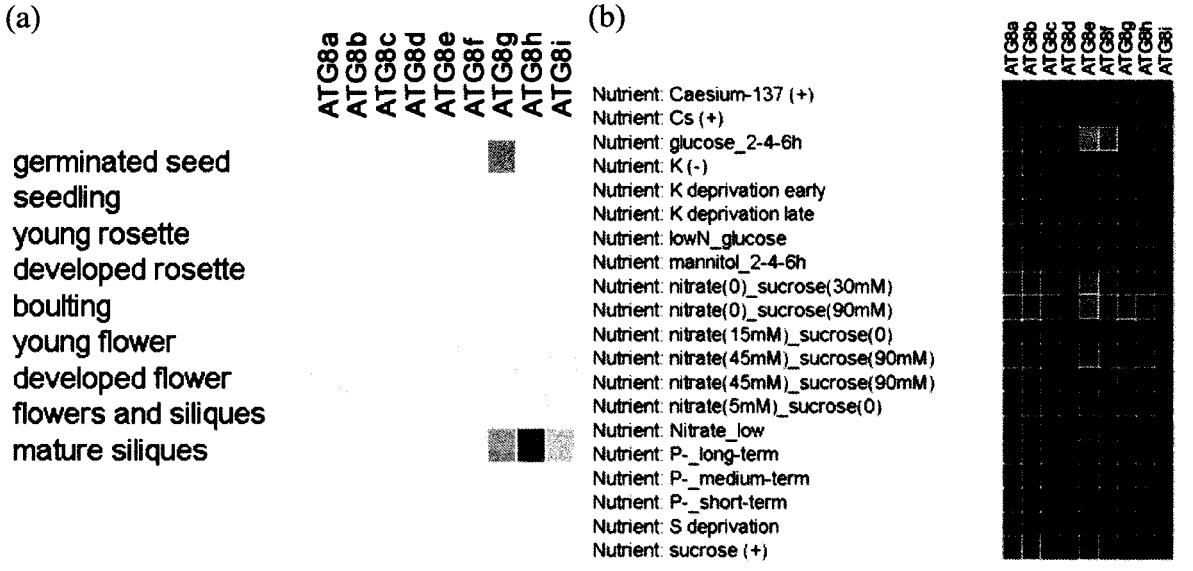

Fig 1.7 Genevestigator reported *ATG8* expression patterns obtained from Arabidopsis microarray experiments. (a) Differential expression of *ATG8s* in different developmental stages. Dark-blue coloring represents highest expression. (b) Differential expression of *ATG8s* in plants grown under different nutrient media. Red and green coloring represent elevated and decreased expression, respectively, of *ATG8s* after the treatments compared to non-treatments.

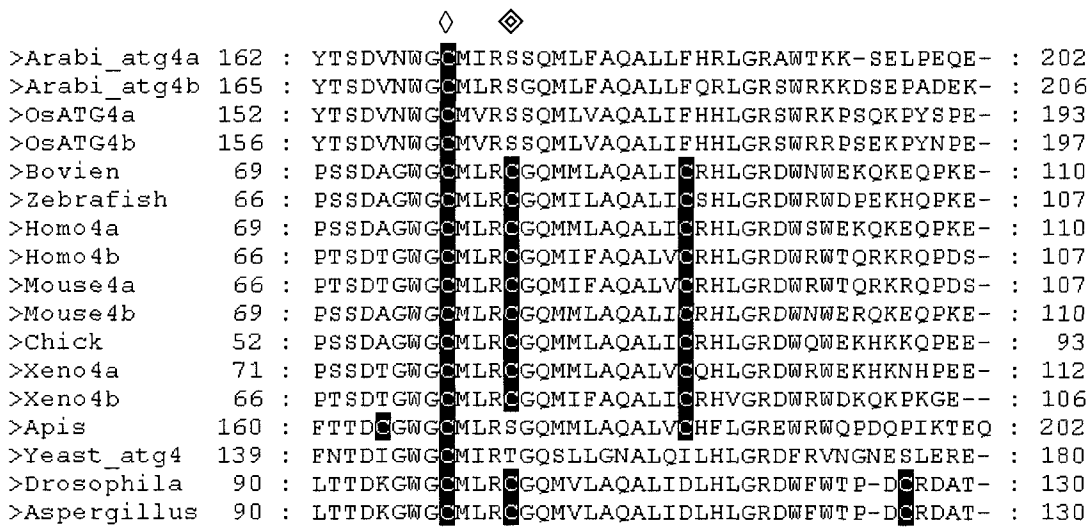

Fig 1.8 Plant ATG4 proteins lack the analogous oxidation-sensitive Cys78 of human ATG4. Amino-acid alignment of the region surrounding the active site Cys residue among members of the ATG4 family. The alignment was preformed using the ClustalX multiple alignment program. ◊ marks the catalytic Cys residue. ◈ marks Cys78 that is essential for redox regulation of human ATG4b but is missing in plant ATG4. Cys residues are highlight in black. Amino acid numbers are on the left and right of the sequences.

Chapter 2: Materials and Methods

2.1 Plant material and growth conditions

The *Arabidopsis thaliana* ecotype Col-0 was used in this study unless stated otherwise. Seeds were surface sterilized with 95% ethanol for 1 min and 6% sodium hypochlorite for 10 min followed by three washs with sterilized water. Sterilized seeds were stratified at 4°C for 48 to 72 hours and then sown in Metro-Mix 200 series soil (SunGro, Bellevue, WA, USA) or on agar plates (0.8% w/v) with media as described in 2.1.1 and were grown under 8, 16, or 24 hours photoperiods at approximately 60 μmol m^{-2} s^{-1} at 22°C. These growth conditions were used in this study unless stated otherwise.

2.1.1 Manipulation of nitrogen source in the culture media

Plants were grown on nitrogen-rich (PN or MS) or –free (PN-N or MS-N) media with or without 0.5% sucrose for specific periods as indicated. PN and half strength MS (1/2MS) media are commonly using for Arabidopsis growth media (Haughn and Somerville, 1986; Murashige and Skoog, 1962). The modified PN without nitrogen (PN-N) lacked KNO_3 and $Ca(NO_3)_2$ with substitution of KCl and $CaCl_2$ to maintain the same amount of potassium and calcium. MS-N media lacked KNO_3 and NH_4NO_3 from the MS formula (Table 2.1). MS media contain both NO_3^- and NH_4^+ and PN media contain only NO_3^- as nitrogen source.

2.2 Phenotype characterization

2.2.1 Analysis of transition to flowering

Plants were grown on soil under long- or short- photoperiods at 22°C. Flowering time was determined as the number of days from sowing the seeds to the appearance of a floral bud with inflorescence stems elongated over 2 mm. In addition, the number of rosette leaves present at the start of flowering was recorded.

2.2.2 Analysis of nitric oxide accumulation

To monitor nitric oxide levels *in vivo*, the first and second true leaves (around 5 mm in diameter) were detached from two-week-old soil-grown plants and submerged in MES buffer (10 mM MES (2-(*N*-morpholino) ethanesulphonic acid), 10 mM KCl, 0.1 mM $CaCl_2$, pH 5.8) for two hours. After addition of 10 mM 4-amino-5-methylamino-2',7'-difluorofluorescein diacetate (DAF-FM DA, Molecular Probes) for 45 min, fluorescence was analyzed with excitation at 490-495 nm and emission at 515 nm and visualized using a MZ FLIII (Leica, Switzerland) fluorescence stereomicroscope. For root nitric oxide levels measurement, 7-day-old seedlings were submerged in MES buffer with or without 200 μM L-NMMA (N^G-monomethyl-L-arginine monoacetate) for 30 min and then followed with DAF-FM DA staining for 15 min and imaging as described before. All the images had the same exposure time. To quantify the DAF-FM DA fluorescence, images were analyzed by Image J (Wayner Rasband, National Institute of Health, USA). The NO scavenger, 2-(4-carboxyphenyl)-4,4,5,5-tetramethylimidazoline-1-oxyl-3-oxide (cPTIO, Sigma-aldrich) 400 mM in 0.4% (v/v) DMSO and 0.1% (v/v) Tween20, was directly sprayed on leaves

of two-week-old plants; the control leaves were sprayed with solvent (0.4% DMSO, 0.1% Tween20). The first and second leaves were harvested after four hours.

2.2.3 Amino acid analysis sample preparation

100 mg of soil-grown leaf tissues were ground with liquid nitrogen and 200 µl of extraction buffer (0.1 N HCl, 0.4 mM amino acid standard) was added. The homogenized tissue extract was centrifuged for 15 min at 21,000g to remove tissue debris, and the supernatant was subjected to ultrafiltration (Ultrafree-MC PL-10, Millipore) to remove proteins. The filtered solution was frozen and dried in a lyophilizer. Amino acid contents were detected with HPLC in collaboration with Kendal Hirschi (BCM).

2.2.4 Analysis of Inductively Coupled Plasma-Mass Spectroscopy (ICP-MS)

ICP-MS was performed by Purdue Ionomics Information Management System (PiiMS) (Baxter et al., 2007). Plant tissues were prepared at Purdue. Plants were sown onto Sunshine Mix 19f (Sun Gro Horticulture) and stratified at 4°C for three days. Plants were grown under 10 h light/ 14 h dark (90 µmol m^{-2} s^{-1}), 18°C, 50% humidity, and fertilized twice per week with 0.25x Hoagland solution and 10 µM Fe-HBED (N,N'-di(2-hydroxybenzyl) ethylenediamine-N,N'-diacetic acid monohydro-chloride hydrate) was substituted for iron. The leaves were harvested from 5-week old plants and rinsed with deionized (18Ω) water. The samples were dried at 92°C for 20 h and weighed before acid digestion with concentrated nitric acid. The digested samples were processed with ICP-MS (Elan DRCe; Perkin-Elmer) for elemental analysis and the results were normalized to the dry weight.

Table 2.1 The formulas of different growth media.

	PN	PN-N			MS	MS-N	
KPO_4	2.5	2.5	mM	KPO_4	1.25	1.25	mM
KNO_3	**5**	**0**	**mM**	**KNO_3**	**18.8**	**0**	**mM**
$MgSO_4$	2	2	mM	$MgSO_4$	1.5	1.5	mM
H_3BO_3	70	70	μM	H_3BO_3	0.1	0.1	mM
$MnCl_2$	14	14	μM	$MnSO_4$	0.1	0.1	mM
$CuSO_4$	0.5	0.5	μM	$CuSO_4$	0.1	0.1	μM
$ZnSO_4$	1	1	μM	$ZnSO_4$	30	30	μM
Na_2MoO_4	0.2	0.2	μM	Na_2MoO_4	1	1	μM
$CoCl_2$	0.01	0.01	μM	$CoCl_2$	0.1	0.1	μM
NaCl	10	10	μM	$CaCl_2$	3	3	mM
$Ca(NO_3)_2$	**2**	**0**	**mM**	**NH_4NO_3**	**20.6**	**0**	**mM**
Fe-EDTA	49	49	μM	Na_2EDTA	0.1	0.1	mM
KCl	**0**	**5**	**mM**	$FeSO_4$	0.1	0.1	mM
$CaCl_2$	**0**	**2**	**mM**	KI	5	5	μM

The red indicates the components different in rich (PN or MS) to nitrogen-depleted (PN-N or MS-N) media.

2.2.5 Analysis of root length

Seeds were directly sown on agar plates with different media as described in each experiment. After stratifying the seeds at 4°C for 3 days, the plates were placed vertically (70°~80° angle) under constant light (~60 μmol m^{-1} s^{-2}) at 22°C. The seedlings were grown for different time periods and were photographed with a ruler. The images were processed with Image J to measure the root length.

2.3 Genetic analysis

2.3.1 Identification of T-DNA insertion plants

The *cml23-1* (SALK_003090), *cml23-2* (SALK_043636), *noa1* (SALK_047882), *nox* (SALK_116454), *nia1* (SALK_004164), *nia2* (SALK_075996), *atg4a-1* (CS858308), *atg4b-1* (SALK_026075), and *atg7-1* (SALK_057605) mutants were obtained from the Salk Institute sequenced-indexed insertion collection (Alonso et al., 2003). All these T-DNA mutants were generated in Arabidopsis (*Arabidopsis thaliana*) Columbia-0 (Col-0) ecotype. *nox*, *nia1*, *nia2*, *atg4a*, *atg4b*, and *atg7-1* were identified by PCR with T-DNA border primer and gene-specific primers. *cml23-1*, *cml23-2*, and *noa1* T-DNA insertion sites were verified by sequencing the PCR products using gene-specific primers and T-DNA border primers. Sequencing was done by Lone Star Sequencing (Houston, TX). The primers used to detect T-DNA insertion are listed in Table 2.2.

2.3.2 Identification of *cml24* point mutants

The *cml24* point mutants were isolated from an ethyl methanesulfonate (EMS) – induced mutant seed pool from ABRC by TILLING project (Till et al., 2003). To identify and confirm the homozygous plants, PCR and restriction enzyme digest-based

Table 2.2 SALK T-DNA insertion mutation and *cml24* point mutants identification

Genes	Primers	*R.E. digestion	Sequences
CML23	CML23L		GGACATGTCGAAGAACGTTTCGAGAAACTG
	CML23R		CTGGCGCGCCAGAGAGCCATTAAAGAAGCAAC
ATG4a	ATG4a_ex4L		TTGTCGAGCGTGGGAGTCATTAG
	ATG4a_3utrR		ACGTCGATGGGAAACTAACGATG
ATG4b	ATG4b_exon3F		AAAGGCTGGGAAGGTCTTGG
	ATG4b_exon5F		TCTCTGATAGCCACTTTCAC
ATG7	ATG7_R1		ACGCTTCCAAGTCTTTAAGATG
	ATG7_F1		GAAGACGCTACTTGCAATTC
NOA1	NOS1_R1		GTCACTTCCACAACCCAATC
	NOS1_F1		GAAACCCAGACGGAAGTATC
NOX	CUE1_R1		CATTGGAGCATGTAGAGCTTTC
	CUE1_F1		GCGTGGGTGGTATGGGACTATG
NIA2	NIR2_ex3R		CCTGCAGCTAGAATATCAAGAAATCCTCCTTGATG
	NIR2_ex1F		ATGGCGGCCTCTGTAGATAATCG
NIA1	NIR1_ex4R		CTAGAAGATTAAGAGATCCTCCTTCAC
	NIR1_ex1F		ATGGCGACCTCCGTCGATAAC
cml24-1 (G6E)	TCH2ASCIOE	*Xmn*I digestion	ATAAAGATGCCACCAGCTCACGCAATCTC
	TCH2EM1		TTGGCGCGCCTCAAGCACCACCACCATTACTCATCATCTTCTT
cml24-2 (G67E)	E124KL	*Bam*HI digestion	AACAGCATCACCAGAAGAAACACT
	G67EdCap		GAAAAGCGCGACGAATTCGTCCAGATCTATGgAT
cml24-3 (D72N)	D72NL	*Xmn*I digestion	AAACAATTCGATCTAGACGGTAACGGATTC
	D72NR		TTCTTTCAAATCGCTTACGTCGTTTCGATT
cml24-4 (E124K)	D72NL	*Hph*I digestion	AACAGCATCACCAGAAGAAACACT
	G160DR		TACGAATCATCACCGTCGACTAAT
cml24-7 (A98T)	D72NL	*Acl*I digestion	AACAGCATCACCAGAAGAAACACT
	G160DR		TACGAATCATCACCGTCGACTAAT
T-DNA	SALK_L1		ACTTGATTTGGGTGATGGTTCACGTAG
	SALK_R1		GCAATAATGGTTTCTGACGTATGTGCT

*R.E. restriction enzyme

analysis were applied. The primers used to identify the different *cml24* point mutants are listed in Table 2.2. DNA that was amplified with the specific primer set was purified and digested using the appropriate restriction enzyme (Table 2.2). *CML24* PCR products from segregating progeny of heterozygous *cml24-1* plants were digested with *Xmn*I; similarly, *cml24-2*, *cml24-3*, *cml24-4*, and *cml24-7* PCR products were digested with *Bam*HI, *Xmn*I, *Hph*I, and *Acl*I, respectively, to identify homozygous mutants (Table 2.2). The digested DNA fragments (usually <200bp) were separated by 4% agarose gel electrophoresis.

2.3.3 Selection of transgenics

The rapid identification of transgenics method is modified from a previously published method (Harrison et al., 2006). Transgenics were selected by growth on MS media with 0.8% agar with 50 μg mL^{-1} of kanamycin monosulphate, 50 μg mL^{-1} of DL-phosphinothricin (as known as BASTA, Finale®, AgrEvo, Montvale, NJ), or 15 μg mL^{-1} of hygromycin B. Seeds were stratified at 4°C for two days and transferred to continuously light growth chambers at 22°C. After 6 hours incubation to promote seed germination, plates were covered with aluminium foil and incubated for two days at 22°C and then transferred to continuously light and grown for 48 hours. Both kanamycin- and BASTA- resistant seedlings have long hypocotyls and green cotyledons relative to non-resistant seedlings which have long hypocotyls but pale cotyledons (Harrison et al., 2006). The hygromycin B-resistant seedlings have long hypocotyls and green cotyledons relative to non-resistant seedlings, which have short hypocotyls and green cotyledons (Harrison et al., 2006). The resistant seedlings were transferred and continuously grown on soil to collect seeds.

2.3.4 Double mutant generation and identification

cml23/cml24 double mutants were generated by crossing *cml23-2* T-DNA insertion mutants with *cml24-1* or *cml24-4* point mutants. Nikkí Delk identified homozygous mutants from the F_2 or later generations using the PCR- and restriction digest-based analyses described in Table 2.2.

The *cml24-4* point mutant was also crossed with *noa1* T-DNA insertion mutant to generate *cml24-4/noa1* double mutants. I verified the double homozygous plants from the F2 generation by PCR using the primers as described in Table 2.2.

atg4a4b double mutants were generated by crossing *atg4a-1* with *atg4b-1* T-DNA insertion mutants. The double homozygous mutants were identified by PCR from the F2 generation and the progeny of F2. *atg4a4b* double mutants did not have full length *ATG4a* and *ATG4b* coding sequences (CDS) amplified by RT-PCR.

2.3.5 Plant DNA isolation

For plant genotyping PCR, DNA was isolated from leaves using an alkali treatment modified from that previously reported (Klimyuk et al., 1993). 10 μL of 0.5 N NaOH was added to a 5 mm^2 leaf piece that had been ground on dry ice. Samples were boiled at 100°C for 30 seconds and neutralized with 100 μL of 0.2 M Tris pH 8, 1 mM EDTA on ice. DNA preps were stored at -20°C.

2.3.6 Plant RNA isolation

Total RNA was isolated using TRI Reagent® (Molecular Research Center, Inc., Cincinnati, OH). One mL of TRI Reagent® was added to 50-100 mg of homogenized plant tissue and incubated at room temperature for 5 min. The samples were vortexed for

15 seconds after adding 0.2 mL of chloroform to the homogenates and centrifuged at 12,000g for 15 min at 4°C. Following centrifugation, the upper aqueous phase was transferred to a new tube and mixed with 0.5 mL of 100% isopropanol to precipitate RNA. After removing the supernatants by centrifugation, RNA was washed with 75% (v/v) RNase free ethanol and resuspended in DEPC-treated water and stored at -20°C. RNA was quantitated using absorbance at 260 nm.

2.3.7 Reverse transcription (RT)

One μg of total RNA was DNase treated with 10 unit of DNase I (Roche Applied Science, Mannheim, Germany) at 37°C for one hour and heat inactivated at 75°C for 10 min. DNase-treated RNA was mixed with 250 ng of oligo$(dT)_{15}$ and 0.5 mM of dNTP and incubated at 65°C for 5 min. The DNase-treated RNA was placed on ice for one min then the reverse transcription mixture (4 μL of 5X First-strand buffer, 1 μL of 0.1M DTT, 50 units of SuperScript^{TM} III RT (Invitrogen, Carlsbad, CA)) was added to the sample and it was incubated at 50°C for one hour. Afterward, the sample was heat inactivated at 70°C for 15 min.

2.3.8 Quantitative RT-PCR (Q-PCR)

Approximately 80 to 100 ng of cDNA was used for each Q-PCR reaction, assuming 100% conversion from RNA to cDNA and 100% recovery from the reverse transcription reaction. Each 25 μL Q-PCR reaction contained 1X Thermocycler ABI SYBR Green PCR Master Mix (Applied Biosystems, Foster City, CA) and 500 nM of each forward and reverse gene specific primers. The primer sequences for Q-PCR are listed in Table 2.3. SYBR Green was detected by using an ABI PRISM 7000 (Applied

Table 2.3 Q-PCR primers list

Genes	Primers	Sequences
TUB4	qTUB4L	CTGTTTCCGTACCCTCAAGC
	qTUB4R	AGGGAAACGAAGACAGCAAG
CO	CO_qL	ATATGGCTCCTCAGGGACTC
	CO_qR	GGGTCAGGTTGTTGCTCTAC
FCA	FCA_qL	GAATGGCCGAGCTGGTAAAC
	FCA_qR	ATCCATCAGGCGAGGTATGC
FKF1	FKF1_qL	CGTTAGAGGTTGGGATGTTC
	FKF1_qR	CGAGGATCTCTGTACTGTAG
FLC	FLC_qL	AAGAAGAGAACCAGGTTTTG
	FLC_qR	GAAGATTGTCGGAGATTTGT
FRI	FRI_qL	GATGACTGAAGGAGGATTAG
	FRI_qR	CATTCCACGCTTGATACTTG
FT	FT_qL	TGATATCCCTGCTACAACTG
	FT_qR	TCGCGAGTGTTGAAGTTCTG
FVE	FVE_qL	TTCAGACCCTTGGACTATTG
	FVE_qR	AAGTCATAACGTGCGACTTG
FY	FY_qL	TATGCCATTGCACCCTCATC
	FY_qR	TTCATGCCACCTTGCATTCC
GI	GI_qL	GATTGCTGCTCCTGAAATCC
	GI_qR	GATGCACTTGCGAGAATCAC
LD	LD_qL	CCCACTCCATCAACTAATCC
	LD_qR	TGTACCCGATCTAGCAACTG
PIE1	PIE1_qL	GGAAGGCTCTCCTTAAAGTC
	PIE1_qR	TTCACGGAACCCATAAACTG
SOC1	SOC1_qL	CAAGCAGACAAGTGACTTTC
	SOC1_qR	GCCTCAGATAACGATCTATG
VIN3	VIN3_qL	GTGGTTTGAAGCAAGATAGG
	VIN3_qR	GTTCCAACAGATTCCGATAC
VRN1	VRN1_qL	GCGAGAAAGAGAACCGTGAC
	VRN1_qR	TTGATGAACCCGGAGATCCC
NIA1	NIA1_qL	TTCTGGTGCTGGTGTTTCTG
	NIA1_qR	TGCACACGTTGGTCCTAATC
NIA2	NIA2_qL	TTCTTTGGTAGACGCCGAAC
	NIA2_qR	TGACATGGCGTCGTAATCAC

Biosystems). The standard Q-PCR program conditions were: 50°C for 2 min, 95°C for 2 min to denature the cDNA, and 40 cycles of 95°C for 15 seconds and 60°C for 1 min. To determine the specificly of the amplified products, dissociation profiles were measured between 65°C to 95°C at the final step of Q-PCR program.

The difference in cycle number where product amplification resulted in a fixed threshold amount of fluorescence was determined by the following equation:

$\Delta CT_{sample} = \Delta CT_{TUB4} - \Delta CT_{gene\ of\ interest}$.

One sample was chosen as a calibrator and $\Delta\Delta CT$ was determined for each sample according to the equation:

$\Delta CT_{sample} = \Delta CT_{sample} - \Delta CT_{calibrator}$.

Relative RNA levels were calculated using inverse $\log_2$, $2^{\wedge (\Delta\Delta CT_{sample})}$.

2.4 Protein manipulations

2.4.1 Protein extraction and quantification

Total plant protein was isolated using LDS buffer (10% Glycerol, 1% LDS, 0.2 M Triethanolamine-Cl pH 7.6, 0.5 mM EDTA) unless stated otherwise. For ATG4 *in vitro* activity assay with tissue extracts, protein was extracted with KT buffer (25 mM Tris pH 7.5, 50 mM KCl) and 50 μg of total protein was assayed. For ATG8 western blots, the aqueous soluble protein was first extracted with KT buffer then the detergent soluble protein was extracted from the pellet of KT buffer with LDS buffer. Protein quantification was using the BCA™ Protein Assay Kit (Pierce, Rockford, IL) and the standard concentration curve was made with BSA.

2.4.2 CML24, cml24-2, and cml24-4 protein generation and purification

To construct an *E. coli* expression plasmid encoding CML24, the full-length CDS of *CML24* was amplified by PCR from Col-0 wild-type cDNA using the following primers: 5'-catatgATGTCATCGAAGAACGGAG TTG-3' and 5'-CggatccTCAAGCACCACCACCATTAC-3'. The lowercase letters indicate added restriction enzyme sites. CML24 PCR products were inserted into the cloning sites (*Nde*I/*Bam*HI) of pET21b. *cml24-2* and *cml24-4* CDS were amplified from *cml24-2* and *cml24-4* cDNA, respectively, with the same *CML24* primers. *cml24-2*, and *cml24-4* PCR products were inserted into the cloning site (*Nde*I/*Bam*HI) of pET24a. pET24a-cml24-2 and pET24a-cml24-4 were engineered by Dr. Jiabing Ji of the Braam lab. All of the constructs were sequenced and transformed into *E. coli* BL21 (DE3).

Recombinant protein synthesis was induced by adding IPTG (isopropyl 1-thio-β-D-galactopyanoside) at 37°C to cells at OD_{600}= 0.6 ~1.0. After induction, *E. coli* was lysed with a homogenizer (EmulsiFlex-C5, AVESTIN) in 20 mM Tris, pH 7.5, 200 mM NaCl, 1mM DTT and 1 mM EDTA buffer. After centrifugation at 30,000g, the supernatant was incubated with $CaCl_2$ at a final concentration of 3 mM before being applied to a Phenyl Sepharose CL-4B column equilibrated with 25 mM Tris, pH 8.0, 150 mM NaCl, 1 mM DTT, 1 mM $CaCl_2$. CML24, cml24-2, and cml24-4 were eluted with 25 mM Tris pH8.0, 150 mM NaCl, 1 mM DTT, 1 mM EDTA and precipitated with 70% saturated ammonium sulphate. The pellets were solubilized and dialyzed with 25 mM Tris pH 8.0, 150 mM NaCl, 1 mM DTT, 10% glycerol.

2.4.3 GST-ATG4b protein generation and purification

ATG4b (At3g59950) was amplified by PCR using wild type Col-0 cDNA as template. The oligo primers added *Bam*HI (ATG4b-BamHIF: GggatccATG AAGGCTATATGTGATAGATTTG) and *Eco*RI (ATG4b-EcoRIR: CCgaattcTCAA AGTAATTGCCAGTCATC) restriction enzyme sites flanking *ATG4b*. The recombinant *ATG4b* PCR product was cloned into the TA cloning vector pCR2.1-TOPO (Invitrogen, Carlsbad, CA) and the insertion fragment was sequenced and confirmed with T7 primer. pCR2.1-ATG4b and pGEX2T (a gift from Dr. McNew) were digested with *Bam*HI and *Eco*RI and separated by electrophoresis, then the *ATG4b* fragment and linearized pGEX2T vectors were eluted from the TAE-gel using QuickClean DNA Gel Extraction Kit (GenScript Co.). *ATG4b* was cloned into pGEX2T vector downstream of the *glutathione S-transferase* (*GST*) coding sequences using T4 DNA ligase (NEB, Beverly, MA). pGEX2T-ATG4b was chemically transferred into competent *E. coli* BL21 (DE).

E. coli BL21 (DE3) with pGEX2T-ATG4b was inoculated in 25 mL LB/ampicillin and cultured overnight with shaking at 37°C. The cells were transferred from 25 mL overnight culture to 500 mL 2xYT/ampicillin and continuously grown with shaking at 37°C to OD_{600}= 0.6 to 1.0. One mM final concentration of IPTG was added to the media and continued culture 2 hours at 37°C. Cells were centrifuged at 5,000 g for 10 min at 4°C, and the pellet was kept at -70°C.

The cell pellet was resuspended in GST binding buffer (25 mM Tris pH 7.5, 150 mM NaCl, 1 mM EDTA, 1x protease inhibitor (P-9599, Sigma)) and then lysed by passing through a homogenizer (EmulsiFlex-C5, AVESTIN) three times. Cell lysate was centrifuged at 30,000g for 10 min at 4°C. The supernatant was transferred to a new 50

mL tube and added 500 μL of washed glutathione (GSH)-Sepharose 4B beads (prewashed with GST binding buffer and resuspended to 50% slurry). The supernatant and GSH-beads were rocked at 4°C for two hours. GSH-beads were spun down at 500 g for one min and washed with GST binding buffer twice. GST-ATG4b protein was eluted from GSH-beads twice with 500 μL elution buffer (10 mM reduced GSH, 50 mM Tris pH 8.0, 5% glycerol). The eluted proteins were analyzed by SDS-PAGE. The eluted GST-ATG4b protein was dialyzed in buffer (20 mM Tris pH 8.0, 200 mM NaCl, 10% glycerol) at 4°C overnight.

2.4.4 His-ATG8e-HA protein generation and purification

The HA tag was first introduced to the carboxyl-terminus of AtATG8e (At2g45170) by PCR using wild type Col-0 cDNA as template. The oligo primers were engineered *Nde*I (ATG8e-F3: GCCcatatgAATAAAGGAACATCTTTAAGATGGACGACG) and *Bam*HI (ATG8e-R3HA: TGCggatccCTAAGCGTAATCTGGAACATCGTATGGGTAGATTGAAGAAGCACCGA) restriction enzyme sites flanking *ATG8e*. The reverse primer ATG8e-R3HA added hemagluttinin (HA) sequences (underlined sequences) downstream of the ATG8e carboxyl-terminus before the stop codon. The engineered ATG8e-HA fragment was cloned into pCR2.1-TOPO vector and the sequence was confirmed by T7 primer sequencing. The protein expression binary vector pET15b and pCR2.1-ATG8eHA were digested with *Nde*I and *Bam*HI. The digested products were separated by electrophoresis and the engineered ATG8e-HA fragment and linearized pET15b vector were eluted from TAE-gel using Gel Clean Kit (GeneScript, Co.). Engineered ATG8e-HA was cloned into the pET15b vector downstream of the His tag using T4 DNA ligase (NEB, Beverly, MA).

pET15b-ATG8e plasmid was chemically transferred into competent *E. coli* BL21 (DE3) for protein expression. The transformed *E. coli* cells were inoculated in 25 mL LB/ampicillin and cultured overnight with shaking at 37°C. The overnight culture was transferred to 500 mL 2xYT/ampicillin and grew with shaking at 37°C until the OD_{600} reached 0.6 to 1.0. 1 mM final concentration of IPTG was added to the media and growth continued for 2 hours at 37°C. Cells were centrifuged at 5,000 g for 10 min at 4°C, and the pellet was kept at -70°C.

His-tag protein purification procedure was modified from a previously published method (Petty, 1996). The cell pellet was resuspended in MCAC-0 buffer (20 mM Tris-Cl pH 7.9, 0.5 M NaCl, 10% glycerol, 1 mM PMSF) and then lysed by passing through a homogenizer (EmulsiFlex-C5, AVESTIN) three times. The cell lysate was mixed with 0.1% Triton X-100, 10 mM $MgCl_2$, and 10 μg/mL DNaseI at the final concentration and centrifuged at 15,000 rpm (SS-34 rotor) for 10 min at 4°C. The supernatant was loaded onto Ni^{2+}-NTA column which had been equilibrated with MCAC-0 buffer. The column was washed with MCAC buffer containing 20 mM imidazole and His-ATG8e-HA protein was eluted and collected with MCAC buffer containing 40 to 200 mM imidazole. The eluted protein was analyzed by SDS-PAGE (Figure 6.1). To prevent His-AtATG8e-HA recombinant protein aggregation, the eluted proteins were ultrafiltrated with 20mM Tris pH 7.0, 1% glycerol, 0.5 M urea, and 300 mM NaCl (Chae et al., 2004).

2.4.5 Ca^{2+}-induced mobility shift

To test whether CML24 and the cml24 mutants isoforms (cml24-1, cml24-2, cml24-4) were able to undergo Ca^{2+}-dependent conformation changes, the recombinant CML24 protein and total plant proteins from wild type and *cml24* mutants were

incubated with 5 mM $CaCl_2$ or 5 mM EGTA for 15 min at room temperature and separated on 13% SDS-PAGE with constant voltage at 60 V. CML24 proteins were detected by western blot with anti-CML24 antibody (section 2.4.11) or coomassie blue staining.

2.4.6 GST pull-down analysis

The purified GST-fused ATG4b was incubated with GSH-Sepharose 4B beads for 30 min at 4°C and washed with TBS buffer (50 mM Tris, pH 7.5, 150 mM NaCl). CML24, cml24 protein, or CaM (P1431 Sigma) were added to the beads with 1mM $CaCl_2$ or 1mM EGTA and incubated at 4°C for 1hour. After washing the beads three times with TBS containing 0.05% Triton X-100, 1 mM $CaCl_2$ or EGTA, proteins bound to the beads were directly subjected to SDS-PAGE and immunoblotting (section 2.4.11).

2.4.7 ATG8a antibody purification

The antisera against ATG8a were provided by Dr. Yoshinori Ohsumi (National Institute of Basic Biology, Okazaki, Japan). The antiserum was affinity purified by passing the serum through a His-ATG8e-HA coupled Ni-NTA column. The column was washed with equilibration buffer (150 mM NaCl, 50 mM Tris pH 7.4). The serum was loaded onto the column and washed with equilibration buffer and 2 M NaCl, 50 mM Tris pH 7.5. The polyclonal anti-ATG8a antibody was eluted with 4 M $MgCl_2$ and dialyzed in PBS buffer overnight. The washed and eluted fractions were analyzed on SDS-PAGE (Figure 2.1). An intensive band appeared in the first elution around 50 kDa relative the the molecular weight marker, which likely is IgG heavy chains. The final concentration of anti-ATG8a antibody is 2 mg/mL and is stored in PBS with 0.02% NaN_3.

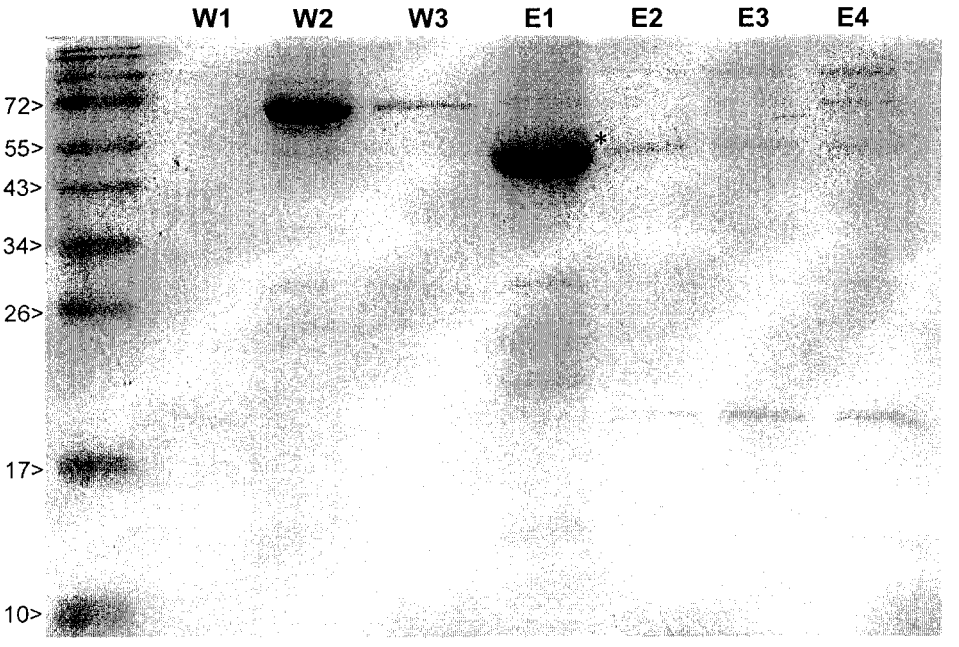

Figure 2.1 ATG8a antibody purification. ATG8a polyclonal antibody was purified with His-ATG8e-HA coupled Ni-NTA column. W1, W2, and W3, washed fractions with 2 M NaCl, 50 mM Tris, pH 7.5. E1, E2, E3, and E4, eluates with 4 M $MgCl_2$ from Ni-NTA column. Molecular mass markers are indicated at left. Asterisk indicates potential IgG heavy chains. Proteins were detected on a Coomassie Blue-stained SDS-PAGE.

2.4.8 ATG8e antibody generation and purification

Recombinant His-ATG8e-HA protein was generated and purified. I was able to store the protein for only short periods in buffer (20 mM Tris pH 7.0, 1% glycerol, 0.5 M urea, and 300 mM NaCl) because of its tendency to precipitate. To isolate enough protein for antigen production, I purified 8 mg of recombinant His-ATG8e-HA protein and separated if on several protein gels and cut out the His-ATG8e-HA as gel slices. The immunization of rabbits was performed by GenScript Co. I analyzed the specificity of four antisera after the second immunization from the rabbits (Figure 2.2). 80 μg of aqueous (Figure 2.2, lanes 1, 3, 5, 7, and 9)- and detergent (Figure 2.2, lanes 2, 4, 6, 8, and 10)-soluble protein samples were extracted from Col-0/*GFP-ATG8e* transgenics and immunoblotted with the antisera. The fold dilution of the antisera were based on ELISA test; anti-ATG8a (1:2500), anti-ATG8e#6999 (1:640), anti-ATG8e#7000 (1:160), anti-ATG8e#7001 (1:320), and anti-ATG8e#7002 (1:1280). Anti-ATG8a antibody appeared to recognize two molecular weight proteins in the aqueous soluble fraction (Figure 2.2, lane 1); the high molecular (~41 kDa) and low molecular (~16 kDa) bands are consistent with full length GFP-ATG8e (41 kDa) and endogenous ATG8 (17 kDa). Only the high molecular band was recognized by anti-ATG8a in the detergent soluble fraction (Figure 2.2, lane 2). The antiserum ATG8e#6999 has two bands around 23 and 17 kDa in the aqueous soluble fraction (Figure 2.2, lanes 3). The band around 17 kDa could be ATG8. One band is detected around 26 kDa by #6999 in the detergent soluble fraction (Figure 2.2, lane 4). Antiserum ATG8e#7000 has lowest titer and high background in the western blot. An approximate 18 kDa band from the aqueous soluble fraction and no clear band in detergent soluble fraction was detected by antiserum ATG8e#70002 (Figure 2.2, lanes 5

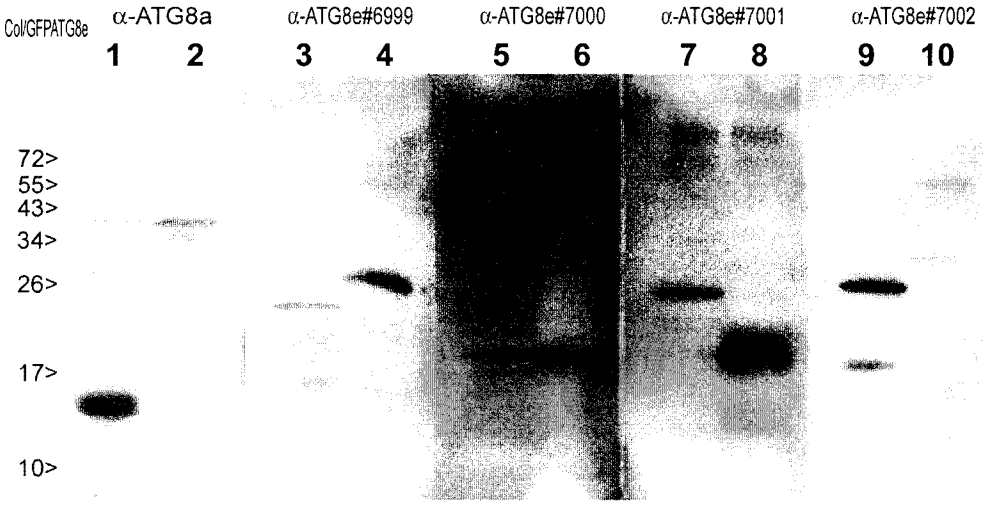

Figure 2.2 Anti-ATG8e sera reaction with plant extract proteins. Total protein was extracted with KT (odd-numbered lanes) and LDS buffer (even-numbered lanes) from Col-0/GFP-ATG8e transgenic plants and separated on 15% SDS-PAGE and followed by western blot with anti-ATG8a and four anti-ATG8e sera. Endogenous ATG8s and GFP-ATG8e are around 16 -17 and 43 kDa, respectively.

and 6). Antiserum ATG8e#7001 detected an 26 kDa and 18 kDa bands in aqueous- and detergent-soluble fractions, respectively (Figure 2.2, lanes 7 and 8). Antiserum ATG8e#7002 detected similar two bands in aqueous-soluble fraction as #6999 and the lower molecular mass protein could be ATG8 (Figure 2.1, lane 9). There are also two light bands detected by antiserum ATG8e#7002 from the detergent soluble fraction and the molecular mass is around 55 and 28 kDa (Figure 2.1, lane 10). The antiserum ATG8e#7002 had highest titer, lowest background, and detected a potential ATG8 protein relative to other antisera. However, the ELISA titer decreased in the final serum and the final antibody after IgG purification cross-reacts with other proteins (data not shown). This antibody should be affinity purified and re-tested to determine whether it will be useful.

2.4.9 *In vitro* ATG4 activity analysis

Approximately equal moles (60 pmole) of recombinant GST-ATG4b (~78 kDa), His-ATG8e-HA (~17 kDa), and CML24 (~17 kDa) were used *in vitro* activity analysis. GST-ATG4b was mixed with or without CML24 in presence of 5 mM Ca^{2+} or 5 mM EDTA at room temperature for 10 min and then His-ATG8e-HA was added to the reactions. Thereafter, the reactions were incubated at the conditions: 20°C for two hours, 10, 20, 30, 40, and 50°C for three hours, 30°C for two and six hours. The samples were subjected to 15% SDS-PAGE and proteins were detected by western blot with anti-His or anti-HA antibody or coomassie blue staining.

For tissue extract ATG4 activity analysis, two-week-old long-photoperiod soil-grown plants (Col-0, *cml24-2*, *cml24-4*, *atg4a*, *atg4b* and *atg4a4b*) were collected during the light period or one hour after the shift to darkness and extracted with KT buffer (25

mM Tris pH 7.5, 50 mM KCl, 1 mM PMSF, 1 mM EDTA). 50 μg total protein was mixed with 0.2 μg of His-ATG8e-HA as substrate and incubated at 30°C for two hours. Samples were subjected to 15% SDS-PAGE and ATG8 proteins were detected by immunoblotting with anti-ATG8a antibody.

2.4.10 Nitrate reductase activity analysis

Soil-grown two-week-old seedling leaves were harvested and ground on dry ice. Extraction buffer (50 mM Hepes-KOH (pH 7.6), 1 mM DTT, 10 μM FAD, 10 mM $MgCl_2$ and 50 μM cantharidine) was added to the frozen powder (two mL/g FW) (Kaiser et al., 2000). After centrifugation at 16,000g for 10 min at 4°C, to determine activated NR activity (NR_{act}), 100 μL of the supernatants were mixed with 900 μL reaction buffer (50 mM Hepes-KOH (pH 7.6), 10 μM FAD, 1 mM DTT, 10 mM $MgCl_2$, 5 mM KNO_3, 0.2 mM NADH) and incubated at room temperature for 3 min. To determine total NR (NR_{max}), another 100 uL aliquots were incubated at room temperature for 12 min with 5 mM 5'-AMP and 15 mM EDTA at final concentration before adding 895 μL reaction buffer ($MgCl_2$ was substitute with 15 mM EDTA). To each sample, 125 μL of 0.5 M zinc acetate was added to stop the reaction and samples were centrifuged at 16,000g for 10 min. To oxidize the NADH left in the reactions, 10 μM (final concentration) phenazine methosulfate was added, and the samples were further incubated at room temperature for 15 min in the dark. For colorimetric determination of nitrite formation, 500 μL of each sample was reacted with 250 μL of 1% (w/v) sulfanilamide (in 3 N HCl) and 250 μL of 0.02% (w/v) N-(1-naphthyl) ethylenediamine for 20 min at room temperature. Samples were briefly spun to remove any precipitate and supernatant absorbances at 546 nm

wavelength were determined with a spectrophotometer (DU640, Beckman). Absorbances were normalized to the protein concentration of the samples.

2.4.11 Western blot analysis

50~80 μg of total tissue protein was loaded onto 13% SDS-PAGE and separated by electrophoresis. After electrophoresis, proteins were blotted to 0.2 μm nitrocellulose membranes (Whatman, GE) in transfer buffer (25 mM Tris, 1.44% glycine, 20% methanol, 2 mM $CaCl_2$) using semi-dry transfer system Owl blotter (OWL separation Systems, Portsmouth, NH) with 100 mAmp constant current for 45 mins for each gel. Membranes were baked at 60°C overnight. Baked membranes were blocked in 1X TBST (TBS buffer, 0.1%(v/v) Tween-20) with 1% skim milk (Carnation) for one hour before adding the first antibody and then incubated at room temperature for one hour. All incubations were with gentle rocking. The final concentration or the fold dilution of first antibodies were as follows: 2.4 μg/mL CML24 (Delk, 2006), 1:1000 HSC70 (SPA-818, Assay designs, Ann Arbor, MI), 1:1000 β-ATPase (a gift from Dr. Bartel), 1:500 GFP (SC-9996, Santa Cruz Biotechnology, Santa Cruz, CA), 1:1000 GST (a gift from Dr. McNew), 1:1000 HA (05-904, Millipore, Billerica, MA) and 1:1000 His (MMS-156R, Covance, Princeton, NJ). For anti-ATG8a western blots, the blots were incubated with the first antibody (1:5000) at 4°C overnight to minimize non-specific interaction. The membranes were washed with 1X TBST 10 min three times. The secondary antibodies were diluted in 1X TBST with 1% skim milk and the membranes were incubated at room temperature for one hour. Goat-anti-mouse antibody conjugated with horseradish peroxidase (SC-2005, Santa Cruz Biotechnology, Santa Cruz, CA) for anti-β-ATPase, GFP, GST, HA and His antibodies was diluted 1: 5,000 and goat-anti-rabbit antibody

conjugated with horseradish peroxidase (Pierce, Cat.31460, Rockford, IL) was diluted 1: 10,000 for CML24 and ATG8a antibodies. Nonspecific secondary antibody binding was reduced by washing with 1X TBST 10 min four times. Pierce Super Signal West Pico chemluminescent kit was used for detecting the specific interacting secondary antibody.

2.4.12 MALDI-TOF mass spectroscopy

To determine whole protein mass, one μg of recombinant CML24 protein was directly incubated at 99°C for 5 min, with 25 mM iodoacetamide (IAM) for one hour, or 5 mM DTT at 37°C for 10 min prior to 25 mM IAM for one hour. C_{18} Zip-tip-purified recombinant CML24 proteins were directly mixed with matrix (20 mg/mL sinapinic acid (SA) in 50% acetonitrile (ACN)/0.1% Trifluoro acetic acid (TFA)) and spotted on a SCOUT-MTP targets. Mass spectra were collected with a Bruker Autoflex™ II MALDI-TOF operated in linear mode and calibrated with Protein Calibration Standard I (Part No. 206355, Burker). I analyzed positively charged ions in the *m/z* range 10,000-25,000. The spectra were summed for 1000 laser pulses.

To identify the peptides of CML24, 10 μg of recombinant CML24 protein was treated as follows: (1) CML24 was denatured with 4 M guanidine thiocyanate (GdmCN) at 95°C for 10 min and incubated with 100 mM IAM for 30 min at 37°C. (2) CML24 denatured with 4 M GdmCN at 95°C for 10 min and incubated with 5 mM EDTA, 100 mM IAM for 30 min at 37°C. (3) CML24 was denatured with 4 M GdmCN at 95°C with 10 mM DTT and incubated with 100 mM IAM for 30 min at 37°C (4) CML24 was denatured with 4 M GdmCN at 95°C with 10 mM DTT and incubated with 5 mM EDTA, 100 mM IAM for 30 min at 37°C. Samples were digested with 0.1 μg/μl Trypsin

overnight at 37°C and purified with C_{18} Zip-tip. Purified peptides were mixed with α-cyano-4-hydroxycinnamic acid matrix (10 mg/mL in 50% ACN/0.1% TFA) and spotted on an AnchorChip Target™. Mass spectra were collected with a Bruker Autoflex™ II MALDI-TOF operated in reflected mode and calibrated with Peptide Calibration Standard II (Part No. 222570, Burker). I analyzed positively charged ions in *m/z* range 700-3500. The spectra were analyzed with MASCOT database (Perkins et al., 1999) and tolerated 50 parts per million mass error and one permitted missed cleavage site.

2.5 Fluorescence microscopy

2.5.1 GFP-ATG8e green fluorescent protein visualization

To visualize GFP fluorescence, GFP-ATG8e transgenic roots were imaged *in vivo* using Axioplan II (Zeiss) with narrow-band GFP filter (Chroma 41020). The Z-stack images were taken and processed with deconvolution and 3D reconstruction with MetaMorph software. To prevent non-specific epi-fluorescence signal, non-GFP or GFP vector transgenic plants were also imaged and confirmed with DAPI/ Texas Red filters.

2.5.2 Monodansylcadaverine staining and visualization

Arabidopsis whole seedlings were incubated with 0.05 mM monodansyl-cadaverine (MDC) in PBS buffer for 10 min at room temperature (Contento et al., 2005). After staining, seedlings were washed with PBS twice to remove excess dye and mounted on slides. *In vivo* MDC fluorescence was observed at 335 nm wavelength using a DAPI filter on Axioplan II (Zeiss) or two photon laser on LSM510 confocal microscopy (Zeiss). To prevent non-specific epi-fluorescence signal, non-MDC staining plants were

also imaged and confirmed with Texas Red filters. The images were processed and quantified with MetaMorph or Image J software.

Chapter 3: Arabidopsis Potential Calcium Sensors Regulate Nitric Oxide Levels and Transition to Flowering

To begin to identify the physiological functions of *CML24*, we initiated reverse genetic approaches. CML24 protein has 4 EF hands and shares 44% amino acid identity with CaM (Braam and Davis, 1990; Khan et al., 1997). *CML24* mRNA accumulates in response to heat shock, touch, wounding, dark, cold, H_2O_2, ABA, and auxin (Braam, 1992; Braam and Davis, 1990; Delk et al., 2005; Polisensky and Braam, 1996). Nikkí Delk, a previous graduate student in the Braam lab, identified *CML24* underexpressing transgenics, *U1* and *U2*, which have an epigenetically silenced *CML24* gene and strong reduction of *CML24* transcript and protein levels (Delk et al., 2005). *U1* and *U2* have reduced $MgCl_2$, $CoCl_2$, Na_2MoO_4, $ZnSO_4$, and ABA sensitivity compared to wild type (Delk et al., 2005). In addition, both *U1* and *U2* transition to flowering later than wild type (Delk et al., 2005).

To further characterize CML24 functions, we aimed to identify true genetic lesions in *CML24* because of potential complications, such as instability, using epigenetically silenced lines. No T-DNA insertions have been identified in *CML24*, therefore we sought TILLING mutants (Till et al., 2003). Nikkí Delk identified ten TILLING-generated *CML24* mutants, which have single amino acid substitutions (Table 3.1).

CML23 shares close sequence similarity with CML24 (78% amino acid sequence identity), and *CML23* and *CML24* share overlapping expression behavior (Tsai et al., 2007). Because of the potential for at least partial functional redundancy between *CML23*

Portions of this chapter have been published (Tsai et al., 2007).

Table 3.1 *cml24* point mutations and mutant flowering phenotype

Allele name	Mutation	Flowering phenotype
cml24-1	6^{th} Gly → Glu	Same as wild type
cml24-2	67^{th} Gly → Glu	Early flowering
cml24-3	72^{th} Asp → Asn	Late flowering
cml24-4	124^{th} Glu → Lys	Late flowering
cml24-5	36^{th} Asp → His	*Early flowering
cml24-6	36^{th} Asp → Asn	
cml24-7	98^{th} Ala → Thr	Late flowering
cml24-8	105^{th} Asp → Asn	
cml24-9	130^{th} Asp → Asn	
cml24-10	160^{th} Gly → Asp	

* *cml24-5* early flowers only under high intensity light (Delk, 2006).

and *CML24*, we sought to identify and characterize *CML23* mutants also. Nikkí Delk identified two *cml23* T-DNA knock out insertion mutants, *cml23-1* and *cml23-2*. The *cml23* single mutants have no detectable differences in phenotype relative to wild type (Delk, 2006). However, combining *cml23-2* with the point mutation, *cml24-1*, results in decreased Mg^{2+} sensitivity relative to wild type (Delk, 2006). Because this phenotype is not detected in either *cml23-2* nor *cml24-1*, we conclude that *CML23* and *CML24* have at least partially overlapping function and the effect of the *cml24-1* mutation on CML24 function may be less severe than the apparent loss of *CML24* expression in the underexpressing *CML24 U1* and *U2* transgenics.

3.1 *CML24* regulates the transition to flowering

3.1.1 *CML24* is required for photoperiod regulation of the transition to flowering

The transition to flowering in Arabidopsis is promoted by long photoperiods (≥ 14 hr light), and mutants defective in this photoperiod-regulated transition fail to respond to the lengthened light period. *cml24-4* flowers later than wild type in long-day photoperiods (Figure 3.1a) consistent with a defect in the photoperiod pathway of flowering regulation. In addition, *cml24-4* generates a greater number of rosette leaves than wild type prior to flowering (Figure 3.1d). Altered rosette leaf number at flowering is an indicator that flowering time differences are the consequence of defective regulation of floral induction and not simply slowed growth rate. *cml24-4* flowering time is comparable to wild type when grown in short-day photoperiods (Figure 3.1c and 3.1e), subjected to an extended cold period (data not shown), or treated with gibberellin (GA)

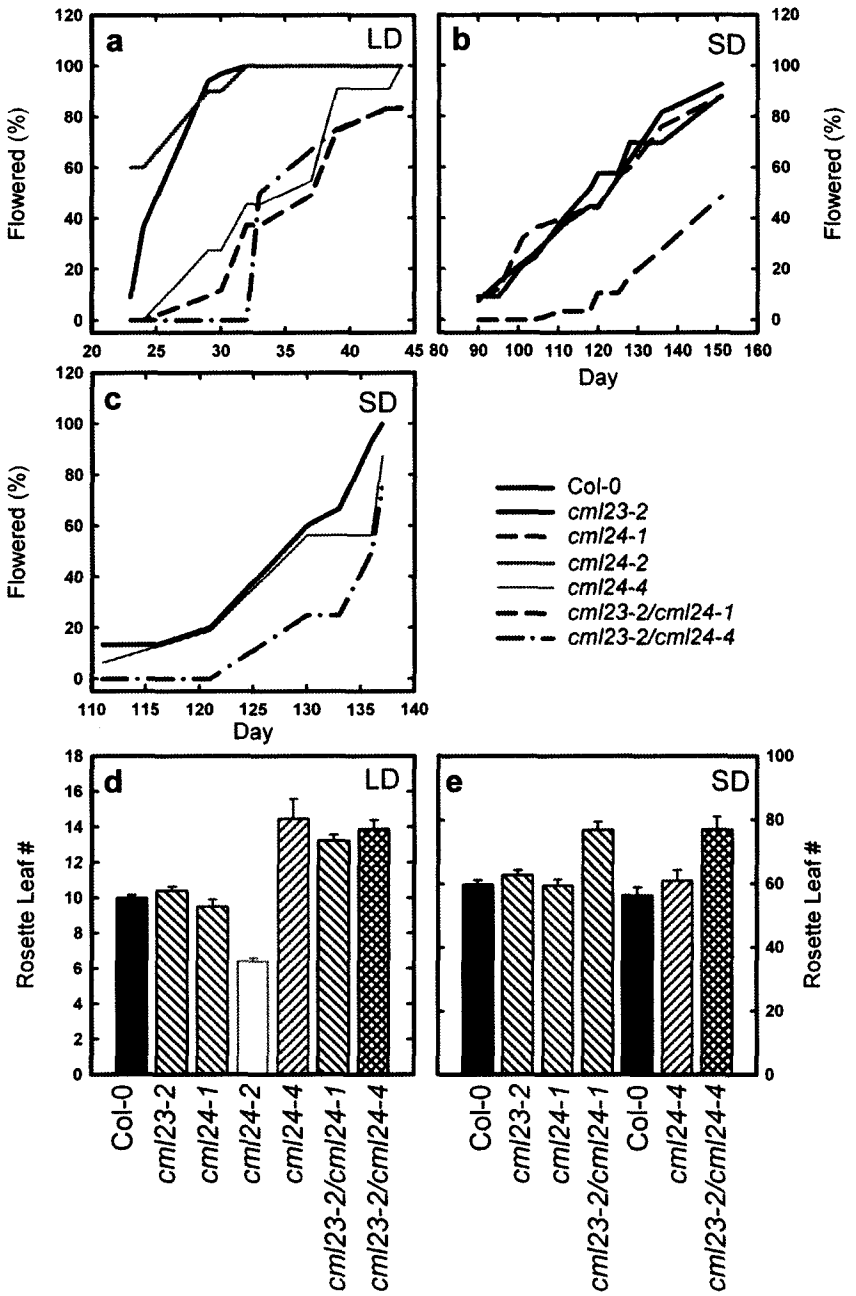

Fig 3.1 *CML23* and *CML24* are required for appropriate timing of the transition to flowering. Wild type (Col-0) and mutants were grown in LD 16-hour (a) or SD 8-hour (b) and 7-hour (c) photoperiods and the percentages of plants flowering over time were recorded. Rosette leaf numbers at flowering onset were recorded for Col-0 and mutants grown under (d) LD and (e) SD photoperiods. LD: long-day, SD: short-day. Values are means ± SE (n = 6 to 33). (Tsai et al., 2007).

(data not shown). These three results indicate, respectively, that the autonomous, vernalization and GA flowering regulatory pathways are intact. *cml24-4* is thus specifically defective in the photoperiod pathway. The coincidence of a photoperiod-specific defect in both *cml24-4* and *CML24*-silenced plants (Delk et al., 2005), for which little or no CML24 protein is detectable, suggests that the E124K mutation in *cml24-4* causes at least a partial loss of CML24 function. In addition, *cml24-3* and *cml24-7* flower later than wild type in 16-hour photoperiods; these mutations may also cause loss of CML24 function (data not shown) (Delk, 2006). *cml24*-5 flowers earlier when grow in high light intensity (110 μmol m^{-2} s^{-1}) but not under low light (50 μmol m^{-2} s^{-1}) in both 16- and 24-hour photoperiods (Delk, 2006). We suspect that this high light-dependent acceleration of flowering is a stress response since these plants are also pale green under high light.

cml24-2 flowers early (Figure 3.1a) and produces fewer rosette leaves prior to flowering (Figure 3.1d) in long-day photoperiods. In short days, *cml24-2* flowering time resembles that of wild type (data not shown). The opposing effect on flowering time of the *cml24-2* and *cml24-4* mutations suggests that the *cml24-2* G67E mutation may result in a gain of function. Consistent with this possibility, *cml24-2* is dominant; plants heterozygous for the mutation also flower early under long-day conditions (Figure 3.2). Together, these data indicate that CML24 may act as a regulatory switch, stimulating flowering when activated and inhibiting flowering when inactive.

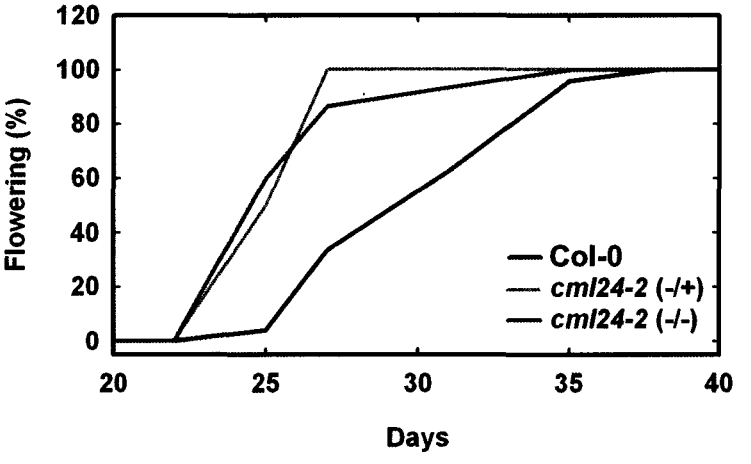

Fig 3.2 The *cml24-2* mutation is dominant with respect to time to flowering transition. Both homozygous (-/-) and heterozygous (-/+) *cml24-2* transition to flowering earlier than wild type (Col-0) when grown in 24-hour light. n ≥6.

3.1.2 *CML23* contributes to flowering regulation under long days

Flowering time and rosette leaf number at flowering are not significantly affected in *cml23-2* or *cml24-1* under long or short photoperiods (Figure 3.1b, d and e). However, when the *cml23-2* and *cml24-1* mutations are combined in double mutants, the transition to flowering in long days is delayed (Figure 3.1a and d). These data indicate that *CML23* and *CML24* have overlapping roles in photoperiod regulation of flowering, *CML23* is dispensable in the presence of wild-type *CML24*, and *cml24-1* is likely a weak allele that manifests a late-flowering phenotype only when *CML23* is also defective.

3.1.3 Double mutants of *cml23* and *cml24* are defective in the autonomous pathway

The double mutants, *cml23-2/cm24-1* and *cml23-2/cml24-4*, also flower later than wild type under short photoperiods, revealing a role for the related Ca^{2+} sensors in the autonomous pathway. Relative to wild type, *cml23-2/cm24-1* and *cml23-2/cml24-4* flower later (Figure 3.1b and c) and produce a greater number of leaves (Figure 3.1e) under short days of 7 or 8 hours of light. These double mutants respond to both vernalization and GA (data not shown), indicating that the *CML23* and *CML24* functions are likely limited to the photoperiod and autonomous pathways regulating flowering time.

3.1.4 *cml23* and *cml24* mutations affect *CO* and *FLC* transcript levels

To begin to dissect where *CML23* and *CML24* act in the photoperiod and autonomous pathways, I analyzed expression of genes implicated in flowering regulation. *FLOWERING LOCUS T* (*FT*) and *SUPPRESSOR OF OVEREXPRESSION OF CONSTANS1* (*SOC1*) integrate regulatory information from both the photoperiod and autonomous pathways and promote flowering (Figure 3.3)

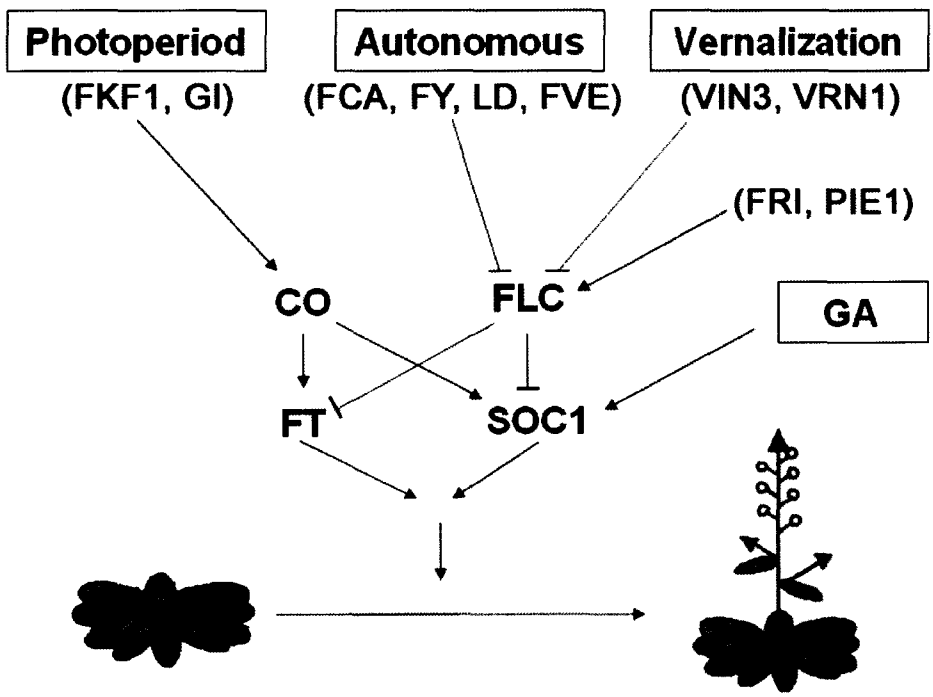

Fig 3.3 Four pathways regulate the transition to flowering: photoperiod, autonomous, vernalization, and gibberellin (GA). Four major genes, *CO*, *FT*, *SOC1*, and *FLC* control flowering time. *FKF1* and *GI* act in the photoperiod pathway as positive regulators upstream of *CO*. *FLC* is negatively regulated by *FCA*, *FY*, *LD*, and *FVE* in the autonomous pathway. *VIN3* and *VRN1* act in the vernalization pathway. *FRI* and *PIE1* are positive regulators of *FLC*.

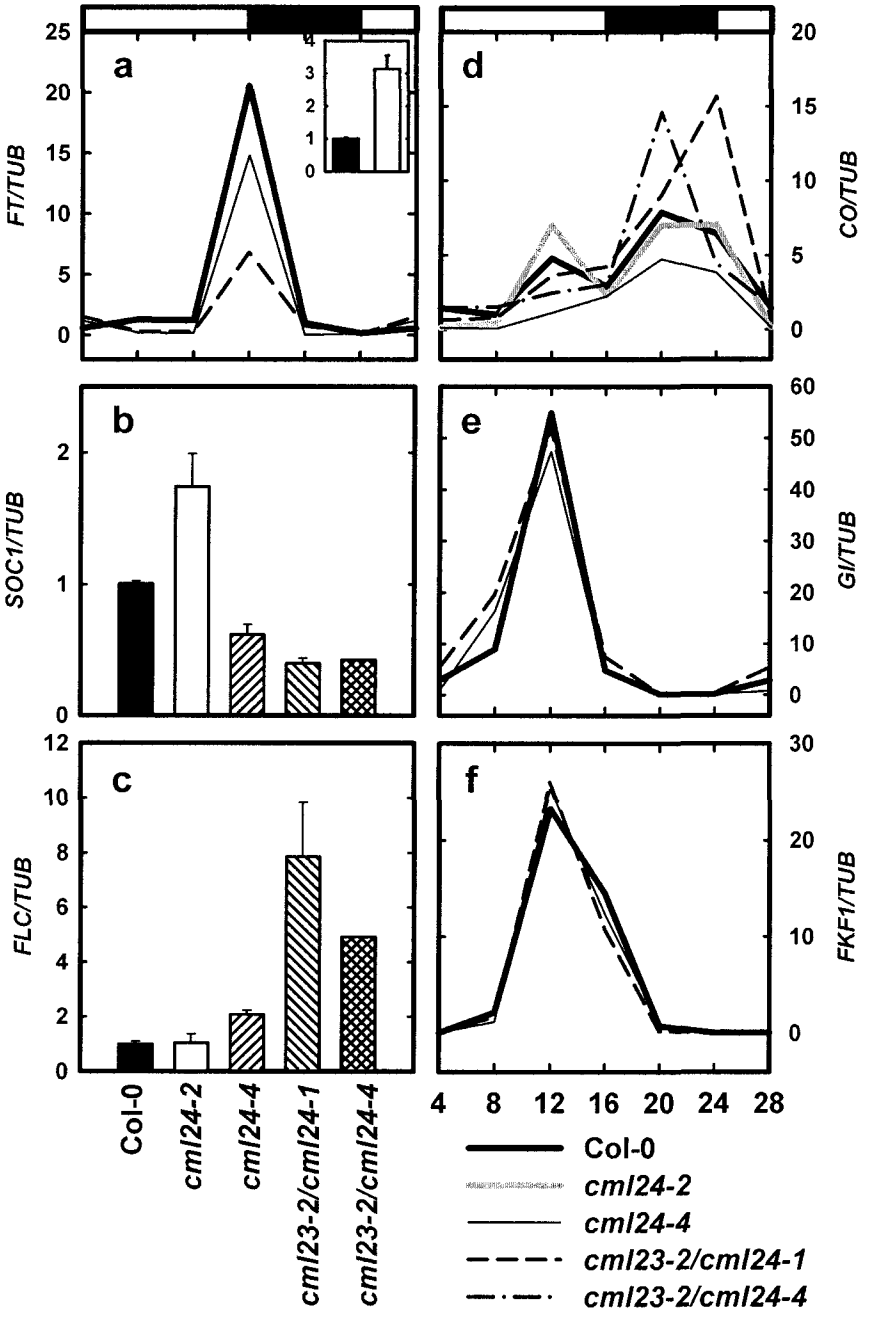

Fig 3.4 Regulation of flowering time gene expression in *cml* mutants. Wild type and *cml* mutants were grown for 2 weeks in 16-hour long-day photoperiods and harvested 11 hours after dawn (a, b, c) or at 4-hour intervals over a 24-hour period (d, e, f). Quantitative RT-PCR was performed to detect abundances of (a) *FT*, (b) *SOC1*, (c) *FLC*, (d) *CO*, (e) *GI*, (f) *FKF1* transcripts relative to *TUB4* (encoding tubulin) transcripts. The light and dark periods for d – f are represented by the open bars and filled bar, respectively, above panel d. (b) (c) Values are means ± SE (n = 3 to 5). (Tsai et al., 2007).

(Mouradov et al., 2002; Simpson and Dean, 2002). The peak of *FT* transcript accumulation that occurs before the start of the dark transition is reduced in two late-flowering mutants analyzed, *cml24-4* and *cml23-2/cml24-1* (Figure 3.4a). *SOC1* expression is reduced in all the late-flowering mutants (Figure 3.4b). In contrast, both *FT* and *SOC1* expression levels are elevated in the early-flowering *cml24-2* mutant (Figure 3.4a and b). This altered gene expression in the *cml* mutants suggests that *CML23* and *CML24* act upstream of these pathway integrators.

FT and *SOC1* expression levels are dependent upon *Constans* (CO) protein activity (Imaizumi et al., 2003; Kardailsky et al., 1999; Kobayashi et al., 1999). CO activity is regulated through coincident signals from the circadian clock and photoreceptors, which convey when the photoperiod is appropriate for flowering (Suarez-Lopez et al., 2001; Yanovsky and Kay, 2002). The late-flowering mutants *cml24-4, cml23-2/cml24-1* and *cml23-2/cml24-4* have reduced *CO* transcript accumulation during the day (Figure 3.4d), the time when *CO* mRNA accumulation can lead to stable and thereby functional protein product (Valverde et al., 2004). *cml24-4* has the strongest effect, with a loss of 76% of the peak *CO* transcripts found in wild type at 12 hours after dawn (Figure 3.4d). *CO* expression levels in *cml23-2/cml24-1* and *cml23-2/cml24-4* are reduced by 24% and 48%, respectively (Figure 3.4d). In contrast, the early flowering mutant, *cml24-2*, has elevated daytime *CO* expression (Figure 3.4d). *CO*, *FT,* and *SOC1* expression levels are comparable to wild type in *cml24-1* (data not shown). Taken together, these data indicate that *CML24* is required for, and *CML23* contributes to, the regulation of *CO* transcript accumulation during the day. The defect in daytime *CO*

expression in the mutants may account, at least in part, for alterations in *FT* and *SOC1* transcript levels and delayed flowering in long-day photoperiods.

Genes that act upstream of *CO* and the circadian clock appear largely unaffected by mutations in *CML23* or *CML24*. Transcripts of *GIGANTEA* (*GI*) and *FLAVIN-BINDING, KELCH REPEAT, F-BOX1* (*FKF1*), which are required for proper *CO* expression (Figure 3.3) (Imaizumi et al., 2003; Mizoguchi et al., 2005; Suarez-Lopez et al., 2001), accumulate with nearly identical diurnal kinetics in wild type, *cml24-4*, and *cml23-2/cml24-1* (Figure 3.4e and f). However, *GI* transcripts do appear to begin to accumulate slightly earlier in the mutants (Figure 3.4e). Leaf movements of the double mutants (*cml23-2/cml24-1* and *cml23-2/cml24-4*) reveal a possible circadian period lengthening (Alex Webb unpublished, University of Cambridge); however, the effect is likely too modest to account for the late flowering behavior. In addition, circadian *CO* expression continues in long-day entrained *cml23-2* and *cml23-2/cml24-4* placed in constant light conditions (data not shown). *CML23* and *CML24*, therefore, are unlikely to play major roles in the regulation of the circadian clock or *GI* or *FKF1* expression; however these paralogous Ca^{2+} sensors may act either downstream or in parallel with these photoperiod pathway components and at a regulatory step upstream of *CO*.

CO expression in wild type reaches a second peak during the night (Figure 3.4d); the mechanism of this regulation is not well defined. *cml24-4* has reduced whereas *cml23-2/cml24-1* and *cml23-2/cml24-4* have higher *CO* expression than wild type during the night (Figure 3.4d). *CO* expression is unaffected in *cml23-2* mutants (data not shown); therefore, *CML23* and *CML24* have functional overlap in the darkness-specific repression

of *CO*. The consequence of aberrant nighttime *CO* expression is, as yet, unclear because CO protein is unstable in the dark (Valverde et al., 2004).

Delayed flowering of *cml23/cml24*double, but not single, mutants in short-day photoperiods (Figure 3.1b, c, and e) indicates that *CML23* and *CML24* have overlapping functions regulating the autonomous pathway. *FLC* transcript levels are elevated several fold in *cml23-2/cml24-1* and *cml23-2/cml24-4* (Figure 3.4c) and altered expression is detectable in the shoot apex (data not shown) where *FLC* is normally expressed (He et al., 2003). These results are consistent with the mutants flowering late in short days (Figure 3.1b, c, and e). The single mutants, *cml23-2*, *cml24-1* and *cml24-4*, show no or only modest increases in *FLC* transcript accumulation (Figure 3.4c and data not shown). The coordinate mis-regulation of both *CO* and *FLC* expression in the double mutants may explain why *FT* and *SOC* expression levels are more strongly affected in, for example, *cml23-2/cml24-1* than in *cml24-4*, which is only modestly affected in *FLC* transcript levels. Although mutation of *CML24* can be sufficient to affect photoperiod-regulated flowering time, the autonomous pathway is affected only when both *CML23* and *CML24* are impaired. Therefore, I concluded that *CML23* and *CML24* act upstream of *FLC* to inhibit expression and thus promote flowering.

The transition to flowering can also be negatively regulated by *FLC* as part of the autonomous and vernalization pathways. Late-flowering mutants *cml23-2/cml24-1* and *cml23-2/cml24-4* have strongly elevated *FLC* expression levels (Figure 3.4c). Several genes are negative regulators of *FLC* and belong to either the autonomous (*FCA*, *FY*, *LD*, and *FVE*) or vernalization (*VIN3* and *VRN1*) pathways (Figure 3.3). *cml23-2/cml24-1* transcript levels of these negative regulatory genes are either elevated or comparable to

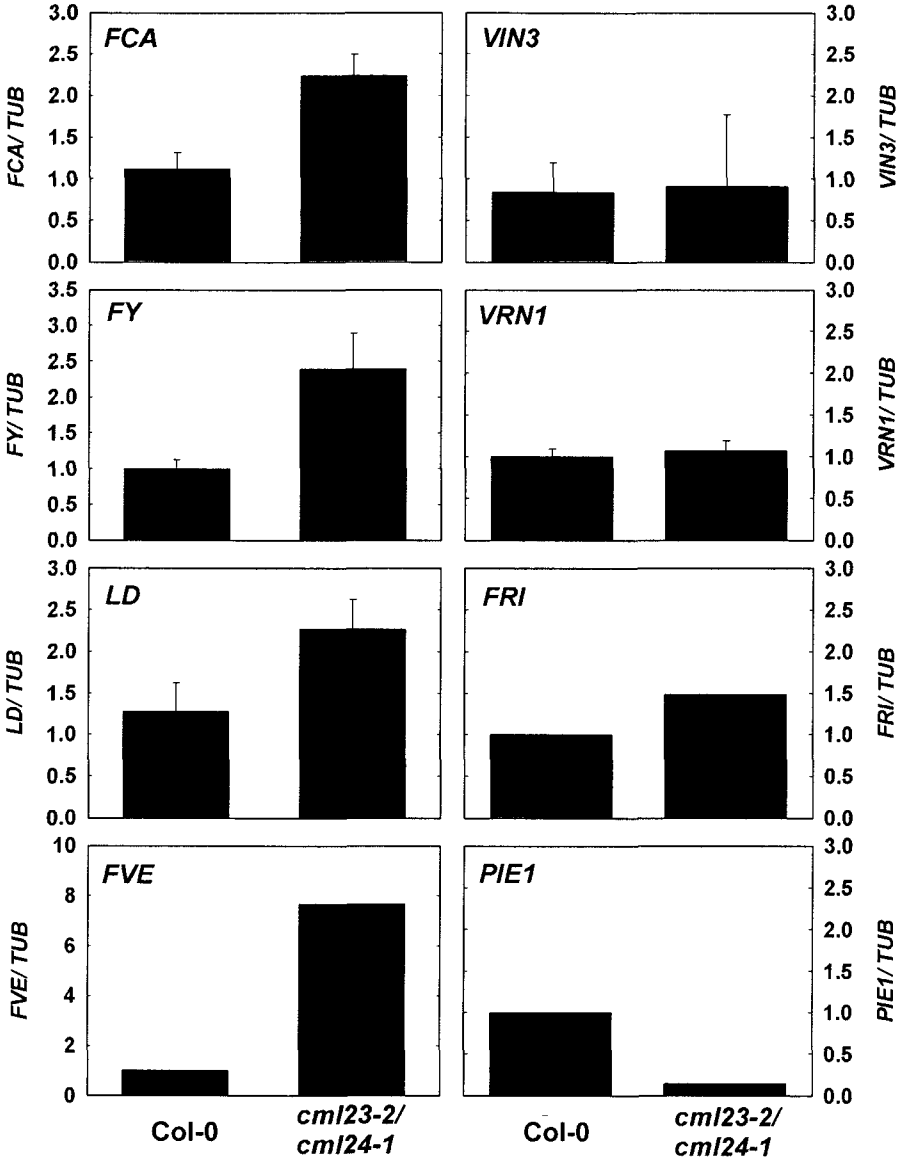

Fig 3.5 Regulation of flowering time gene expression in *cml* mutants. Quantitative RT-PCR of *FCA, FY, LD, FVE, VIN3, VRN1, FRI,* and *PIE1* relative to *TUB4* transcript levels were determined in 2-week-old plants grown under long-day (24-hr) photoperiods. Autonomous genes, *FCA*, *FY*, *LD*, and *FVE*, accumulated higher transcript levels in *cml23-2/cml24-1* relative to wild type (Col-0). *cml23-2/cml24-1* has comparable transcript levels of vernalization pathway genes, *VIN3* and *VRN1*, to wild type. *FRI*, a mutant allele in Col-0, has increased transcript levels in *cml23-2/cml24-1* relative to wild type. *PIE1*, a positive regulator of *FLC*, has decreased transcript levels in *cml23-2/cml24-1* relative to wild type. *FCA, FY, LD, VIN3,* and *VRN1* relative transcript values are means ± SE (n = 3 to 4). *FVE*, *FRI*, and *PIE1* analysis was conducted one time.

wild type (Figure 3.5). Transcript levels of two *FLC* positive regulators (*FRI* and *PIE1*) were also examined; *FRI* had slightly increased RNA levels in *cml23-2/cml24-1* relative to Col-0 (Figure 3.5). However, *FRI* in Col-0 is a mutant allele unable to upregulate downstream *FLC* expression (Johanson et al., 2000); therefore alterations in *FRI* transcript abundance has no likely functional consequence. These results suggest that *CML23* and *CML24* do not act on these upstream *FLC* regulators of the autonomous and vernalization pathways. Instead, *CML23* and *CML24* may influence *FLC* expression through an alternative mechanism.

3.1.5 The *cml24* late flowering mutants accumulate elevated nitric oxide (NO)

Nitric oxide (NO) is known to regulate several plant developmental processes, including the flowering transition (He et al., 2004b). NO delays flowering by positively regulating *FLC* and negatively regulating *CO* expression levels (He et al., 2004b). To check whether the late and early flowering *cml23* and *cml24* mutants are altered in NO levels, I compared staining with NO fluorescence indicator, 4-amino-5-methyl-amino-2',7'-difluorofluorescein (DAF-FM), used primarily for *in vivo* NO measurements (He et al., 2004b) to assess how NO accumulation is affected in the *cml* mutants. Comparable basal fluorescence is detected in wild type, *cml23-2*, *cml24-1*, and *cml24-2* (Figure 3.6a and b). In contrast, the late-flowering mutants, *cml24-4*, *cml23-2/cml24-1*, and *cml23-2/cml24-4*, show elevated fluorescence in detached leaves (Figure 3.6a and b). These data suggest that *CML23* and *CML24* may regulate NO accumulation levels in Arabidopsis. The elevated fluorescence in the late-flowering *cml* mutants is most likely due to higher NO accumulation because incubation with 2-(4-carboxyphenyl)-4,4,5,5-tetra-

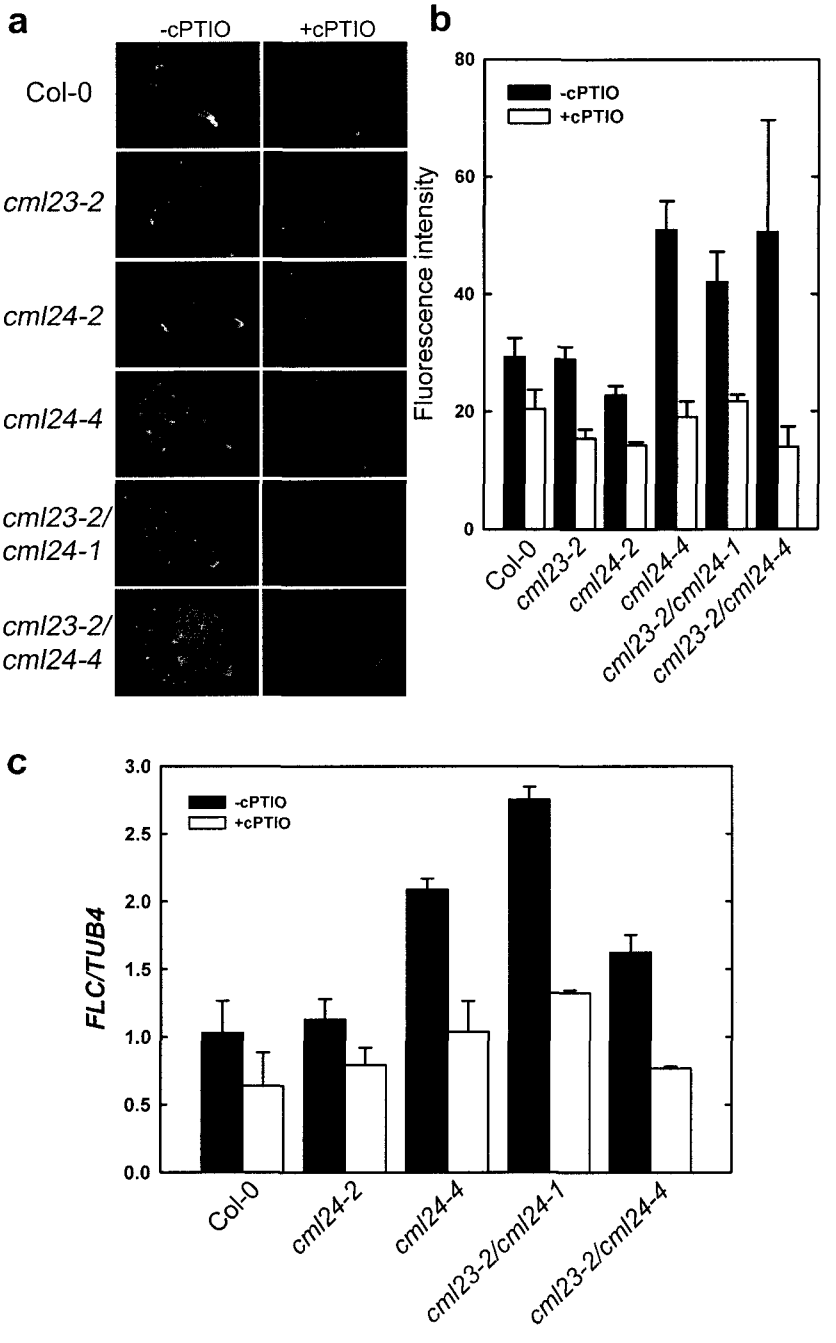

Fig 3.6 *CML23* and *CML24* regulate NO accumulation in leaves and the altered NO levels are responsible for elevated *FLC* transcript levels. (a) Col-0 and *cml* mutants rosette leaves were stained with DAF-FM DA for 45 min. Fluorescence was detected with 490-495 nm excitation and 515 nm emission. (b) Fluorescence intensity was quantified. n=3. (c) Quantitative RT-PCR of *FLC* levels relative to *TUB4* were determined in 2-week-old plants grown under long-day (24-hr) photoperiods and treated with or without 400 μM cPTIO for 4 hours. Values are means ± SE (n = 3 to 4). (Tsai et al., 2007).

methylimidazoline-1-oxyl-3-oxide (cPTIO), an NO scavenger, significantly reduces the DAF-FM fluorescence (Tsai et al., 2007).

To investigate whether the elevated NO levels in the *cml23/cml24* mutants may be responsible for alterations in gene expression, I quantified *FLC* transcript abundance in wild-type and mutant plants grown under a 16-hour photoperiod, and treated with cPTIO to reduce NO levels. A 4-hour cPTIO treatment has no significant effect on *FLC* transcript levels in wild type or *cml24-2* but strongly reduces *FLC* expression in the late-flowering *cml24-4*, *cml23-2/cml24-1* and *cml23-2/cml24-4* mutants (Fig 3.6c). These results suggest that although NO may not be required for basal *FLC* expression, elevated NO is essential for the enhanced *FLC* expression in the late flowering *cml24-4*, *cml23-2/cml24-1* and *cml23-2/cml24-4* mutants.

To test whether the elevated NO levels in *cml23/cml24* mutants are responsible for delayed flowering in short photoperiods, I sprayed cPTIO directly on Col-0, *cml23-2/cml24-1*, and *cml23-2/cml24-4* leaf surfaces and compared flowering times (Figure 3.7). When plants were grown in short-day photoperiods and sprayed with 0.16% MetOH as control, 50% of Col-0 transitioned to flowering before 115 days of growth (Figure 3.7a). Half of the *cml23/cml24* double mutants transitioned to flowering around 130 days after the seed were sown. Plants treated with cPTIO transitioned to flowering earlier than untreated controls (Figure 3.7a and b). With cPTIO treatment, 50% of Col-0 transitioned to flowering 5 days earlier than untreated controls. *cml23-2/cml24-1* and *cml23-2/cml24-4* flowered earlier with cPTIO than untreated controls by 11% (114/128 days) and 4% (125/130 days), respectively (Figure 3.7a and b). The different responses between the two mutants may be because *cml24-1* or *cml23-2/cml24-1* is more sensitive to cPTIO.

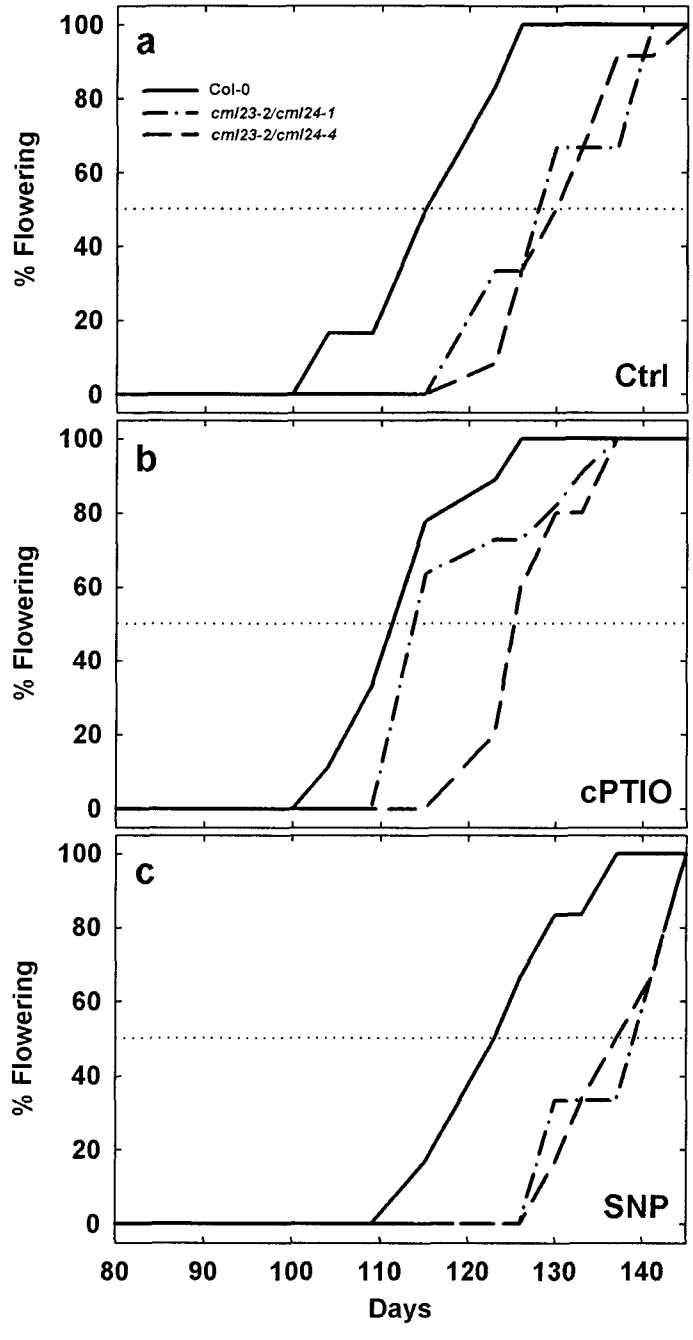

Fig 3.7 Exogenous NO scavenger (cPTIO) and NO donor (SNP) affect Col-0 and *cml23/cml24* double mutants flowering time in short photoperiods. Wild type (Col-0) and mutants were grown in 8-hour photoperiods and sprayed with 0.16% MetOH as control (a), 400μM cPTIO (b), or 50μM SNP (c) twice per week. The percentages of plants flowering over time were recorded. n≥10.

Conversely, Col-0, *cml23-2/cml24-1*, and *cml23-2/cml24-4* treated with SNP, a NO donor, showed around a 7% (123/115 days), 8% (139/128 days), and 5% (137/130 days), respectively, delayed flowering transition relative to untreated controls (Figure 3.7a, and c). These results are consistent with the hypothesis that NO levels influence the timing of the transition to flowering. The timing of the flowering transition is influenced by manipulation of NO in wild type and the *cml* mutants. Therefore, the *cml* mutants remain sensitive to NO levels. Furthermore, the flowering time alterations in the *cml* mutants correlate with NO accumulation levels.

3.2 Amino acid content in the *cml* mutants

3.2.1 Free arginine levels in *cml* mutants do not correlate with NO accumulation

In animal cells, NO synthases catalyze NO production from L-arginine. Whether NO production in plant cells occurs through an L-arginine-dependent mechanism remains controversial (Flores-Pérez et al., 2008; Moreau et al., 2008). However, in the Arabidopsis *nox1* mutant, NO overaccumulation correlates with an 8-fold increase in arginine compared to wild type (He et al., 2004b).

To determine whether NO accumulation in the *cml24* mutants correlates with altered arginine accumulation, I analyzed free amino acid levels in wild type and *cml* mutants in collaboration with Kendal Hirschi (BCM) (Figure 3.8 and Appendix A1). Plants were soil grown in constant light, and two-week-old rosette leaf amino acid levels were quantified by HPLC. Asn and Gln levels were over the set detection limit and thus affected the accuracy of the minimum amino acid detection level; therefore, to confirm the data this analysis will be repeated.

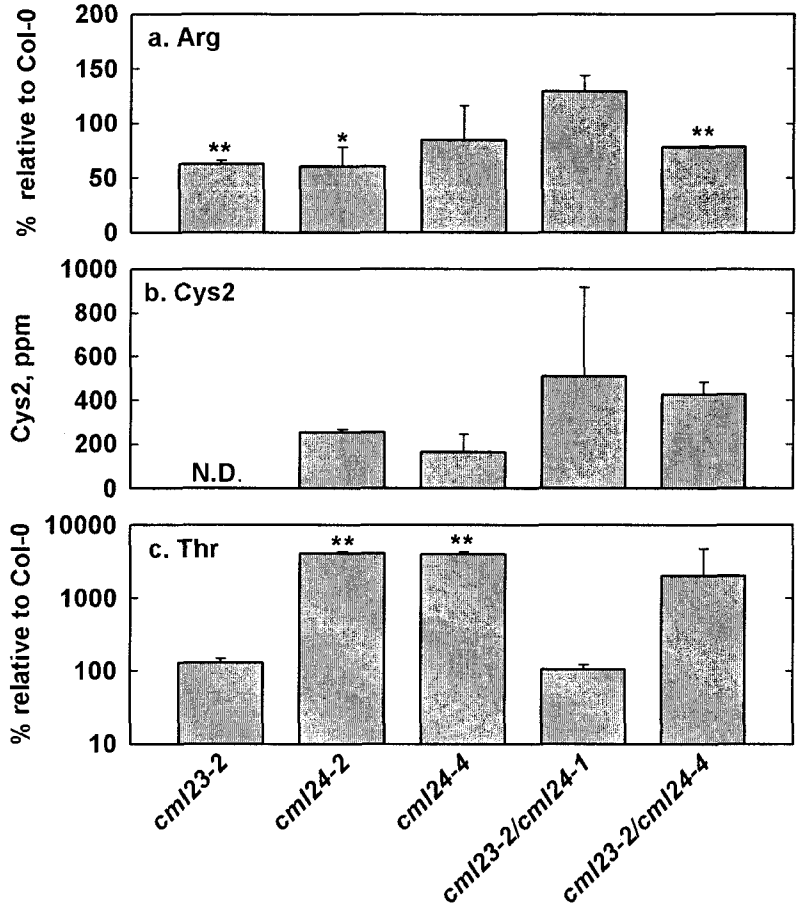

Fig 3.8 Arg, Cys2, and Thr amino acid content in wild type (Col-0) and *cml* mutants. (a) (c) Col-0 extract contained 14774 (84 nmol/g FW) and 501 ppm of Arg and Thr, respectively. Arg and Thr contents in *cml23-2*, *cml24-2*, *cml24-4*, *cml23-2/cml24-1*, and *cml23-2/cml24-4* were quantified relative to Col-0. (b) Absolute content of cystine (Cys2). The Cys2 level was not detectable (N.D.) in Col-0 and *cml23-2*. **$p<0.01$; *$p<0.05$.

Although *cml24-4, cml23-2/cml24-1* and *cml23-2/cml24-4* mutants have higher NO levels than wild type, free arginine levels were not significantly different in *cml24-4* and *cml23-2/cml24-1* relative to Col-0 (Figure 3.8a). *cml23-2*, *cml24-2* and *cml23-2/cml24-4* had significantly lower arginine levels relative to Col-0 (Figure 3.8a), which may suggest defective arginine biosynthesis or degradation. These results indicate that the *cml24* mutants are unlike *nox1* in that high NO levels are not correlated with high arginine. The mechanism whereby the *cml* mutants accumulate high NO remains undetermined. Further investigation into the basis for this phenotype may reveal insight into the outstanding question of how plants generate NO.

3.2.2 *cml24* mutants accumulate cystine

One remarkable difference discovered through the amino acid analysis is that the *cml24* mutants had relatively high levels of oxidized cysteine (cystine, Cys2) (Figure 3.8b). Cystine usually accrues in oxidizing environments and is very insoluble. For example, in animal cells, proteins degraded in the oxidizing environment of the lysosome release cysteine as cystine. Cystine is then transported from the lysosome to the cytoplasm (Gao et al., 2005). In wild type and *cml23-2*, there was no detectable free cystine (Figure 3.8b). In contrast, *cml24-2* and *cml24-4* accumulated 255 and 111 ppm, respectively, of cystine; *cml23/cml24* mutants had over twice as much cystine than *cml24-4* (Figure 3.8b). These results suggest that *cml24* mutations may cause a higher oxidizing state and/or have a higher protein turnover rate than wild type. The accumulation of higher cystine in *cml23-2/cml24-4* than *cml24-4* is consistent with the hypothesis that *CML23* has overlapping functions with *CML24*. This analysis will be repeated to verify the reproducibility of the results.

3.2.3 *cml24* mutants have altered threonine levels

Threonine (Thr) is an essential amino acid that animals cannot synthesize and instead must be obtained through diet. In plants, Thr is synthesized from Aspartate (Asp) (Figure 3.9). Lysine (Lys), Methionine (Met), and S-Adenosylmethionine (SAM) are also produced from Asp. Thr can be further converted to isoleucine (Ile) or degraded to glycine, 2-oxobutyrate, or 2-amino-3-oxobutyrate. *cml24-2* and *cml24-4* accumulated 40 times more Thr relative to wild type (Figure 3.8.c). Both *cml23-2/cml24-1* and *cml23-2/cml24-4* mutants did not have significant Thr accumulation differences relative to wild type, which may indicate *cml23-2* can somehow compensate for *cml24*-caused Thr accumulation. Thr, Lys, and SAM can negatively regulate Asp-derived amino acid synthesis by a negative feedback mechanism. A mutant defective in the key enzyme for Lys synthesis accumulates high Thr levels (Sarrobert et al., 2000). High levels of Thr can be toxic for plant root development (Sarrobert et al., 2000). These results indicate that both CML23 and CML24 may have a role in Thr accumulation. However, the mechanisms responsible for these differences in accumulation and the relevance of these effects remain unclear.

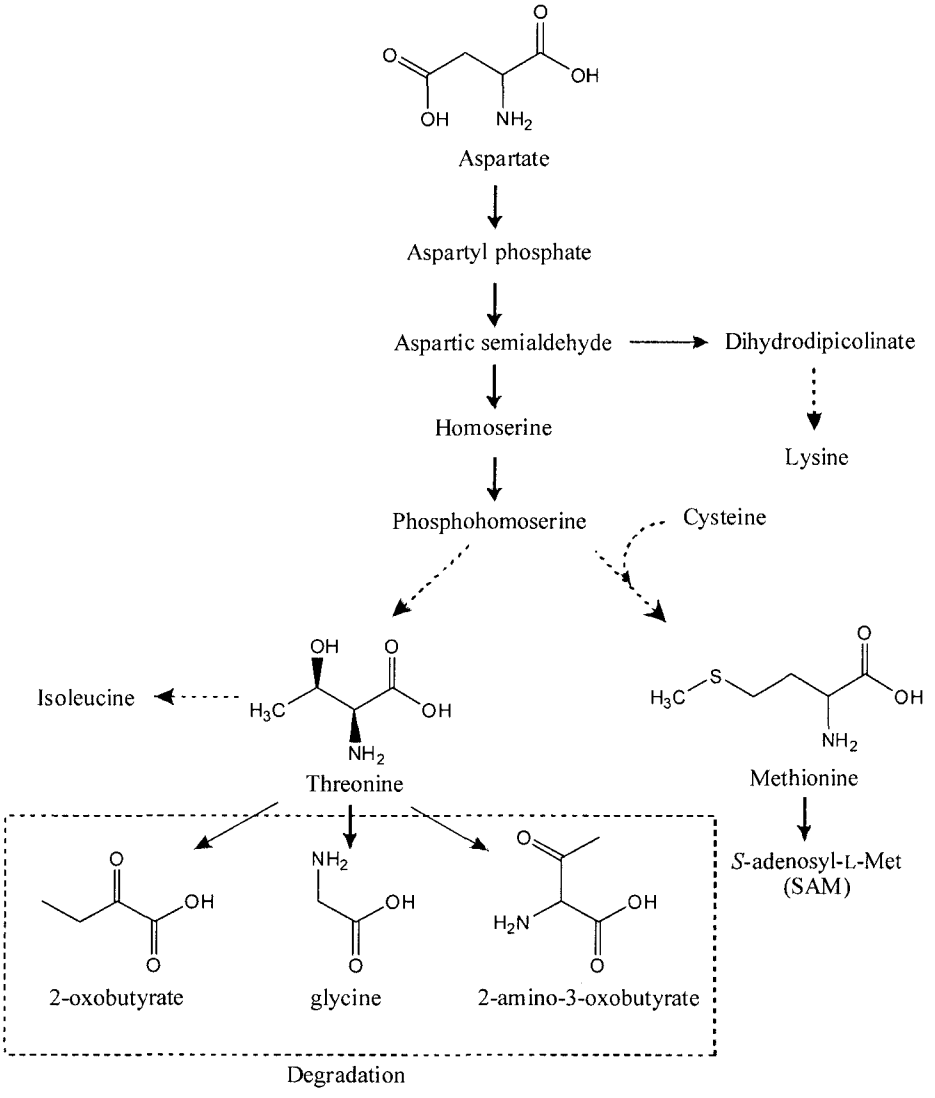

Fig 3.9 Aspartate-derived amino acid biosynthesis and degradation. Arrows with solid lines indicate direct reaction products and arrows with dashed line indicate indirect reactions. Threonine degradation reactions are labeled with a dashed box. Figure was adapted from (Joshi et al., 2006; Kim et al., 2002; Lee et al., 2005; Sarrobert et al., 2000).

3.3 Ionomics analysis

CML24 is a potential Ca^{2+} sensor and therefore may play a role in sensing transient cytosolic Ca^{2+} changes (Delk et al., 2005). Ca^{2+} is essential for ion homeostasis in plants (White and Broadley, 2003). The *CML24* underexpressors have enhanced tolerance to several ions, including Co^{2+}, MoO_4^{2-}, Zn^{2+}, and Mg^{2+} (Delk et al., 2005). The higher tolerance of Mg^{2+} in *CML24* underexpressors is not due to defects of Mg^{2+} uptake (Delk et al., 2005).

In collaboration with David Salt (PiiMS, Purdue University), *cml23* and *cml24* mutants were analyzed with inductively coupled plasma mass spectroscopy (ICP-MS) (Baxter et al., 2007). High-throughput ICP-MS is a powerful tool that enables analysis of most metal ions (Li, B, Na, Mg, K, Ca, Mn, Fe, Co, Ni, Cu, Zn, Cd, Mo, and As) and biologically significant nonmetals (P and Se) in tissue samples (Appendix A2). Although some differences in ion content were reported, there were variations among the genotypes which confused the interpretation of the results. In general, the ionomics analysis did not reveal severe ion deficiency in *cml23* and *cml24* mutants, which may suggest that any metal sensitivity in the *cml* mutants is not due to aberrant ion accumulation.

3.4 Conclusion

CML24 can act as a switch in the response to day length perception; loss-of-function *cml24* mutants are late flowering under long days, whereas apparent gain of CML24 function results in early flowering. CML24 function is required for proper *CONSTANS* (*CO*) expression; components upstream of *CO* in the photoperiod pathway are largely unaffected in the *cml24* mutants. In conjunction with CML23, a related

calmodulin-like protein, CML24 also inhibits *FLOWERING LOCUS C* (*FLC*) expression and therefore impacts the autonomous regulatory pathway of the transition to flowering. Nitric oxide (NO) levels are elevated in *cml24-4* and *cml23/cml24* double mutants and are largely responsible for *FLC* transcript accumulation.

The high NO levels in *cml24* late flowering mutants do not correlate with increased L-arginine levels. Therefore an altered NOS activity is likely not contributing to the NO overaccumulation in the *cml* mutants. *cml24* mutants also accumulate high levels of cystine indicating that *CML24* may have a role in regulating the oxidative cellular state.

The results presented in this chapter reveal overlapping roles for the Arabidopsis CML23 and CML24 potential Ca^{2+} sensor proteins in regulating the transition to flowering and NO accumulation. Thus, CML23 and CML24 may function to integrate signaling information from cytosolic Ca^{2+} to the production and/or degradation of cellular NO, leading to regulation of the transition to flowering in Arabidopsis.

Chapter 4: *CML24*: Role in NO Accumulation

There are two major proposed enzymatic pathways for NO production in plants (Figure 1.4). One pathway requires NOA1 (Guo and Crawford, 2005); the other pathway involves nitrate reductase (Flores-Pérez et al., 2008; Guo et al., 2003). There is no clear evidence for L-arginine derived NO production from NO synthase-like proteins in plants (Corpas et al., 2009b). Mitochondria, chloroplasts, and peroxisomes are organelles also implicated in NO production and/or degradation (Corpas et al., 2009a; Guo and Crawford, 2005; Gupta et al., 2005; Jasid et al., 2006; Planchet et al., 2005).

CML24 affects NO accumulation and, in turn, delays transition to flowering (Tsai et al., 2007), and plays a role in pathogen defense (Ma et al., 2008). However, how *CML24* influences NO accumulation remains unclear.

4.1 *CML24* and putative *NOS/NOA1* pathway

Animal NOS proteins catalyze the oxidation of L-Arg to NO and L-citrulline, and this activity can be inhibited by Arg analogs. Published work suggests that plants also have Arg-dependent NOS activity, which can be inhibited by Arg analogs (Barroso et al., 1999; Corpas et al., 2004; del Rio et al., 2004).

To determine whether a putative Arg-dependent NOS pathway may be required for NO accumulation in *cml24-4*, *cml23-2/cml24-1*, and *cml23-2/cml24-4*, the *cml* mutants were treated with the NOS substrate arginine analog, N^G-monomethyl-L-arginine monoacetate (L-NMMA), which has been reported to act as an inhibitor of the putative NOS-like pathway in plants (Zeidler et al., 2004; Zottini et al., 2007). Plants were grown on PNS plates for 2 weeks and transferred to PNS liquid media with 5 mM L-NMMA or

0.1% methanol as control. After 4 hours incubation, roots were subjected to DAF-FM staining (Figure 4.1). I chose to examine roots because I reasoned that the inhibitor might best be taken up by roots. However, the *cml* mutant roots did not have higher than wild-type levels of DAF-FM fluorescence. *cml24-2* may have lower DAF fluorescence relative to wild type. Furthermore, L-NMMA treatment did not decrease the fluorescence detected; in some samples, the L-NMMA treatment increased DAF-FM fluorescence (Figure 4.1).

These results suggest that either the L-NMMA treatment was not optimal under the conditions used and therefore failed to inhibit the NOS-like pathway or that the NOS-like pathway does not significantly contribute to basal NO levels in wild type and *cml* mutant roots.

4.2 *CML24* and *NOA1* pathway

To address whether *CML24* and *NOA1* act in the same NO-related pathway, I crossed *cml24-4* with *noa1* to monitor genetic interaction. In long photoperiod soil-growth conditions, rosette leaves of *cml24-4* but not *cml24-4/noa1* had higher DAF-FM fluorescence relative to wild type (Figure 4.2a and 4.2b). These data indicate that the *cml24-4* mutant requires *NOA1* for NO over accumulation. Therefore, *CML24* may act upstream of *NOA1* for NO accumulation. In addition, *cml24-4/noa1* resembles *noa1* in that double mutants have pale green and small leaves (data not shown). However, the timing of transition to flowering of *cml24-4/noa1* was intermediate between the late flowering *cml24-4* and early flowering *noa1* mutant. Relative to wild type, *cml24-4/noa1* flowered later and generated more rosette leaves prior to the transition to flowering (Figure 4.2c). We conclude that *NOA1* is required for NO overaccumulation in the *cml24-4* mutant but that the delayed flowering in *cml24-4* is only partially caused by

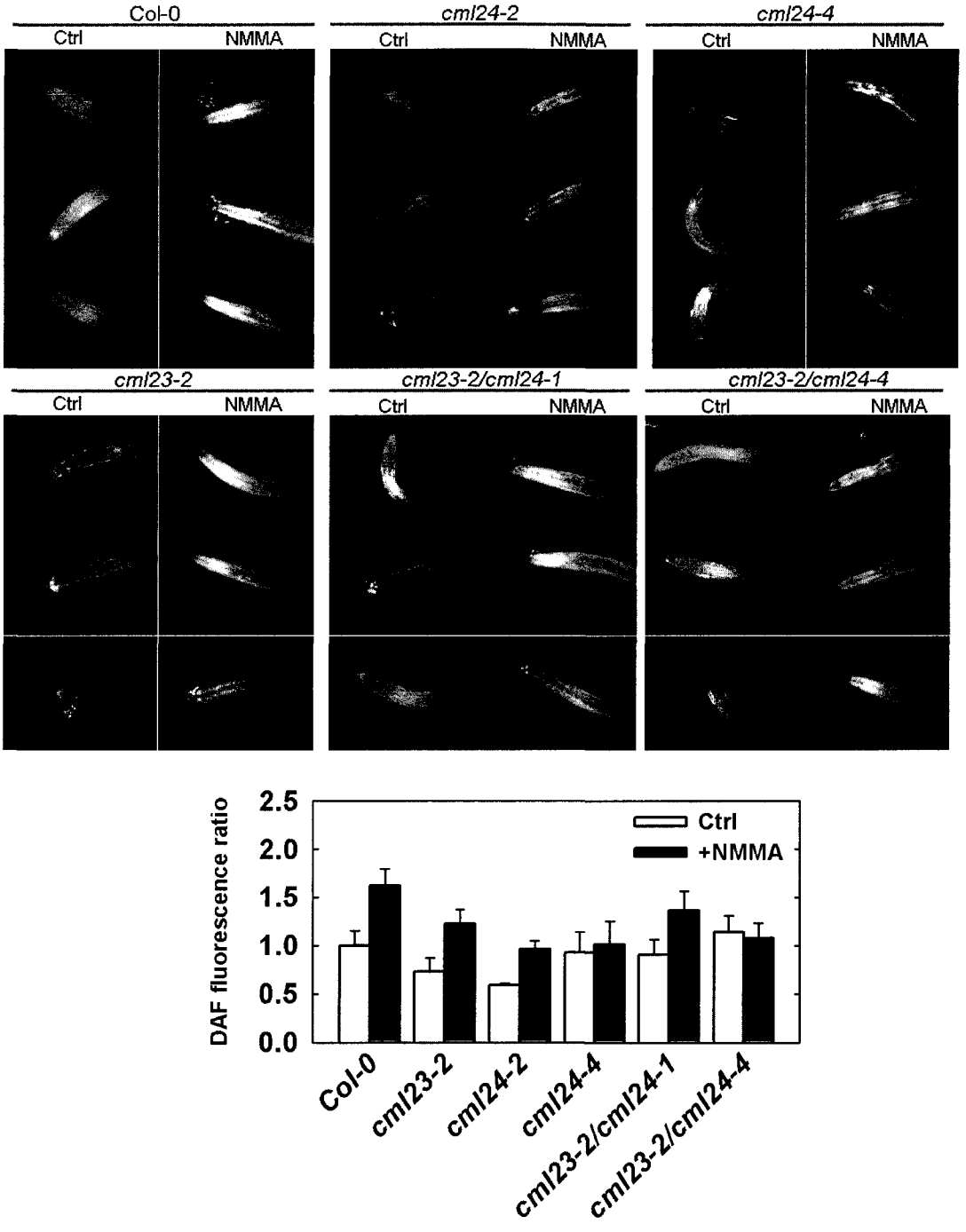

Fig 4.1 L-NMMA does not repress NO accumulation. 2-week-old Col-0 and *cml* mutants were untreated or treated with 5 mM L-NMMA for 2 hours in liquid culture and stained with DAF-FM for 45 min. Fluorescence was detected with 490-495 nm excitation and 515 nm emission. Average fluorescence intensity levels from the roots were quantified using Image J (NIH). n=5.

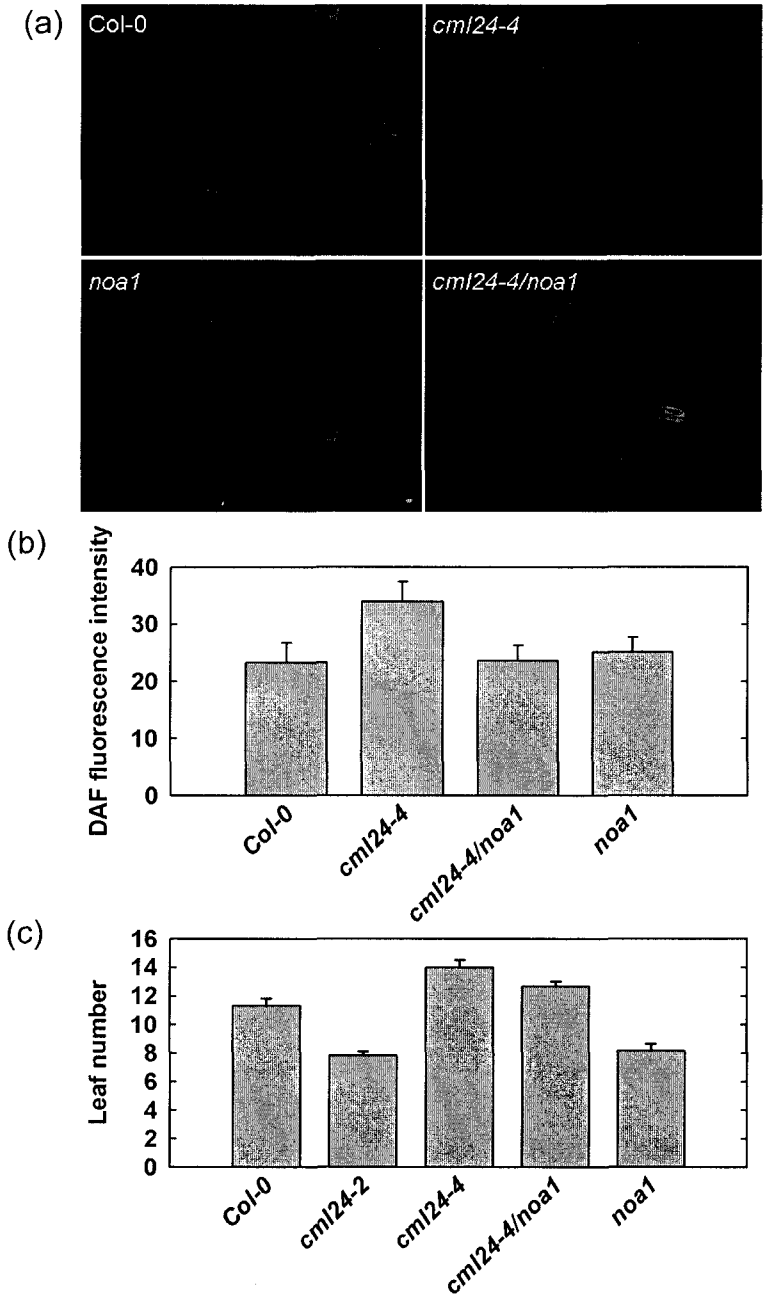

Fig 4.2 NOA1 is required for NO accumulation but is dispensable for the delay of flowering caused by *cml24-4*. (a) Col-0, *cml24-4*, *cml24-4/noa1*, and *noa1* rosette leaves were stained with DAF-FM. DAF-FM fluorescence reports higher basal NO accumulation in *cml24-4*. Two-week-old soil-grown plant leaves were stained with DAF-FM DA for 45 min. Fluorescence was detected with 490-495 nm excitation and 515 nm emission. (b) Average fluorescence intensity levels from the rosette leaves corresponding to the treatments in (a) were quantified using Image J (NIH) $n \geq 5$. (c) Rosette leaf numbers at flowering for plants grown in constant light. $n \geq 9$.

NOA1-dependent accumulation of NO. The *cml24-4* effect on the timing of flowering is partially independent of *NOA1*.

Collaborative experiments with Dan Klessing's lab (Cornell University) found that CML24 does not bind NOA1 in yeast two-hybrid, co-immunoprecipitation, or *in vitro* pull-down experiments (unpublished). In addition, addition of purified CML24 does not affect the enzymatic activity of NOA1 *in vitro* (unpublished). Therefore, it is unlikely that CML24 directly interacts with NOA1. If *CML24* and *NOA1* are in the same pathway, it is likely that any interaction is indirect.

4.2.1 *CML24* and mitochondrial/chloroplast NO production pathway

NOA1 also has been identified as RIF1, which is localized to chloroplasts (Flores-Pérez et al., 2008). Mitochondria and chloroplasts are both potential sources of NO (Gupta et al., 2005; Jasid et al., 2006; López-Figueroa et al., 2000). Electron transfer chain activities may reduce nitrite to NO under certain conditions. Mitochondrial and chloroplast ATP synthases contain similar F_1 complexes composed of five subunits ($\alpha_3\beta_3\gamma\delta\varepsilon$). As an initial examination of organelle integrity in mutants altered in NO accumulation, I used an antibody generated against mouse mitochondrial ATP synthase β subunit (MitoSciences, Oregon) to detect protein levels in Col-0, *cml24-2*, *cml24-4*, *noa1* and *nox*.

Two-week-old seedlings were collected and protein was extracted with LDS (lithium dodecyl sulfate) buffer. LDS prevents protein degradation at low temperature better than SDS because of higher solubility. 50 μg of protein were subjected to SDS-PAGE and western blotting with anti-ATP synthase β subunit antibody. The antibody

detected comparable protein levels in *cml24-2*, *cml24-4* and wild type (Figure 4.3). In strong contrast, however, *noa1* had elevated levels of ATPase β subunit, which suggests that *noa1* has abnormal mitochondria or chloroplasts. Unexpectedly, the *cml24-4* mutation suppressed this defect, as *cml24-4/noa1* has reduced ATPase β subunit accumulation relative to *noa1* (Figure 4.3). These data suggest that the *cml24-4* allele counteracts the *noa1* defect with respect to this phenotype.

These results indicate *noa1* has elevated levels of mitochondrial/chloroplast ATPase. This finding is consistent with the idea that *NOA1* is required for normal function of mitochondria and/or chloroplasts. How *CML24* may affect the abundance of ATPase in *noa1* is unclear.

4.3 CML24 and Nitrate Reductase

Nitrate reductase is another protein implicated in NO production in plants (Meyer et al., 2005). Nitrate reductase has a major role in plant nitrogen assimilation through the reduction of nitrate to nitrite. Genetic and inhibitor studies indicate that nitrate reductase is important for abscisic acid (ABA)- and auxin-induced NO production as well as NO accumulation required for the transition to flowering, cold acclimation, and freezing tolerance (Figure 1.4) (Desikan et al., 2004; Desikan et al., 2002; Kolbert et al., 2008; Kolbert and Erdei, 2008; Seligman et al., 2008; Zhao et al., 2009). Nitrate reductase may contribute to NO production through its role in nitrite production. Nitrite can then be reduced to NO through multiple pathways. In addition, nitrate reductase can itself directly reduce nitrite to NO under some conditions. Nitrate reductase accumulation and activity levels are tightly regulated by exogenous nitrate levels and darkness (Lillo et al., 2004). I

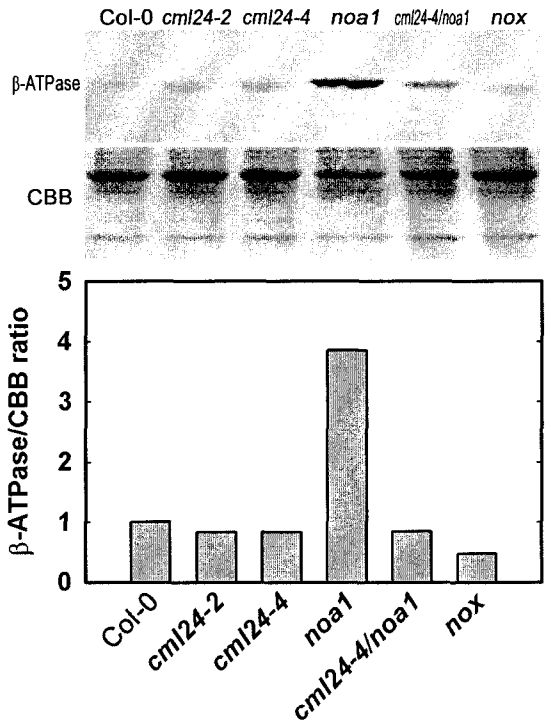

Fig 4.3 β-ATPase protein accumulation levels in wild type, *cml24* and *noa1*. Plants were grown in soil for three week and the rosette leaves were harvested. Proteins were extracted and separated on 13% SDS-PAGE following by western blot with anti-β-ATPase antibody. Total proteins were stained with coomassie brilliant blue (CBB). The intensity of β-ATPase was normalized with CBB staining with Image J (NIH) and Col-0 was defined as 1 for quantification.

am interested in determining whether CML24 regulates NO accumulation through an effect on nitrate reductase.

4.3.1 The *cml24* mutants do not have alter *NIA1* and *NIA2* transcript levels

Nitrate reductase protein is encoded by two genes, *NIA1* and *NIA2*, in Arabidopsis. *NIA2* is more highly expressed during vegetative growth than *NIA1*. *NIA1* transcript levels also decline during the floral transition (Genevestigator). To investigate whether *NIA* expression is affected by *CML24*, *NIA1* and *NIA2* transcript levels were determined from wild type, *cml24-2* and *cml24-4* shoots harvested six hours after shift to light. As expected, *NIA2* transcript levels are much higher than those of *NIA1* in wild type (Figure 4.4a). Transcript levels of *NIA1* and *NIA2* in the *cml24* mutants are indistinguishable from wild type (Figure 4.4a). These results indicate that *NIA1* and *NIA2* expression is not significantly affected by *CML24* and therefore altered NO accumulation in the *cml* mutants is not due to altered *NIA* expression regulation.

4.3.2 The *cml24* mutants do not have altered nitrate reductase activity levels

To determine whether CML24 affects nitrate reductase function post-transcriptionally and thereby affects NO accumulation, I determined both maximum nitrate reductase activity (NR_{max}) and the active nitrate reductase (NR_{act}). In the presence of divalent cations, phosphorylation of nitrate reductase on Ser543 recruits 14-3-3 binding (Aitken, 1996) and inactivates nitrate reductase (Kaiser et al., 1999). Nonphosphorylated nitrate reductase (NR_{act}) consumes NAD(P)H and catalyzes the reduction of nitrate to nitrite (Kaiser et al., 1999).

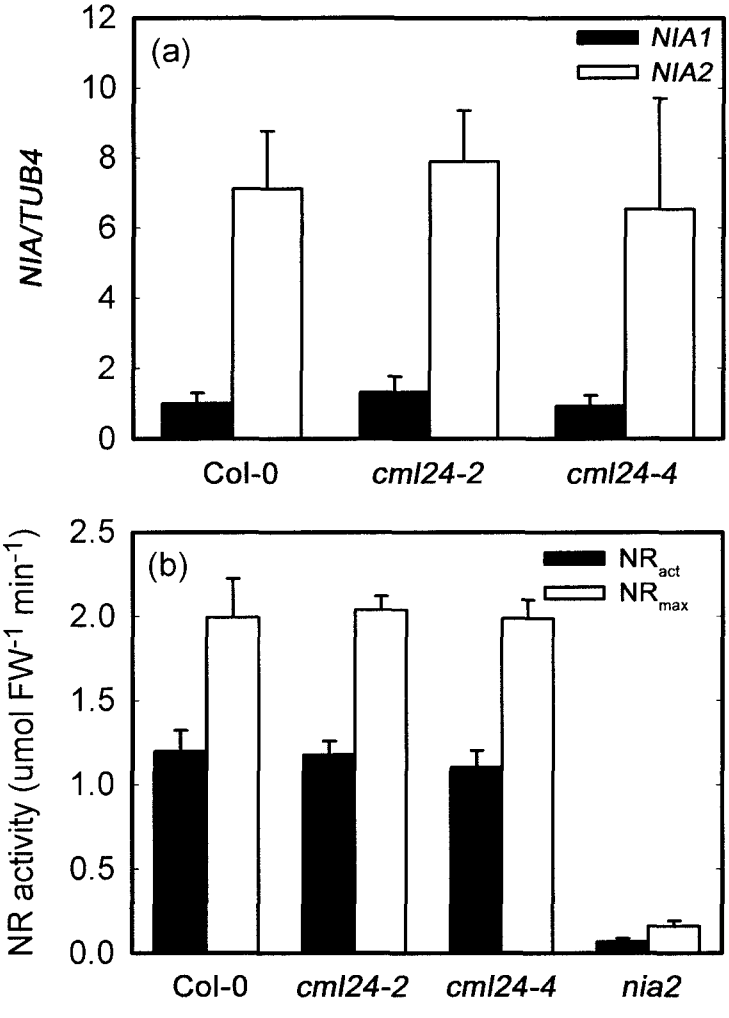

Fig 4.4 *NIA* transcript and nitrate reductase activity analysis in wild type and *cml* mutants. (a) Q-PCR of *NIA1* and *NIA2* transcript levels relative to *TUB4* transcripts were determined in 2-week-old plants. (b) Both NR_{max} and NR_{act} activity were measured. NR_{max} represents the total amount of functional NR. NR_{act} represents the proportion of nonphosphorylated NR.

To measure NR_{act}, $MgCl_2$ was added into each reaction. To fully activate NR (NR_{max}), a reaction was mixed with EDTA to chelate divalent cations. NR_{act} and NR_{max} activity were determined in extracts from three-week-old plants grown under 16-hour photoperiods in soil. Approximately 50% of the total nitrate reductase is apparently nonphosphorylated in wild type (Figure 4.4b). I used *nia2* as a control; *nia2* reports only 10% of wild type NR_{act} and NR_{max} activity (Figure 4.4b), which is consistent with a previous report (Wilkinson and Crawford, 1993). *cml24-2* and *cml24-4* had similar proportions of NR_{act} to NR_{max} as wild type (Figure 4.4b). These results indicate that the altered accumulation of NO in *cml24* mutants is not correlated to alterations in extractable nitrate reductase activity.

4.4 Conclusion

In this chapter, I attempted to link CML24 to potential NO production pathways. I found that although NO accumulation in *cml24-4* requires *NOA1*, CML24 is unlikely to directly interact with NOA1. If *CML24* and *NOA1* are in the same pathway, it is likely that their interaction is indirect. *cml24-4/noa1* revealed an intermediate flowering between *cml24-4* and *noa1* and abated ATPase accumulation in mitochondria and/or chloroplasts relative to *noa1*.

In addition, *CML24* regulation of NO accumulation occurs independently of transcriptional *NIA* regulation, total nitrate reductase protein accumulation, or nitrate reductase activity level regulation.

NO accumulation may also be regulated by degradation or scavenging. Plant hemoglobin can bind and remove NO (Figure 1.4) (Hebelstrup and Østergaard-Jensen, 2008). Bernadette Gehl, a postdoctoral researcher in the Braam lab, determined that

hemoglobin transcript levels in the *cml24* mutants are comparable to wild type. Thus, CML24 regulation of NO accumulation may not be due to increased NO scavenging through hemoglobin function.

CML24 is one of several genes implicated in NO accumulation regulation in Arabidopsis. As the mechanisms and machinery that catalyze NO production remain uncertain, further insight into CML24 function may shed light of NO regulation in plants.

Chapter 5: Biochemical Analysis of CML24

5.1 CML24 structure

In many organisms, Ca^{2+} signals are sensed by calmodulin (CaM). CML24 shares 44% amino acid identity with CaM and, like CaM, has 4 EF hand Ca^{2+}-binding domains (Braam and Davis, 1990; Khan et al., 1997) (Figure 1.1). To assess whether CML24 has homologs in other plant species, I used the Blast program (http://blast.ncbi.nlm.nih.gov/Blast.cgi) to search for CML24-related proteins. Protein sequence alignments with ClustalX program (Larkin et al., 2007) reveals protein conservation. The top seven ESTs that encode more than 70% amino acid identity with CML24 cluster with CML24. Unlike most plant CaMs, which contain only one Cys, CML24 protein contains 4 Cys at positions 11, 126, 131 and 145 (Figure 1.1 and 5.1a). Cys126 and Cys131 are predicted to form a disulfide (Khan et al., 1997). The seven CML24-related proteins also have the analogous 4 Cys residues (Figure 5.1a and b). An additional 17 CML24-related proteins also have cysteines analogous to CML24. This phylogenetic analysis indicates that the Arabidopsis CML24 may have orthologs are conserved in *Brassica* and *Raphanus* within *Brassicaceae* (Figure 5.1b). A closely related CML24-like protein is also encoded in *Zea mays* (Figure 5.1b).

Based on CML24 protein modeling predictions, Cys126 and Cys131 are close enough in space for disulfide bond formation (Khan et al., 1997). Formation of a disulfide is predicted to stabilize the Ca^{2+}-bound conformation of CML24 and therefore is predicted to affect CML24 function. SUBA (Heazlewood et al., 2007), based on mass spectroscopy and primary sequence predictions, reports that CML24 may be located in

(a)

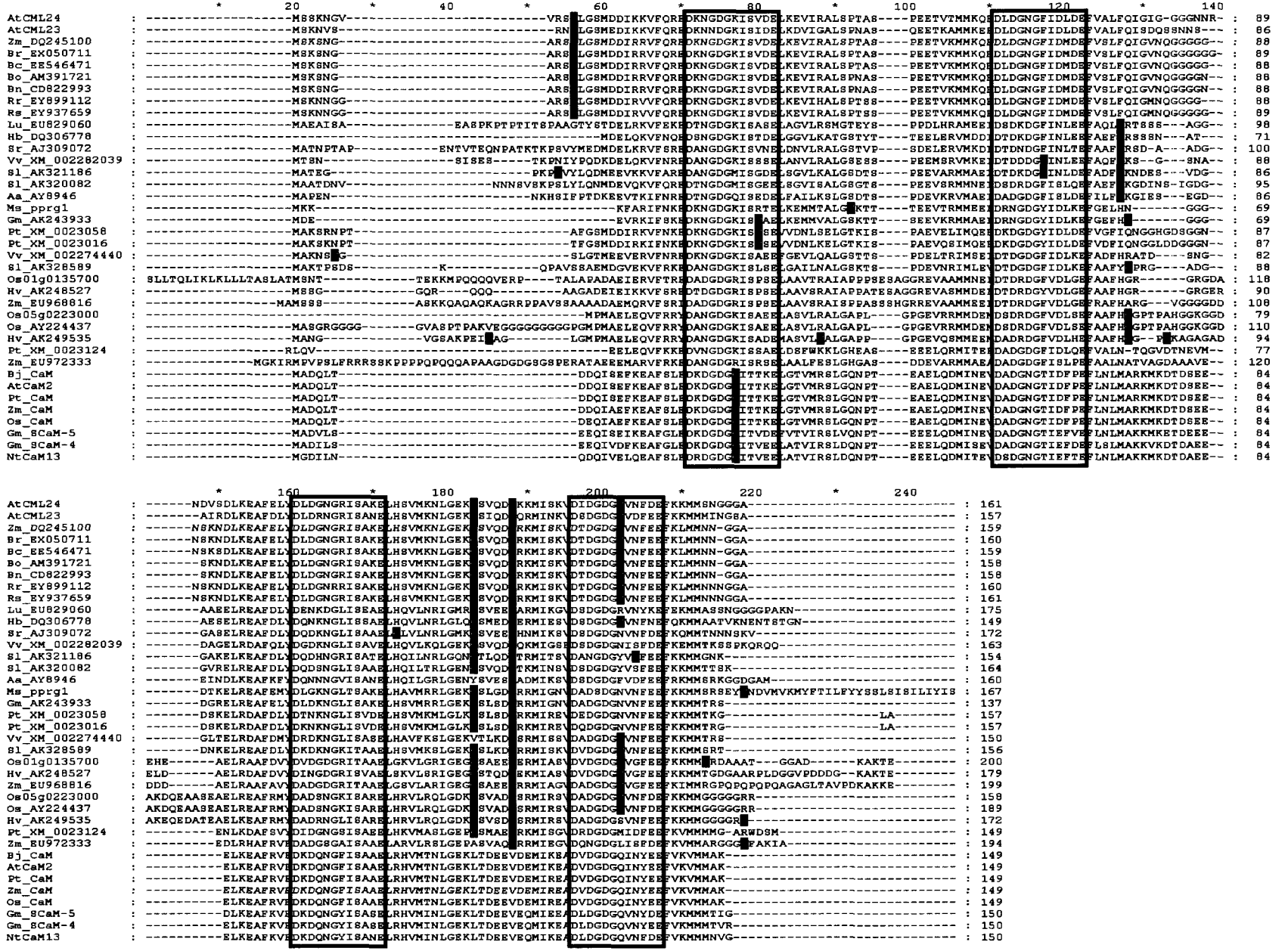
AtCML24
AtCML23
Zm_DQ245100
Br_EX050711
Bc_EE546471
Bo_AM391721
Bn_CD822993
Rr_EY899112
Rs_EY937659
Lu_EU829060
Hb_DQ306778
Sr_AJ309072
Vv_XM_002282039
Sl_AK321186
Sl_AK320082
Aa_AY8946
Ms_pprg1
Gm_AK243933
Pt_XM_0023058
Pt_XM_0023016
Vv_XM_002274440
Sl_AK328589
Os01g0135700
Hv_AK248527
Zm_EU968816
Os05g0223000
Os_AY224437
Hv_AK249535
Pt_XM_0023124
Zm_EU972333
Bj_CaM
AtCaM2
Pt_CaM
Zm_CaM
Os_CaM
Gm_SCaM-5
Gm_SCaM-4
NtCaM13

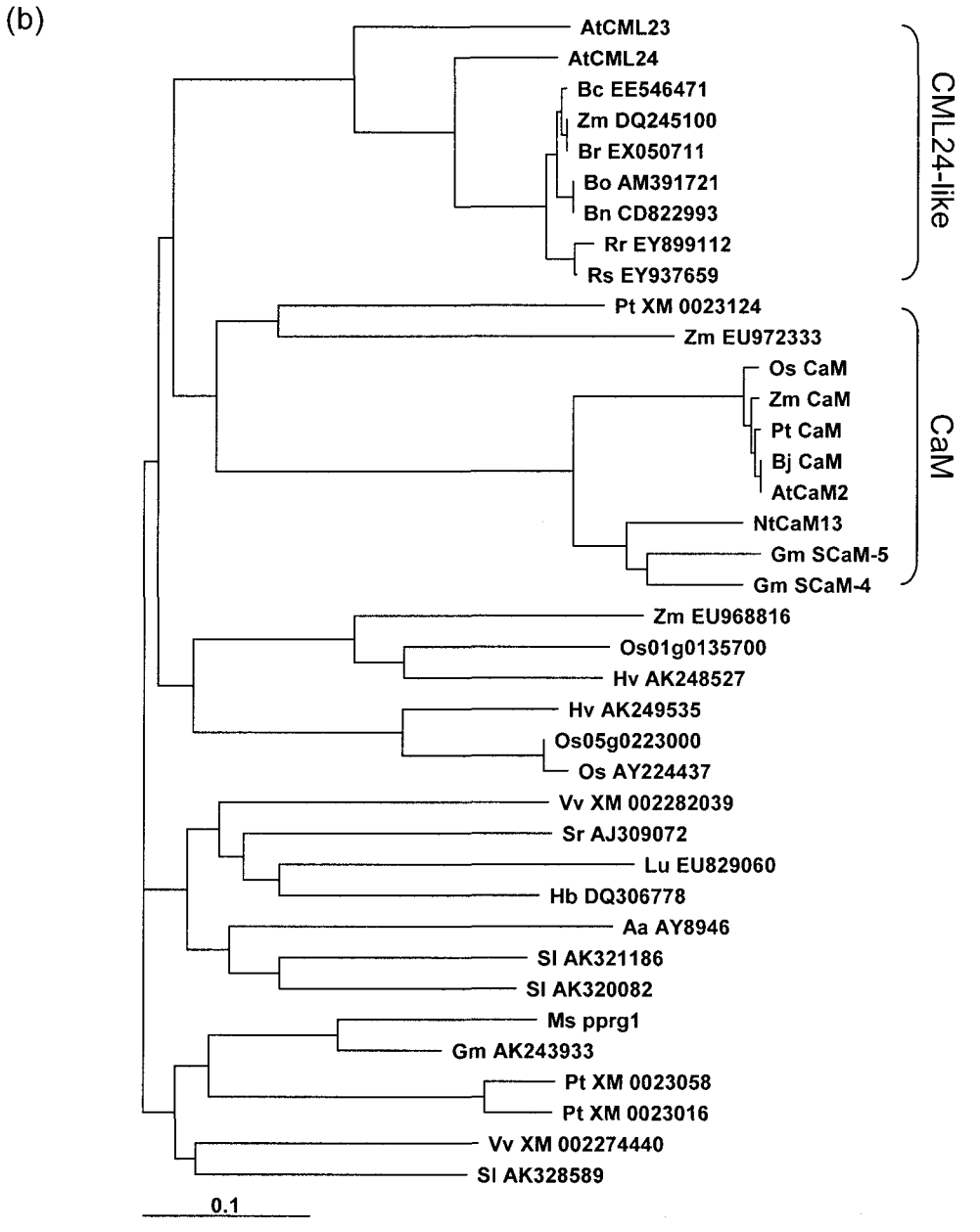

Fig 5.1 Multiple alignment and phylogenetic analysis of CML24 homologous proteins in other plant species. (a) The amino acid sequence of CML24 was aligned against sequences giving significant BLAST similarity scores using ClustalX. The red boxes indicate EF-hand Ca^{2+} binding domains. The cysteine residues are highlight in black. The first two letters of the acronyms indicate the species (Aa, *Ambrosia artemisiifolia*; At, *Arabidopsis thaliana*; Bc, *Brassic carinata*; Bn, *Brassica napus*; Br, *Brassica rapa*; Bo, *Brassica oleracea*; Gm, *Glycine max*; Hb, *Hevea brasiliensis*; Hv, *Hordeum vulgare*; Lu, *Linum usitatissimum*; Ms, *Medicago sativa*; Nt, *Nicotiana tabacum*; Os, *Oryza sativa*; Pt, *Pouplus trichocarpa*; Rr, *Raphanus raphanistrum*; Sl, *Solanum lycopersicum*; Sr, *Sesbania rostrata*; Vv, *Vitis vinifera*; Zm, *Zea mays*). (b) Trichotomy phylogenetic tree showing the evolutionary relationships among the sequences in (a). The analysis was generated with ClustalX, and the tree was drawn with the TREEVIEW program. The distance indicated by "0.1" refers to the percent sequence divergence.

the plasma membrane, cytosol, mitochondria and nucleus (Figure 1.2). As these cellular locations would be expected to be mostly reducing environments, it is unclear whether a disulfide could form. One possibility is that a disulfide would form in CML24 in a transient redox-sensitive manner. The alteration in structure could then alter function. CML24, therefore, may function as both a Ca^{2+} and redox sensor in cells. In this chapter, I evaluate the biochemical characteristics CML24 that relate to its potential as a Ca^{2+} and/or redox sensor.

5.1.1 CML24 changes conformation upon Ca^{2+} binding

To study the potential consequences of the *cml24* point mutations on CML24 function, I investigated the Ca^{2+}-binding ability of the wild-type and mutant CML24 isoforms. I generated *CML24*, *cml24-2*, and *cml24-4* expression constructs to produce the proteins in *E. coli*. Proteins were purified with Ca^{2+}-dependent chromatography using phenyl sepharose. Wild-type and mutant CML24 isoforms bound the resin in a Ca^{2+}-dependent manner, indicating that the mutant proteins maintained the ability to expose hydrophobic domains as a response to binding Ca^{2+}.

Like CaM, Ca^{2+} sensors change conformation in the presence of Ca^{2+}. The conformation change can be detected by mobility shifts in SDS-PAGE. CML24, detected by western analysis of wild-type extracts, also shows a Ca^{2+}-dependent mobility shift in SDS-PAGE (Delk et al., 2005; Tsai et al., 2007). To assess whether the amino acid substitutions in the mutant cml24-1, cml24-2, and cml24-4 isoforms affect Ca^{2+} binding and conformational change, I conducted western analysis of protein extracts from wild type (Col-0), *cml24-1*, *cml24-2*, and *cml24-4* plants, and purified recombinant CML24

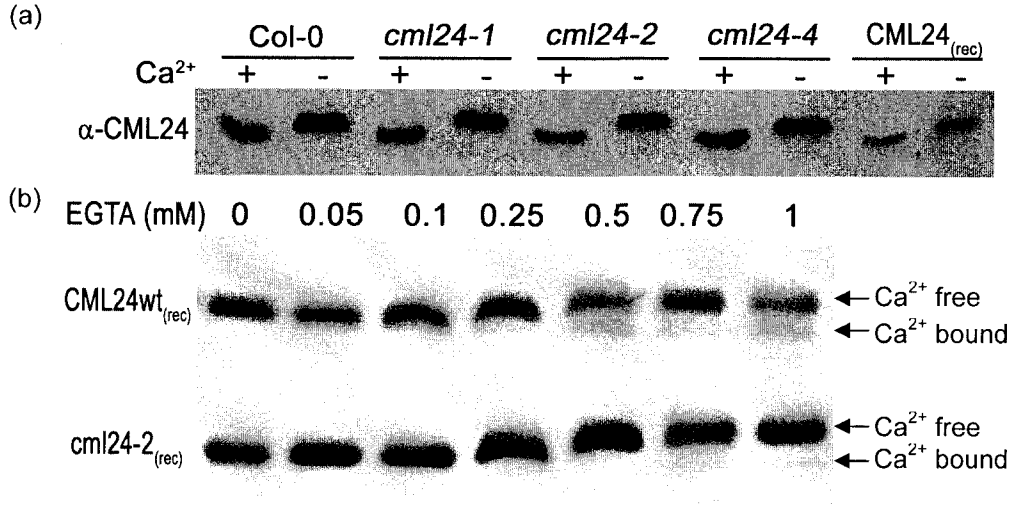

Fig 5.2 Comparison of wild-type and mutant CML24 isoform migration in SDS-PAGE. (a) Western analysis of protein extracted from the roots of Col-0, *cml24-1*, *cml24-2* and *cml24-4* incubated with either 5 mM $CaCl_2$ (+) or 5 mM EGTA (-) and subjected to 13% SDS-PAGE. (b) Coomassie blue staining of purified recombinant wild-type CML24 and cml24-2 protein incubated with increasing concentrations of EGTA and subjected to 13% SDS-PAGE.

from bacteria (Figure 5.2a). All isoforms of CML24 migrate faster through SDS-PAGE in the presence of 5 mM $CaCl_2$ (+, Figure 5.2a) compared to protein in the presence of 5 mM EGTA (-, Figure 5.2a). Recombinant CML24 purified from *E. coli* ($CML24_{(rec)}$, Figure 5.2a) migration behavior is used as a reference. These results indicate that cml24-1, cml24-2, and cml24-4 amino acid substitutions do not block the protein's ability to bind Ca^{2+} and undergo conformational change. However, subtle alterations in Ca^{2+} binding affinity and/or conformation may not be detected under these conditions.

I was interested in analyzing the Ca^{2+}-binding ability of cml24-2 in particular, since this mutant has a substitution in a highly conserved EF hand residue (Gly 67 to Glu); this substitution would be predicted to eliminate Ca^{2+} binding by that EF hand. Therefore, I sought to detect if there were potential subtle differences in Ca^{2+}-binding of cml24-2 as compared with wild type CML24. Recombinant wild-type CML24 and cml24-2 proteins were resuspended in buffer containing 1 mM $CaCl_2$ after purification and then aliquots were incubated with increasing concentrations of EGTA before SDS-PAGE analysis (Figure 5.2b). The coomassie blue stained gel shows that both CML24 and cml24-2 begin to shift in migration rate starting at 0.25 mM EGTA. However, a greater proportion of wild-type CML24 remains in the faster-migrating form, the Ca^{2+}-binding form, even at high EGTA concentrations (e.g., 1 mM, Figure 5.2b) compared to recombinant cml24-2. These results suggest that the cml24-2 G67E substitution of the highly conserved glycine within the second Ca^{2+}-binding domain may affect Ca^{2+} affinity and/or ability to undergo conformational change. This structural defect may underlie the physiological effects observed in *cml24-2* mutant plants.

5.1.2 CML24 can form a disulfide bond

To determine if cysteine residues of CML24 can form a disulfide, I sought to determine the number of reduced cysteines in purified recombinant CML24 *in vitro*. CML24 has four cysteines. Free and reduced thiols of cysteines, not cysteines in a disulfide, can be carboxyamidated with iodoacetamide (IAM). The number of carboxyamidated groups added by incubation with IAM can be determined by liner mode mass spectroscopy (AutoFlexII, Burker). Mass spectroscopy of recombinant wild-type CML24 treated at 99°C for 5 min reveals the average mass of native unmodified CML24 to be 17324 Da (Figure 5.3, green trace). CML24, treated with 25 mM IAM for one hour in the dark to carboxyamidate free thiol groups, has a peak mass of 17438, indicating that two carboxyamidated groups of 58 Da are adding to the protein. This result suggests that only two cysteine thiols were available for carboxyamidation modification (Figure 5.3, blue trace). To reduce any oxidized cysteines, one aliquot of CML24 was pre-incubated with 5 mM of DTT at 37°C for 10 min prior to carboxyamidation with 25 mM IAM (Figure 5.3, orange trace). After the DTT treatment, four carboxyamidated groups were detected on CML24, causing a 227 Da mass shift. These data indicate that purified recombinant CML24 contains only two free cysteine thiols; the other two cysteines are likely oxidized, consistent with the presence of a disulfide bond.

To identify which two cysteine residues may form a disulfide bond, I performed mass spectroscopy with the reflector mode MALDI-TOF-MS (Autoflex II) to detect trypsin-digested peptides from carboxyamidation modified CML24. Trypsin is a serine protease, which specifically cuts after lysines and arginines (Rice et al., 1977). The predicted trypsin-digested peptides of native CML24 are listed in Table 5.1. The four

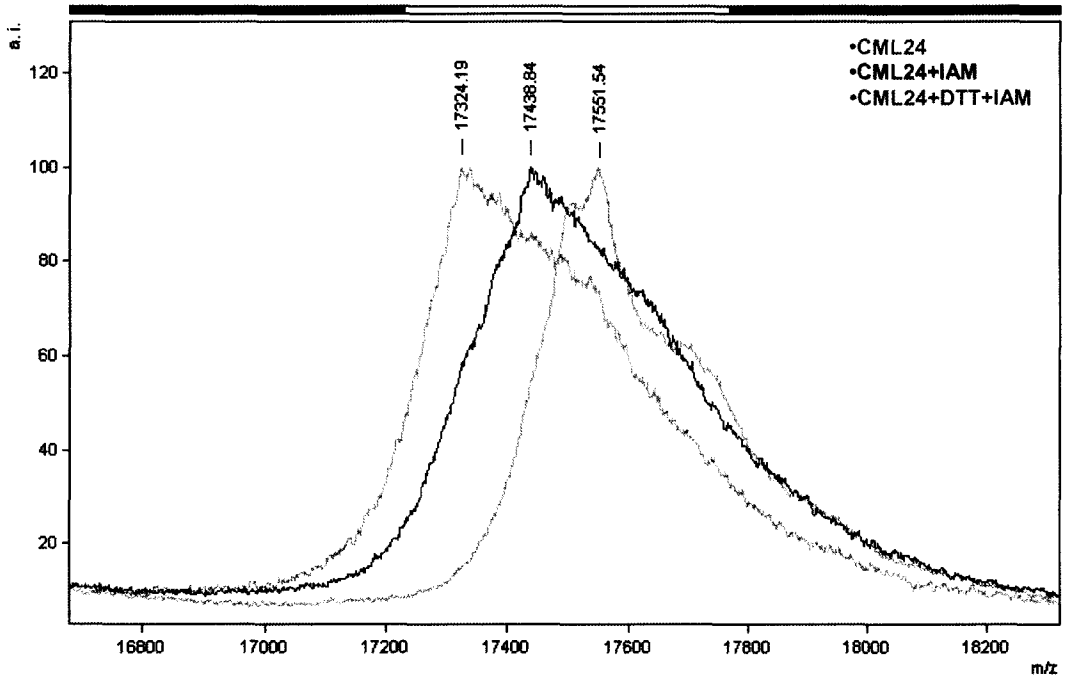

Fig 5.3 Assessment of the number of reduced Cys in recombinant CML24 proteins. Purified recombinant wild-type CML24 was subjected to 99°C for 5 min (green trace), to IAM at 37°C for an hour (blue trace), or to DTT at 37°C for 10min followed by IAM at 37°C for an hour (orange trace). Proteins were analyzed with a MALDI-TOF mass spectrometer (Autoflex). The top black box indicates the full captured mass spectra range (15000-20000 m/z) and the white box represents the region shown in the figure. Intensity is indicated on the y-axis; mass-to-charge (m/z) is on the x-axis.

Table 5.1 Predicted trypsin digestion fragments of CML24

Fragment	Position	Monoisotopic mass	Amino acid sequence
1	[1-4]	452.22	MSSK
2	[5-9]	544.32	NGVVR
3	[10-20]	1196.57	SCLGSMDDIKK
4	[10-20]	1254.57	SCLGSMDDIKK (1x Carboxyamidation)
5	[21-24]	549.31	VFQR
6	[25-27]	409.21	FDK
7	[28-32]	490.23	NGDGK
8	[33-39]	803.45	ISVDELK
9	[40-43]	516.31	EVIR
10	[44-59]	1692.82	ALSPTASPEETVTMMK
11	[60-89]	3198.55	QFDLDGNGFIDLDEFVALFQIGIGGGGNNR
12	[90-96]	790.39	NDVSDLK
13	[97-109]	1498.68	EAFELYDLDGNGR
14	[110-113]	418.27	ISAK
15	[114-120]	843.44	ELHSVMK
16	[121-125]	560.3	NLGEK
17	[126-133]	910.41	CSVQDCKK
18	[126-133]	1026.42	CSVQDCKK (2x Carboxyamidation)
19	[134-137]	478.27	MISK
20	[138-153]	1800.81	VDIDGDGCVNFDEFKK
21	[138-153]	1858.82	VDIDGDGCVNFDEFKK (1x Carboxyamidation)
22	[154-161]	724.28	MMSNGGGA

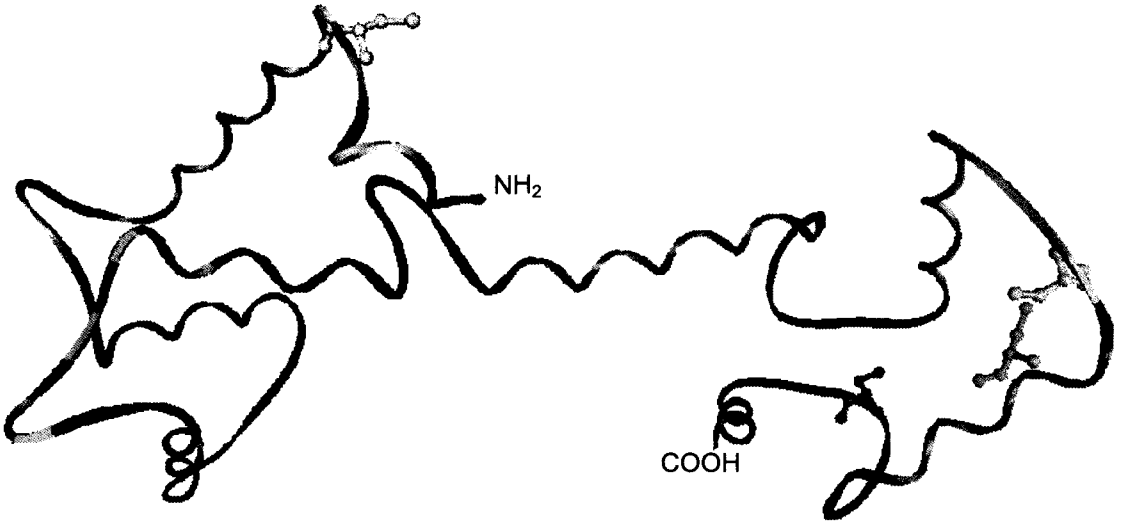

MSSKNGVVRSCLGSMDDIKKVFQRFDKNGDGKISVDELKEVIRALSPTASPEETVTMMKQFDLDGNGFIDLDEFVALFQIG
IGGGGNNRNDVSDLKEAFELYDLDGNGRISAKELHSVMKNLGEKCSVQD KKMISKVDIDGDGCVNFDEFKKMMSNGGGA

Fig 5.4 Prediction of CML24 three-dimensional structure. CML24 3-D structure was predicted basing on amino acid sequence analysis and comparison to potato calmodulin protein structure (PBD_1RFJ) by PredictProtein server (Rost et al., 2004). CML24 amino acid sequence is shown at the bottom. The oranges regions indicate the peptides containing the Cys residue(s) (colored yellow) after trypsin digestion. The blue region represents the fragment contains the second EF-hand after trypsin digestion and green residues are predicted as Ca^{2+}-binding sites/loop (underlined).

cysteine residues would be in peptides 3, 17, and 20 (Table 5.1 and Figure 5.4). Peptide 17 harbors two of the four cysteines (Cys126 and Cys131). All three peptides contain two lysine residues next to each other; this arrangement often causes incomplete trypsin digestion. Carboxyamidated of all four cysteines with IAM would eliminate peptides 3, 17, and 20 and instead generate peptides 4, 18, and 21, respectively (Table 5.1). However, if peptides 3, 17, or 20 contain an oxidized Cys residue(s), peptides 4, 18, or 21 could not be formed from carboxyamidation of CML24.

To conduct this analysis, I denatured CML24 protein and then incubated the protein in either the presence or absence of reducing agent. The protein samples were then IAM treated and subsequently digested with trypsin. In addition, to assess CML24 folding stability, protein aliquots were mixed with either Ca^{2+} or EDTA. After treatments, proteins were re-purified and analyzed by mass spectroscopy (Figure 5.5).

In the MALDI-TOF spectra, I was able to identify ~90% of the predicted CML24 peptides (Table 5.1) using the Mascot database (Perkins et al., 1999). Peptide 3 (S_{10}CLGSMDDIKK$_{20}$) that contains Cys11 was not detected at 1196 Da in any of the treatments (Figure 5.5a, left panel). Only the samples that were reduced with DTT and carboxyamidated with IAM had the predicted +58 Da peptide at 1254 m/z (peptide 4) (Figure 5.5a, right panel, blue and green traces). These results indicate the Cys11 thiol group was unavailable for carboxyamidation prior to DTT-reduction and therefore may be in an oxidized form. I interpret this result as indicating that the cysteine thiol in peptide 3 is oxidized and linked to other peptides; however, I was not able to identify a potential linkage peptide in 700 to 3500 m/z region. It may be that this linkage is nonspecific.

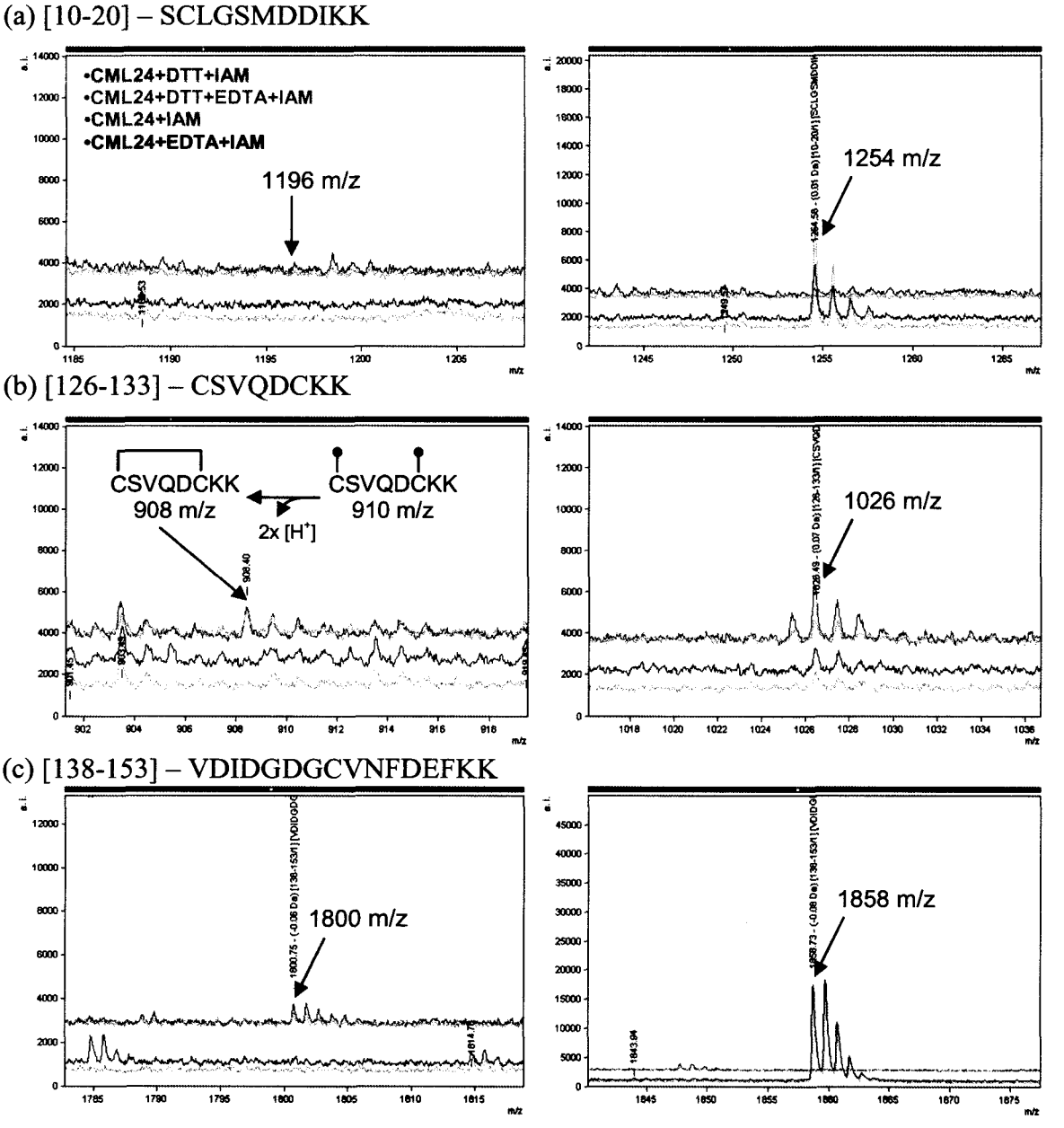

Fig 5.5 MALDI-TOF-MS analysis of trypsin-digested CML24 protein.
Recombinant CML24 protein was incubated with (blue and green traces) or without (orange and purple traces) DTT at 95°C for 10 min and 100mM IAM for 30min. Proteins were desalting and trypsin digested overnight with (green and purple traces) or without EDTA (blue and orange traces) and analyzed with MALDI-TOF-MS (Autoflex II). (a) Monoisotopic mass of peptide 10-20 did not appear at expecting 1196 m/z (left panel) instead at 1254 m/z (right panel) without reduction (orange and purple traces). (b) Monoisotopic mass of peptide 126-133, contains two Cys residues, without reduction appeared at 908 m/z instead of 910 m/z, which may correlate to two protons mass (left panel). Peptide 126-133 can be carboxylamidation with IAM in the presence or absence of DTT and appeared at 1026 m/z (right panel). (c) Monoisotopic mass of peptide 138-153 appeared at predicting 1800 m/z and 1858 m/z, after carboxylamidation. Intensity on the y-axis, mass-to-charge (m/z) on the x-axis.

The second and third cysteines, Cys126 and Cys131 are in the same peptide (C_{126}SVQDCKK_{133}) after trypsin digestion (Figure 5.5b). The non-reduced CML24 protein samples (Figure 5.5b, left panel, orange and purple traces) lacked the expected monoisotopic mass at 910 Da. Instead, there was a monoisotopic mass peak at 908 Da. This peptide would be predicted if Cys126 and Cys131 were disulfide bonded, losing two proton (H^+) mass units. After DTT reduction and IAM carboxyamidation, I identified the modified peptide (C_{126}SVQDCKK_{133}) at the expected mass of 1026 Da, consistent with a two-IAM modification shift from 910 Da (Figure 5.5b, right panel, blue and green traces). However, this peptide with two carboxyamidated modifications also appeared in non-reduced CML24 (Figure 5.5b, right panel, orange and purple traces). These results suggest that the CML24 protein existed in two forms. One fraction of CML24 had two free thiols within the 126-133 peptide; the other fraction harbored the two Cys as disulfide bond. This result may suggest flexibility of disulfide bond formation.

The fourth cysteine, Cys145, was identified in peptide 138-153 (V_{138}DIDGDGC*VNFDEFKK_{153}) and was detected at 1858 Da (Figure 5.5c, right panel, blue and green traces) with DTT reduction and IAM modification. However, in the absence of DTT, this peptide was unable to be modified by IAM and appeared at 1800 Da (Figure 5.5c, left panel, orange and purple traces). It is unlikely this cysteine is oxidized, which would also change the peptide mass. One possibility is that this cysteine thiol group was unable to be carboxyamidated because the peptide existed as a compact and stable folded structure. In the presence of reducing agent, this cysteine is accessible to carboxyamidation. These results suggest that Cys145 in CML24 is unlikely to be part of a disulfide bond.

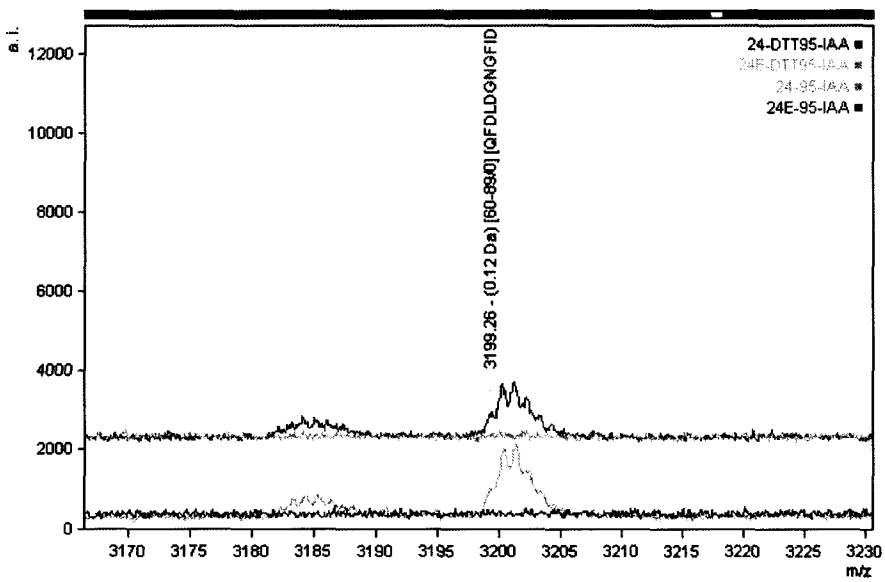

Fig 5.6 MALDI-TOF-MS analysis of trypsin-digested CML24 protein.
Recombinant CML24 protein was incubated with (blue and green traces) or without (orange and purple traces) DTT at 95°C for 10 min and 100mM IAM for 30 min. Proteins were desalted and trypsin digested overnight with (green and purple traces) or without EDTA (blue and orange traces) and analyzed with MALDI-TOF-MS (Autoflex II). Peptide 60-89 appears at 3199 m/z in the absence of Ca^{2+} (green and purple traces). Intensity on the y-axis, mass-to-charge (m/z) on the x-axis.

In summary, these data suggest that Cys126 and Cys131 may form a disulfide bond and Cys11 may be in an oxidized form, which potentially could also form intermolecular disulfide bonds. Cys145 does not appear in oxidized form and is unlikely to be part of a disulfide bond.

Removing Ca^{2+} with EDTA did not affect the thiol group modifications; this can be seen by comparing the blue and green traces or the orange and purple traces (Figure 5.5a, 5.5b, and 5.5c). However, one peptide that is significantly affected by EDTA is peptide 60-89 (QFDLDGNGFIDLDEFVALFQIGIGGGGNNR), which contains the second EF hand (underlined) (Figure 5.4 and 5.6). This peptide only appeared in the CML24 protein samples treated with EDTA. The absence of the peptide from the Ca^{2+}-treated protein may by the consequence of incomplete trypsin digestion (Figure 5.6). This result suggests that the presence of Ca^{2+} affects CML24 structure, in particular that of the second EF hand, such that the protein has higher resistance to denaturants and/or the trypsin protease.

Cysteine residues can participate in both intra- or inter- molecular interactions. To address whether CML24 can form multimers through cysteine oxidation, I incubated wild-type CML24 recombinant protein with 1 mM DTT in the presence or absence of Ca^{2+}. A single band is detected when CML24 is pretreated with reducing agent (Figure 5.7, lane 3 and 5), yet a small proportion of CML24 is detected as a slow migrating form in the absence of DTT (Figure 5.7, lane 2 and 4). The mobility of these forms relative to the protein mass standards (Figure 5.7, lane 1) indicates that CML24 can form dimers (~34 kDa) and timers (~51 kDa). These dimer and trimer structures were more stable in the presence of Ca^{2+} than EDTA (Figure 5.7, lane 2 and 4). These results suggest that

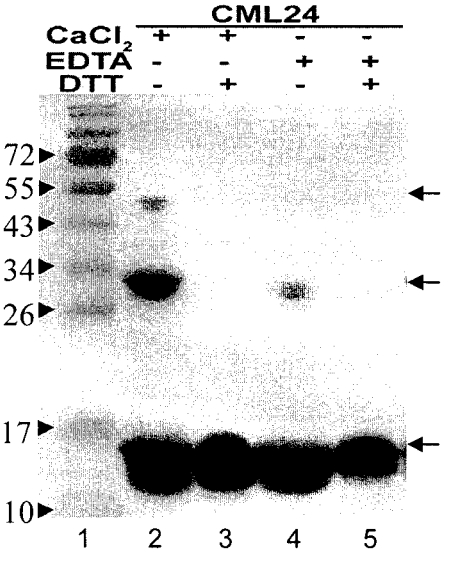

Fig 5.7 CML24 has potential to form multimers. 10 μg of wild-type CML24 recombinant protein was incubated in combinations of DTT, Ca^{2+}, and EDTA. Proteins were analyzed on 12% SDS-PAGE and stained with coomassie brilliant blue. Lane 1 shows the molecular mass markers. From bottom to top, arrows indicate the potential monomer (~16 kDa), dimer (~34 kDa), and trimer (~51 kDa) of CML24.

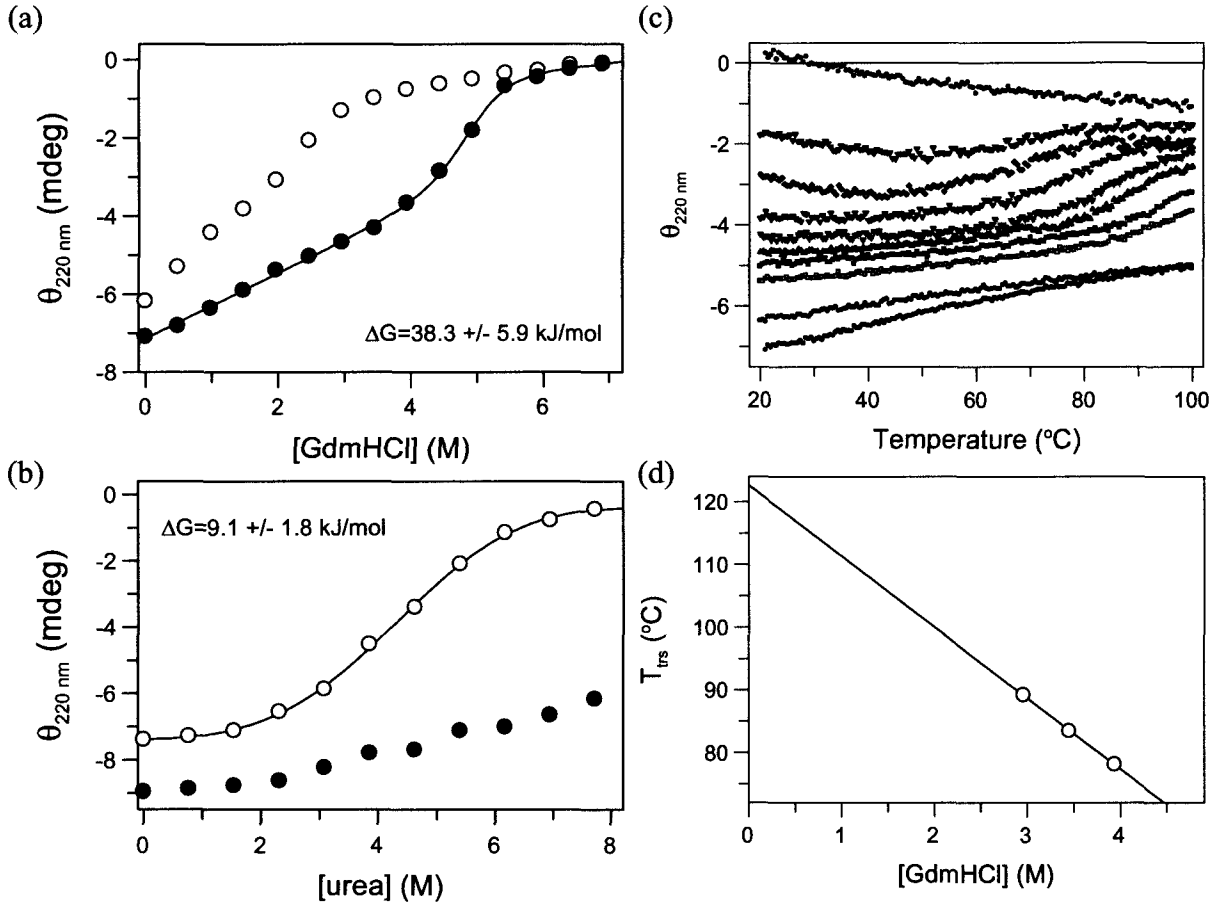

Fig 5.8 Unfolding of CML24 monitored by CD at 220nm. (a) GdmHCl-induced denaturation of apo-CML24 (open circles) and CML24-Ca^{2+} (solid circles) monitored by far-UV CD at 220 nm. (b) Urea-induced denaturation of apo-CML24 (open circles) and CML24-Ca^{2+} (solid circles) monitored by far-UV CD at 220nm. (c) Thermal denaturation of CML24 monitored by CD at 220 nm at different concentration of GdmHCl: from bottom 0.00, 0.99, 1.97, 2.46, 2.96, 3.45 (blue triangles), 3.94, 4.44, 4.93, and 6.90 M at 20 °C. (d) From extrapolation of T_m vs. [GdmHCl] to 0 M denaturant, the transition temperature of CML24 in the presence of 4 Ca^{2+} is 122.6 ± 1.0 °C (Performed by Pernilla Wittung-Stafshede and Erik Sedlák).

intermolecular disulfide bonds may enable multimeriztion of CML24. Whether this mulimerization has physiological relevance and occurs in the presence of other proteins or only occurs with purified CML24 remains to be elucidated.

5.1.3 CML24 protein stability

To address how Ca^{2+} affects CML24 protein stability and may contribute to CML24 functions, circular dichroism (CD) measurements were performed in collaboration with Pernilla Wittung-Stafshede. CD spectroscopy can report protein secondary structure. GdmHCl- and urea-induced unfolding of wild-type CML24 with or without Ca^{2+} were monitored using far-UV CD at 20°C (Figure 5.8a and 5.8b). In the presence of Ca^{2+}, CML24 is very stable and remains folded even at high concentrations of urea (Figure 5.8b) and unfolds only in GdmHCl concentrations higher than 5M (Figure 5.8a). In addition, thermal denaturation of CML24 with Ca^{2+} was also monitored with far-UV CD at a rate of 1.5°C/min (Figure 5.8c). CML24 was incubated with different concentration of GdmHCl (0.00, 0.99, 1.97, 2.46, 2.96, 3.45, 3.94, 4.44, 4.93, and 6.90 M) and CD thermal-unfolding was monitored at 20°C to 100°C. The values of T_m at 3.45, 3.94, and 4.44 M GdmHCl were used for extrapolation of T_m versus [GdmHCl] to 0 M denaturant (Figure 5.8d). Interestingly, the transition temperature of CML24 in the presence of 4 Ca^{2+} bound is 122.6 ± 1.0 °C, which suggests CML24-$[Ca^{2+}]_4$ is very stable in the presence Ca^{2+}.

5.2 CML24-ATG4 interactions

To begin to elucidate the biochemical basis for the *cml24* mutant phenotypes, we sought to identify CML24 interacting proteins.

5.2.1 ATG4b identified as a CML24 interaction partner in yeast two hybrid screen

Our first approach to identify CML24-interacting proteins was to conduct a two-hybrid screen for genes encoding proteins that bind CML24 in yeast. Using the University of Wisconsin Y2H service, 18 million clones were tested for CML24 interaction by selection for yeast growth on histidine drop-out plates and screens for beta-galactosidase activity. Plasmids from the positive clones were rescued and analyzed by restriction enzyme digestion. Verification of interaction by the positive clones was achieved by retransformation. Transformant growth occurred in the selection media when cotransformed with CML24 as bait; no growth occurred with non-bait constructs. In addition, β-galactosidase activity was detected only when CML24 was used as bait. The identities of the positive clone genes were determined by sequencing. The autophagy cysteine protease, ATG4b (At3g59950), was identified as an interactor.

5.2.2 CML24 is pulled down with GST-ATG4b

To verify that CML24 can interact with ATG4b, I tested for co-association with the glutathione-S-transferase (GST) pull-down assay. The coding sequence of *ATG4b* was cloned into pGEX2T vector and fused to GST at its amino-terminus. GST-ATG4b protein was produced in *E. coli* BL21 cells and purified with glutathione (GSH)-sepharose^{TM} 4B (Figure 5.9). The size of GST-ATG4b fusion protein is 78.5 kDa, and GST protein is around 26 kDa (Figure 5.9).

CML24 is pulled down with the GSH-beads in the presence of GST-ATG4b (Figure 5.10, lanes 1 and 2 "Pull down") but not with GST alone (Figure 5.10, lanes 9 and 10 "Pull down"), indicating that the GST-ATG4b interaction with CML24 is

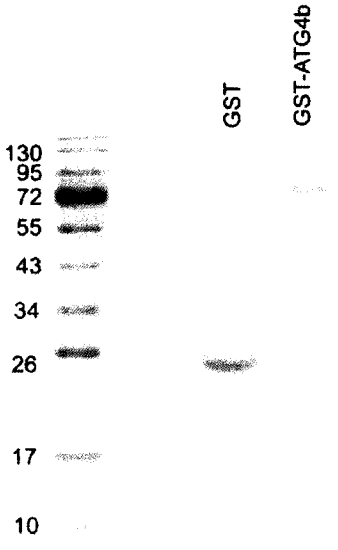

Fig 5.9 Purified GST and GST-ATG4b protein. GST and GST-ATG4b fusion protein were eluted from GSH-sepharose 4B with 5 mM reduced glutathione. The purified proteins were detected on a Coomassie Blue-stained SDS-PAGE.

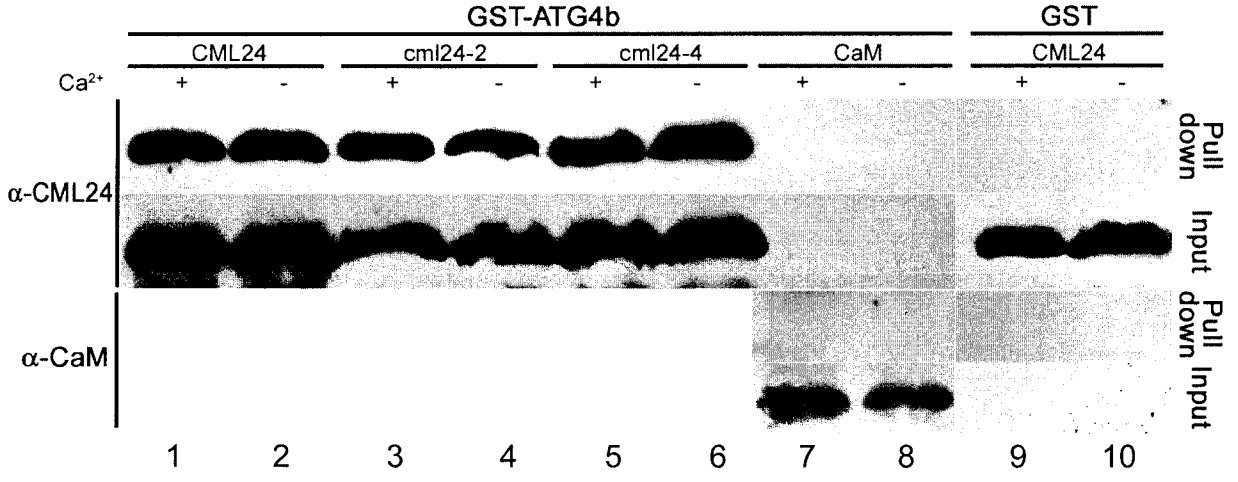

Fig 5.10 CML24 binds GST-ATG4b *in vitro* independent of calcium. Recombinant GST-ATG4b or GST was used in pull-down assays with CML24, cml24-2, cml24-4, and CaM in the presence (+) or absence (-) Ca^{2+}. Protein precipitated with the GSH-sepharose ("Pull down") and protein remaining soluble ("Input") were separated on 12% SDS-PAGE and immunoblotted with anti-CML24 or anti-CaM antibody.

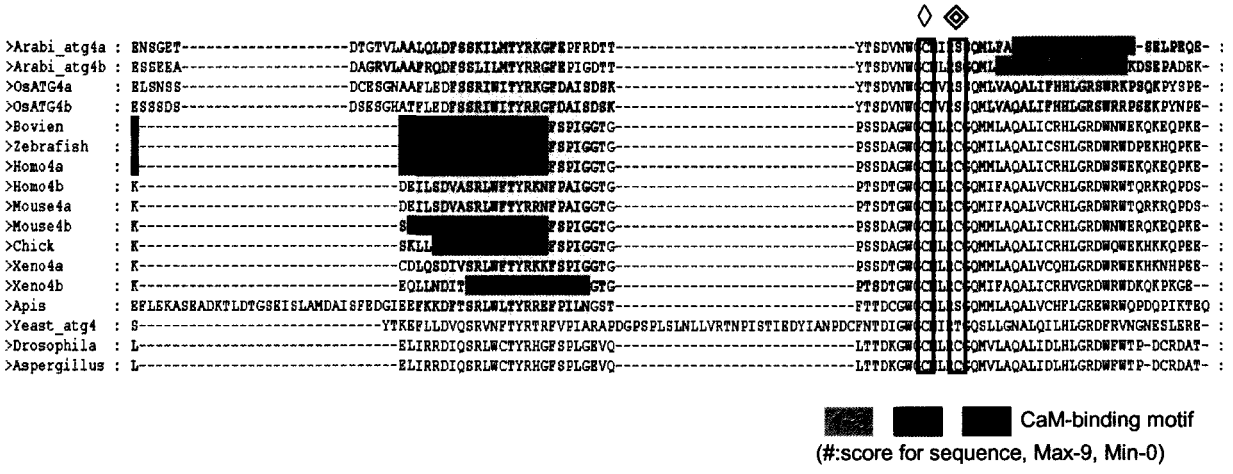

Fig 5.11 Plant ATG4 proteins lack the analogous oxidation-sensitive Cys78 of human ATG4 and have an additional CaM-binding motif. Amino-acid alignment of the region surrounding the active site Cys residue among members of the ATG4 family. The alignment was preformed using the ClustalX multiple alignment program and the green/blue coloration marks the presence of predicted CaM-binding motifs. Red boxes indicate two conserved Cys residues. ◊ marks the catalytic Cys residue. ◈ marks Cys78 that is essential for redox regulation of human ATG4 but is missing in plant ATG4.

dependent upon the presence of ATG4b. The presence of Ca^{2+} had no detectable effect on CML24 binding to GST-ATG4b binding (Figure 5.10, compare lanes 1 and 2 "Pull down").

Based on the Calmodulin Target Database (http://calcium.uhnres.utoronto.ca/ctdb/ctdb/home.html) predictions performed on Arabidopsis ATG4b, I found that ATG4b contains a predicted CaM-binding domain near the active site (Figure 5.11). A predicted CaM-binding domain is not present in animal ATG4s (Figure 5.11). The predicted CaM-binding region on Arabidopsis ATG4b is consistent with three distinct types of CaM-binding motifs, 1-10 (F_{181}xxxxxxxxL_{190}), 1-5-10 (L_{180}xxxxL_{185}xxxxL_{190}), and 1-14 (F_{181}xxxxxxxxxxxxW_{194}). 1-10 and 1-5-10 motifs are similar to Ca^{2+}/calmodulin dependent kinase II binding manners (Rhoads and Friedberg, 1997). Smooth muscle and skeletal muscle myosin light chain kinase has a similar 1-14 motif in the binding region (Rhoads and Friedberg, 1997). These results suggest the possibility that CML24 may possibly interact with ATG4b through a predicted CaM-binding domain.

5.2.2 Mutated cml24 proteins interact with GST-ATG4b

If the cellular functions of CML24 are mediated through interaction of CML24 with ATG4b, one prediction would be that the *cml24-2* and *cml24-4* mutant phenotypes occur because the amino acid substitutions in the cml24-2 and cml24-4 proteins affect ATG4b interaction.

To test this possibility, I assayed cml24-2 and cml24-4 interaction with GST-ATG4b. In the presence of GST-ATG4b, both cml24-2 and cml24-4 were pulled down with GSH-beads (Figure 5.10, lanes 3 to 6 "Pull down"). Similarly to wild-type CML24,

the mutant cml24 interactions with GST-ATG4b were unaffected by the presence of Ca^{2+}. These results indicate that the mutant isoforms cml24-2 and cml24-4 retain Ca^{2+}-independent ATG4b binding ability that is indistinguishable from wild type CML24, at least under the *in vitro* conditions tested. Thus, differential CML24 binding of ATG4b may not explain the phenotypic consequences of cml24-2 and cml24-4.

5.2.3 CaM does not bind ATG4b-GST

CML24 is highly similar to CaM, the prototypical eukaryotic Ca^{2+} sensor, in primary sequence (Figure 1.1) and predicted tertiary structure (Figure 5.4) (Khan et al., 1997). To test whether GST-ATG4b can also bind CaM, I conducted a similar binding assay with purified bovine CaM (Sigma P1431). Under conditions in which GST-ATG4b interacts with CML24, no binding to CaM is detected (Figure 5.10, lane 7 and 8). CaM also did not interact with GST alone (Figure 5.10, lane 7 to 10). Thus, despite the primary and predicted tertiary structural similarities between CML24 and CaM, the interaction with GST-ATG4b may be specific for CML24.

5.2.4 Evolutionary trace analysis of ATG4b

In collaboration with Olivier Lichtarge and Angela Wilkins (BCM), Arabidopsis ATG4b amino acid sequence was examined for clustered amino acids with high conservation among homologs. Unlike traditional mutational analysis which tests functional relevance of each amino acid one residue at a time, evolutionary trace (ET) is based on phylogenetic relationships and identifies 3-dimensionally clustered amino acid residues predicted to be functionally important (Madabushi et al., 2002). ET analysis of Arabidopsis ATG4 indentified the well-characterized binding site for ATG8 (Figure

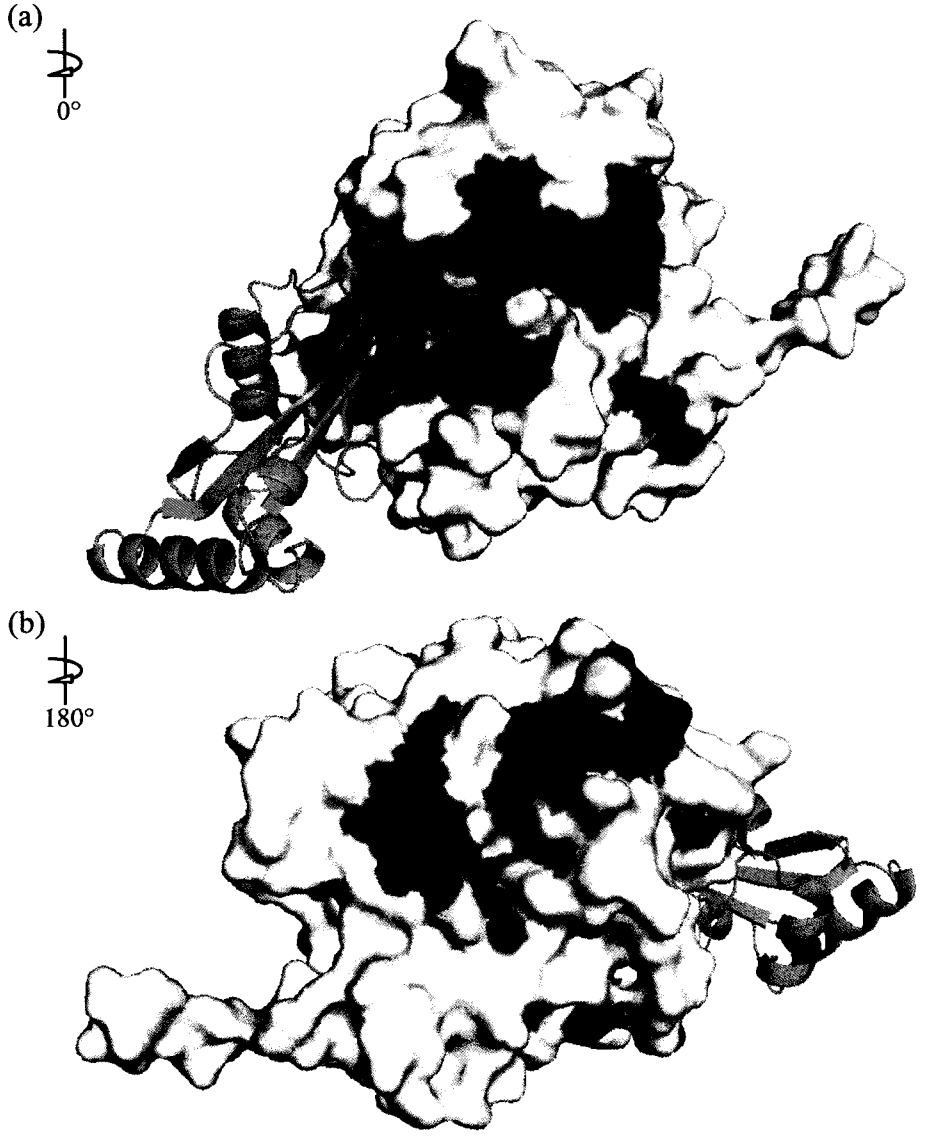

Fig 5.12 Evolutionary trace analysis of plant ATG4b. (a) and (b) are HsATG4b and LC3 (human ATG8) structure (PDB_2Z0E) rotated by 180° about the y-axis. HsATG4b and LC3 are shown in space-filling and cyan-ribbon structures, respectively. The ET-identified residues are marked top 25% (a) and 35% (b) residues on HsATG4b. (a) Red residues represent top 25% residues identified with ET analysis from mammal sequences. (b) Top 35% residues identified with ET analysis and red and blue marked residues are animal and plant specific, respectively.

5.12a). In addition ET highlighted another potential functional site on ATG4b (Figure 5.12b); remarkably, this region is close to the predicted CaM-binding site (Figure 5.11). This second site identified is specific for plant ATG4 (Figure 5.12b). However, animal ATG4s also have a second site identified by ET that may have functional relevance (data not shown). This result suggests that there is a second functional site close to the predicted CaM-binding motif on plant ATG4s and this may involve in regulation of ATG4b.

5.3 Conclusion

In this chapter, I analyzed biochemical characteristics of CML24 to assist in understanding the potential functions of CML24 in plants. CML24 changes conformation upon Ca^{2+} binding. Recombinant cml24-2 may have altered Ca^{2+} binding affinity relative to wild type CML24. Ca^{2+} binding is important for CML24 structured stability and may influence the multimerization of CML24. Cys11, Cys126 and Cys131 of CML24 may form disulfide bonds, as revealed by mass spectroscopy.

I also identified a potential interacting partner of CML24, ATG4b. ATG4b and CML24 interact in yeast two-hybrid and ATG4b-GST pull down assays. The interaction between CML24 and ATG4b is independent of Ca^{2+} binding and is maintained with the cml24-2 and cml24-4 point mutants.

Overall, the results described in this chapter suggest that CML24 has characteristics of both a Ca^{2+} sensor and redox sensor. To further investigate the subtle Ca^{2+}-binding affinity different in CML24 and cml24-2, the Ca^{2+}-binding kinetics will be determined with incorporating $^{45}Ca^{2+}$ by CML24 and cml24-2. To determine specificity of CML24 and ATG4b interaction, ATG4b-paralog, ATG4a, will also be evaluated the

interaction with CML24. Amino acid substitutions of the potential CaM-binding domain on ATG4b will be generated and tested the interaction with CML24. The crystal and/or NMR structure of CML24 will reveal the conformational consequence of a disulfide bond and Ca^{2+}-binding. Recombinant cml24 protein with four cysteine substitutions with alanine will be generated to analyze the physiological relevance of potential disulfide bond formation.

Chapter 6: CML24 and Autophagy Regulation

To begin to reveal mechanisms of CML24 function that may underlie the phenotypic changes detected in the *cml24* mutants (Chapter 3), I identified a CML24-interacting protein, ATG4b, by yeast two hybrid and GST pull-down assay (Chapter 5). I next wanted to determine whether the CML24 interaction with ATG4b affects ATG4 activity. Furthermore, I sought to address whether CML24 regulates autophagy through the interaction with ATG4.

To address these questions, I first analyzed CML24 effects on *in vitro* ATG4 activity that cleaves ATG8. In addition, I monitored autophagy in wild type, *cml*, and autophagy mutants by multiple methods. Finally, I compared dark- or nitrogen depleted-related root growth phenotypes among wild type, *cml* and autophagy mutants.

6.1 CML24 effects on ATG4b activity

6.1.1 CML24 effects on recombinant ATG4b activity *in vitro*

ATG4 cleaves ATG8 to result in a Gly residue as its carboxyl terminus (Yoshimoto et al., 2004). To test whether the interaction between CML24 and ATG4b might affect ATG4b cysteine protease activity, I first designed a substrate to enable *in vitro* ATG4 activity assays. I generated an ATG8e fusion protein with a Hemagluttinin (HA) epitope and six histidine (His) residues at its carboxyl- and amino-termini, respectively. This recombinant His-ATG8e-HA protein was produced in *E. coli* BL21 and affinity purified with Ni-NTA agarose (Figure 6.1).

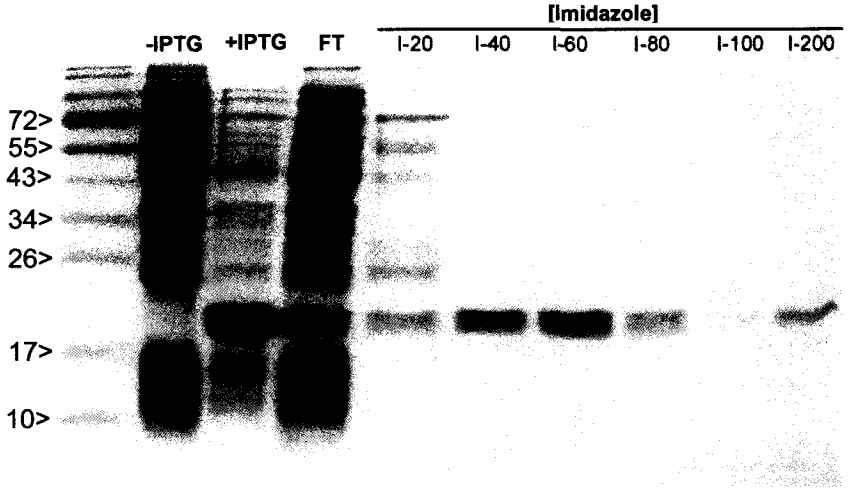

Fig 6.1 His-ATG8e-HA protein purification. Expression and purification of His-ATG8e-HA fusion protein from *E. coli* BL21 (DE3). –IPTG, crude extract of *E. coli*; +IPTG, crude extract of *E. coli* in the presence of IPTG; FT, flow through fraction from Ni-NTA column; I-20 to I-200, eluates with 20 to 200 mM imidazole from Ni-NTA column. Molecular mass markers are indicated at left. Proteins were detected on a Coomassie Blue-stained SDS-PAGE.

To test whether the recombinant GST-ATG4b has activity, I incubated His-ATG8e-HA with or without GST-ATG4b at 20°C for two hours, ran the proteins through SDS-PAGE, and detected protein by western blot analysis with either anti-His or anti-HA antibodies (Figure 6.2). After two hours incubation without ATG4b, a single band is detected by either anti-HA or anti-His antibody (Figure 6.2). A lower band generated in the presence of GST-ATG4b is recognized by anti-His antibodies but not by anti-HA antibodies (Figure 6.2), as expected for ATG4 cleavage of the carboxyl-terminal HA extension from ATG8e. These results indicate that recombinant GST-ATG4b is able to remove the carboxyl-terminal HA extension from His-ATG8e-HA.

In an attempt to improve GST-ATG4b enzymatic rate *in vitro*, I assessed the effect of different temperatures on cleavage of His-ATG8e-HA. Reactions were conducted at 10°C, 20°C, 30°C, 40°C, and 50°C for three hours. The coomassie brilliant blue gel staining of total proteins show that in the absence of GST-ATG4b, His-ATG8e-HA runs as a single stained band (Figure 6.3a, first lane). After a three-hour incubation with GST-ATG4b at 30°C, 10% of the intact His-ATG8e-HA remained (Figure 6.3a, second and third lanes; Figure 6.3b, gray bars). Less His-ATG8e-HA cleavage occurred at 10°C and 20°C (Figure 6.3a, 6.3b). At the higher temperatures of 40°C and 50°C, activity was greatly reduced (data not shown). No strong difference in band intensities occurred as a consequence of Ca^{2+} or EDTA presence (Figure 6.3a, second and third lanes); therefore it appears that Ca^{2+} does not affect GST-ATG4b *in vitro* activity under these assay conditions. These results suggest that the optimal temperature for GST-ATG4b activity is 30°C. However, as evidenced by an overall decrease in total protein band intensities this assay is potentially compromised by some nonspecific protease

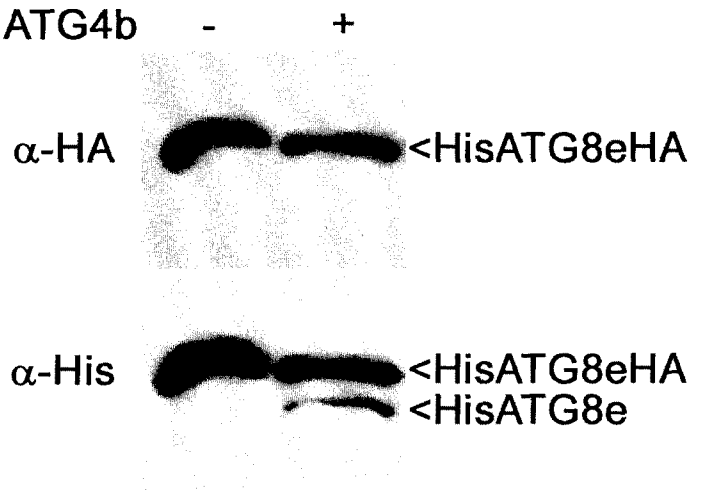

Fig 6.2 ATG4b activity *in vitro*. His-ATG8e-HA was incubated without (-) or with (+) ATG4b at 20°C for 2 hours. Reaction aliquots were separated on 15% SDS-PAGE and western blotting. The blot was probed with α-HA (top panel) first and α-His (bottom panel). The high and low molecular weight bands indicate full length His-ATG8e-HA and His-ATG8e, respectively.

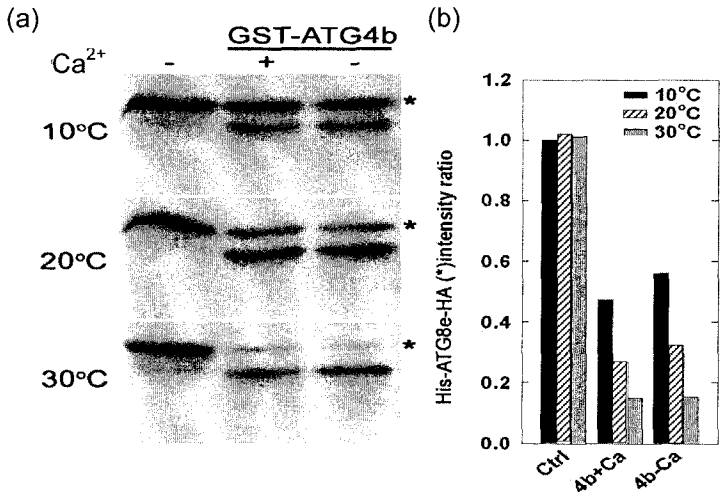

Fig 6.3 Effect of temperature on GST-ATG4b cysteine protease activity *in vitro*. (a) His-ATG8e-HA was incubated without or with GST-ATG4b at 10°C, 20°C, and 30°C for three hours in the presence of Ca^{2+} (+) or EDTA (-). Proteins were separated by SDS-PAGE and visualized by coomassie brilliant blue staining. (b) The intensity was quantified with Image J (NIH) and full length His-ATG8e-HA (*) in the first lane of 10°C (a, without Ca^{2+} or GST-ATG4b) was defined as 1 for quantification. The experiment has been repeated three times with similar results.

activity leading to loss of total proteins especially at elevated temperature.

Next, I used this assay to assess whether the presence of CML24 alters ATG4 ability to cleave the carboxyl-terminal extension of His-ATG8e-HA. I incubated His-ATG8e-HA proteins with GST-ATG4b and CML24 in the presence of Ca^{2+} or EDTA at 30° (Figure 6.4). After two hours of incubation in the absence of CML24 protein, approximately 70% of the full-length His-ATG8e-HA protein remained (Figure 6.4a, and 6.4b), and the lower molecular weight form appeared (Figure 6.4a). Ca^{2+} and EDTA did not affect the activity of GST-ATG4b (Figure 6.4a, second and third lanes), which is consistent with the results in Figure 6.3. In the presence of CML24 (Figure 6.4a, bottom bands in fourth and fifth lanes), a comparable level (~70%) of full-length His-ATG8e-HA protein remained (Figure 6.4a and 6.4b, fourth and fifth lanes) relative to the absence of CML24 after two hours incubation (Figure 6.4a and 6.4b, second and third lanes). These results suggest that CML24 did not affect GST-ATG4b *in vitro* activity to cleavage His-ATG8e-HA after 2 hours incubation.

In addition, I prolonged the GST-ATG4b *in vitro* activity assay reactions to 6 hours to test whether CML24 has subtle effects on GST-ATG4b activity. After 6 hours incubation with GST-ATG4b in the absence of CML24 protein, about 60% of the full-length His-ATG8e-HA remained (Figure 6.4c, d). The band intensity of the cleaved His-ATG8e is greater than the full-length substrate remaining (Figure 6.4c, second and third lanes). Therefore, the overall activity of GST-ATG4b is low under these conditions, unable to convert all the substrate to product in 6 hours. Furthermore, there is some nonspecific protease activity leading to the loss of full length His-ATG8e-HA and appearance of additional smaller bands after the 6-hour incubation. Interestingly, in the

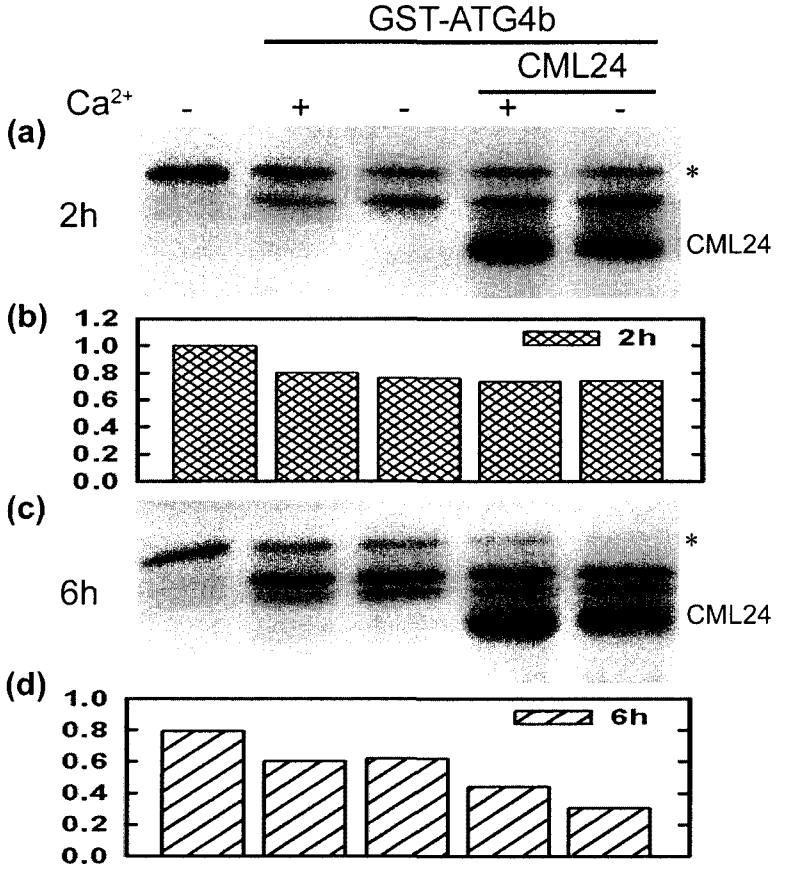

Fig 6.4 Addition of CML24 to test effects on ATG4b *in vitro* cleavage of His-ATG8e-HA substrate. (a) (c) His-ATG8e-HA was incubated without or with GST-ATG4b and with CML24 in the presence of Ca^{2+} (+) or EDTA (-) for 2 or 6 hrs at 30°C. Proteins were separated by SDS-PAGE and visualized by coomassie brilliant blue staining. (b) (d) The intensity was quantified with Image J (NIH), and full length His-ATG8e-HA (*) in the first lanes of 2h (a, without Ca^{2+}, CML24, or GST-ATG4b) was defined as 1 for quantification. The experiment has been repeated three times with similar results.

presence of CML24, GST-ATG4b may have somewhat higher activity to cleave His-ATG8e-HA as compared to activity in the absence of CML24. However, the least amount of full length substrate remaining occurs with CML24 and in the presence of Ca^{2+} and even higher activity in the presence EDTA (Figure 6.4c, fourth and fifth lanes). Future experiments will be aimed at reducing the background protease effects to verify that the loss of substrate is due to ATG4 and not nonspecific protease activity. However, this experiment suggests that CML24 may have a weak enhancing effect on GST-ATG4b *in vitro* cleavage of His-ATG8e-HA. Apo-CML24 may have the strongest enhancement of GST-ATG4b activity.

To verify that the lower band seen by coomassie brilliant blue staining is the result of the removal of the carboxyl-terminus of His-ATG8e-HA, I repeated the *in vitro* GST-ATG4b activity assay and detected resulting protein products with the anti-HA antibody (Figure 6.5). After six hours of incubation at 30°C, only one band approximately of 18 kDa, consistent with His-ATG8e-HA migration, was recognized by anti-HA antibody in all five lanes. Therefore the lower coomassie brilliant blue stained band in Figure 6.4 lacks the HA epitope. Consistent with the results of Figure 6.4, co-incubation with GST-ATG4b results in a moderate decrease in the anti-HA recognized protein, with no significant difference in the presence of Ca^{2+} or EDTA (Figure 6.4, second and third lanes). In the presence of CML24, His-ATG8e-HA decreased in quantity, with the greatest protein loss occurring in the presence of EDTA. Overall, these results are consistent with the coomassie brilliant blue staining results (Figure 6.4).

Fig 6.5 CML24 may enhance GST-ATG4b activity. Cleavage of His-ATG8e-HA substrate. His-ATG8e-HA was incubated without (first lane only) or with GST-ATG4b and with CML24 in the presence of Ca^{2+} (+) or EDTA (-) for 6 hrs at 30°C. Reactions were separated on 15% SDS-PAGE and followed by anti-HA western blot analysis. The experiment has been repeated three times with similar results.

Together the data presented in Figures 6.4 and 6.5 suggest that CML24 may enhance ATG4 cleavage of the carboxyl-terminus of His-ATG8e-HA, and apo-CML24 may have the greatest enhancement activity.

6.1.2 *cml24* mutant tissue extracts have altered His-ATG8e-HA activity

Although I can detect ATG4b enzymatic activity by the appearance of a carboxyl-terminal HA cleavage from His-ATG8-HA substrate *in vitro*, the activity level appears to be low, with only 30% cleavage after two hours. This slow cleavage rate suggests the possibility that the recombinant GST-ATG4b protein may not be fully active. Alternatively, additional cellular factors and/or post-translational modifications not present in the bacterially produced proteins are required for full ATG4b activity. Therefore I sought to assay ATG4b activity using crude tissue lysates.

In the presence of exogenously added His-ATG8e-HA, extract ATG4 activity is predicted to generate a lower molecular mass protein recognized by the anti-His antibody by western blot analysis. Indeed, crude extracts from wild-type plants produce a lower molecular mass form of an anti-His antibody recognized protein (Figure 6.6a, "Col-0"). This lower band is likely produced by endogenous ATG4 activity because extracts derived from an *atg4a4b* double mutant fail to generate this product (Figure 6.6a, "*atg4a4b*").

Plants were harvested twice at different photoperiod points, during the light period (Figure 6.6a) and one hour after the light was turned off (Figure 6.6b). I reasoned that darkness may trigger autophagy and therefore ATG4 activity regulation may occur. In addition, based on microarray data, *ATG4b* expression is regulated by light/dark cycles (Michael et al., 2008). Under long day growth conditions, ATG4b transcripts accumulate

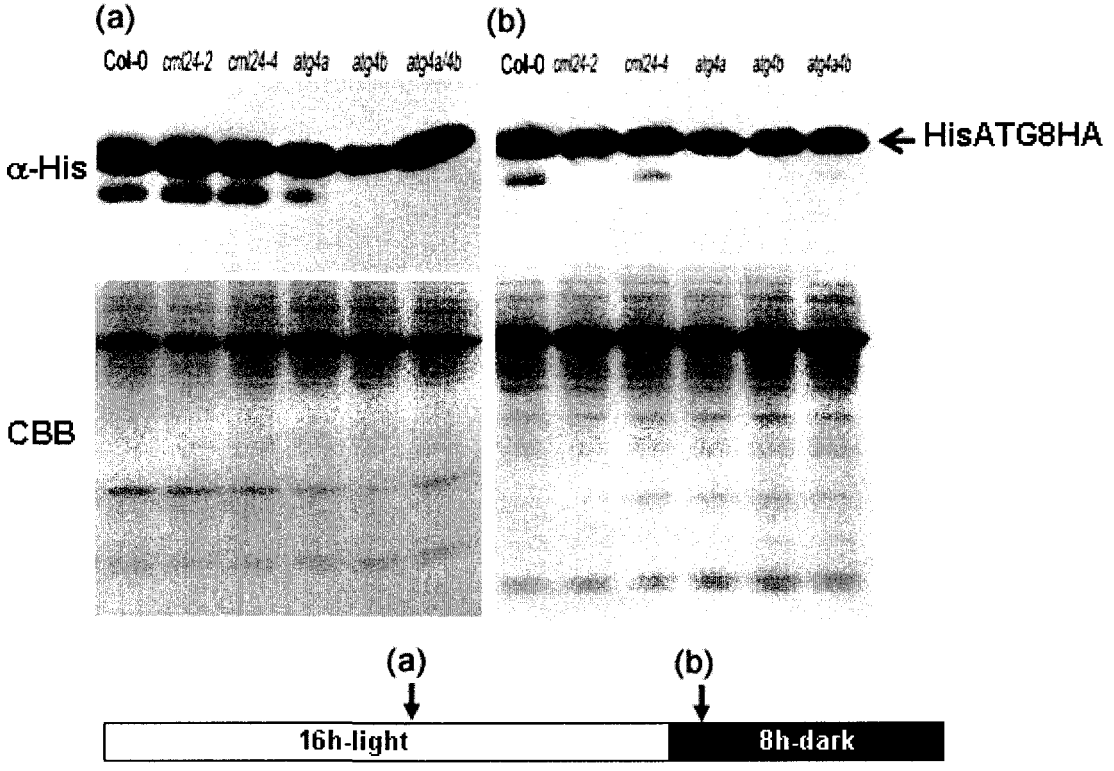

Fig 6.6 *cml24* mutant extracts may have altered ATG4 activity assayed as His-ATG8-HA cleavage *in vitro*. Wild type (Col-0), *cml24-2*, *cml24-4*, *atg4a*, *atg4b*, and *atg4a4b* plants were harvested in the middle of a 16-h light period (a) or one hour after the shift to darkness (b). The scheme at the bottom indicates the sample collection times. Crude tissue extracts were incubated with His-ATG8e-HA at 30°C for 2 hours. The reactions were separated on 15% SDS-PAGE and immunoblotted with α-His antibody. Total proteins were stained with coomassie brilliant blue (CBB) in the gel after transfer to verify similar protein amounts loaded in all lanes. The experiment has been repeated twice with similar results.

after a shift from darkness to light and are reduced after onset of darkness (Michael et al., 2008). Thus, one prediction is that ATG4b would be more abundant and display higher activity in plant tissues harvested in the light than those harvested in the dark.

Extracts prepared from wild type (Col-0) harvested during the light period (Figure 6.6a, "Col-0") and one hour after the light was turned off (Figure 6.6b, "Col-0") demonstrated ability to convert the His-ATG8e-HA substrate to a lower molecular mass protein. The light period-collected extracts revealed higher amounts of lower molecular mass protein than the dark period-collected extracts. These results suggest that Col-0 tissues have higher ATG4 activity during the light relative to the dark period.

To determine whether CML24 can affect endogenous ATG4 activity, I compared the His-ATG8e-HA cleavage activities in wild-type extracts (Col-0) to extracts isolated from the *cml24-2* and *cml24-4* mutants.

Extracts prepared from light or dark collected *cml24-2* and *cml24-4* tissues were incubated with His-ATG8e-HA and production of the smaller protein band was assessed by anti-His westerns. Tissue extracts prepared from light period-harvested *cml24-2* and *cml24-4* demonstrated comparable production of the His-ATG8e-HA cleavage product as wild type (Figure 6.6a, "*cml24-2*" and "*cml24-4*"). I interpret this result to indicate that ATG4 activity levels are comparable in the *cml24* mutants relative to wild type. However, the low molecular mass proteins were undetectable in the dark-collected *cml24-2* tissue extract (Figure 6.6b, "*cml24-2*"). Production of the anti-His detected-low molecular mass protein was also decreased in the dark-collected *cml24-4* extract relative to the wild type extract. Reduced cleavage product suggests that the *cml24* mutants have a diminished ATG4 activity at least under certain growth conditions.

ATG4 is encoded by *ATG4a* and *ATG4b* in Arabidopsis, and *ATG4b* is reported to contribute approximately 70% of total ATG4 activity (Thompson et al., 2005). To determine whether *atg4a* and *atg4b* mutants have ATG4 activity deficiencies, I also analyzed endogenous *atg4a* and *atg4b* activities on His-ATG8e-HA substrate (Figure 6.6a, "*atg4a*" and "*atg4b*"). Only the extract prepared from light period-collected *atg4a* had detectable anti-His detected cleavage product (Figure 6.6a, "*atg4a*"). *atg4b* and dark-collected *atg4a* had no detectable activity (Figure 6.6a,b, "*atg4b*"; 6.6b, "*atg4a*"). These results indicate *atg4a* and *atg4b* have reduced cleavage on activity on the His-ATG8e-HA substrate consistent with the expected reduction in ATG4 activity. In addition, these results are consistent with the interpretation that this assay measures ATG4 activity.

Overall, these results suggest that ATG4b activity regulation by darkness may be defective in *cml24-2* and *cml24-4*; therefore, CML24 may be necessary for proper ATG4 activity regulation in response to darkness. This effect of CML24 on ATG4 activity may be direct, in that CML24 may enhance recombinant GST-ATG4b activity *in vitro*.

6.2 Monitoring autophagy in *cml24* mutants with fluorescence imaging

To investigate whether *cml24* mutants may have altered autophagy, I used the autophagy marker monodansylcadaverine (MDC) and a green fluorescent protein (GFP)-tagged an autophagy protein, ATG8e, to monitor appearance of autophagosome-like structures. MDC is thought to stain acidic compartments, with selectivity toward mature autophagosomes; GFP-ATG8 likely reports fluorescence regardless of protein localization. In brief, I find differences between the *cml24* mutants and Col-0 in staining patterns. However, clear interpretation of potential defects will require additional experiments.

6.2.1 The *cml24* mutants have altered monodansylcadaverine fluorescence

The finding that CML24 can bind with ATG4b and may affect ATG4b activity in plant extracts led me to test whether the *cml24* mutant plants may be defective in autophagosome formation. I used monodansylcadaverine (MDC) as a cellular fluorescence indicator that stains acidic lipid-bound compartments (pKa 4.5~5.0) (Biederbick et al., 1995; Contento et al., 2005).

Autophagy can be induced by nitrogen depletion in plants (Rose et al., 2006). Therefore, I tested whether MDC fluorescence increased in roots exposed to growth media lacking nitrogen. Plants were grown on nutrient rich media for one week and transferred to either nitrogen-free or full nutrient liquid media for an additional 5 days. Under rich media (PNS), wild type (Col-0) showed low MDC fluorescence levels (Figure 6.7). This basal MDC fluorescence in Col-0 could result from acidic compartment staining unrelated to autophagosomes. Alternatively, the MDC fluorescence could be reporting a basal level of constitutive autophagy that has been reported for Arabidopsis roots (Inoue et al., 2006; Yano et al., 2007). After growth in the absence of nitrogen for 5 days, wild type MDC fluorescence increases (Figure 6.7, "Col-0", "PS"). This increased MDC staining may be due to increased autophagosome formation because the autophagy mutant, *atg7-1*, fails to show a comparable increase in MDC fluorescence after growth without nitrogen (Figure 6.7, "*atg7-1*", "PS"). ATG7 is an E1 ubiquitin-like protein required for ATG8 modification and autophagy progression (Figure 1.5) (Doelling et al., 2002). These data are consistent with the interpretation that 5 days of growth without nitrogen may induce starvation and increase autophagosome formation in

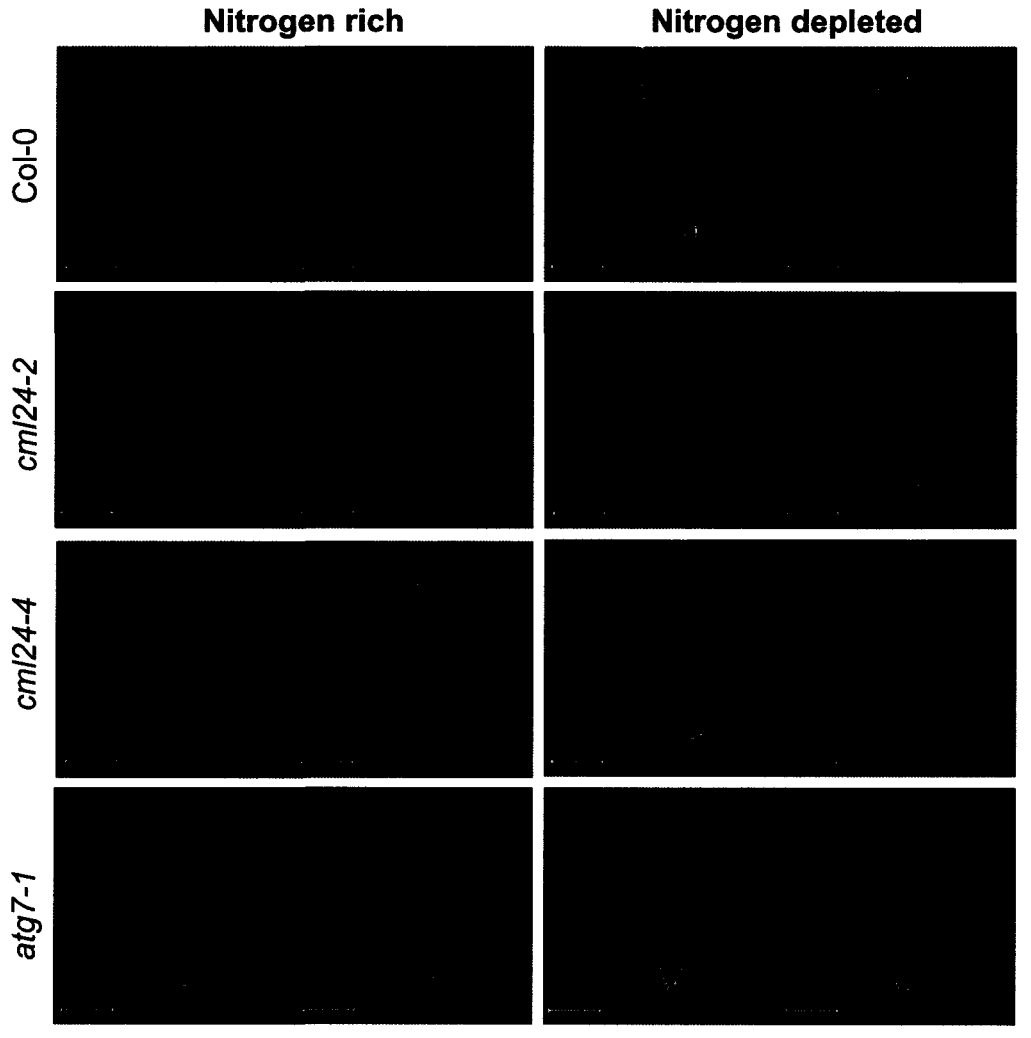

Fig 6.7 MDC staining of root tips of wild type (Col-0), *cml24-2*, *cml24-4*, and *atg7-1*. One-week-old plants were transferred to media with (Nitrogen rich) or without nitrogen (Nitrogen depleted) and grown in the light for 5 days. Roots were stained with MDC for 10 min and visualized by fluorescence microscopy. n=5. Representative examples are shown.

an *atg7-1*-dependent manner. Next, I compared the responses of *cml24-2* and *cml24-4* roots to similar treatment. *cml24-2* had variable MDC fluorescence on rich media (PNS) relative to wild type and comparable fluorescence to wild type after growth without nitrogen. *cml24-4* had elevated MDC fluorescence relative to wild type in both nitrogen-rich and nitrogen-depleted media. These results suggest that CML24 may affect autophagosome formation in roots. However, because non punctate MDC staining may occur independently of autophagosome formation and confuse interpretation, I needed to better define the MDC fluorescence images.

Therefore, I next examined MDC autophagosome labeling at the subcellular level. 10-day-old seedlings were transferred to PNS or PS plates for three days and stained with MDC. Because roots contain cells in different maturation stages, I examined both immature cells near the root tips and more mature cells located more proximally (Figure 6.8). Images were taken at 100x magnification to view subcellular fluorescence.

On complete media, wild type root tips have variable and some what blotchy MDC fluorescence (Figure 6.8a); this fluorescence is unlikely to be reporting autophagosomes because *atg7-1* shows similar fluorescence patterns (Figure 6.8m). However, in mature root cells, some punctate fluorescence was detected in Col-0 that was absent in *atg7-1* (Figure 6.8b and 6.8n). Therefore punctate MDC fluorescence in mature root cells may be a reliable marker for autophagosome accumulation.

The blotchy MDC fluorescence on root tips diminished in both Col-0 and *atg7-1* plants grown in media lacking nitrogen (Figure 6.8c, and 6.8o). Punctate fluorescence increases in Col-0 root tips from nitrogen-starved plants (Figure 6.8c); however *atg7-1* root tips also show some fluorescence particles, although perhaps fewer than Col-0, in

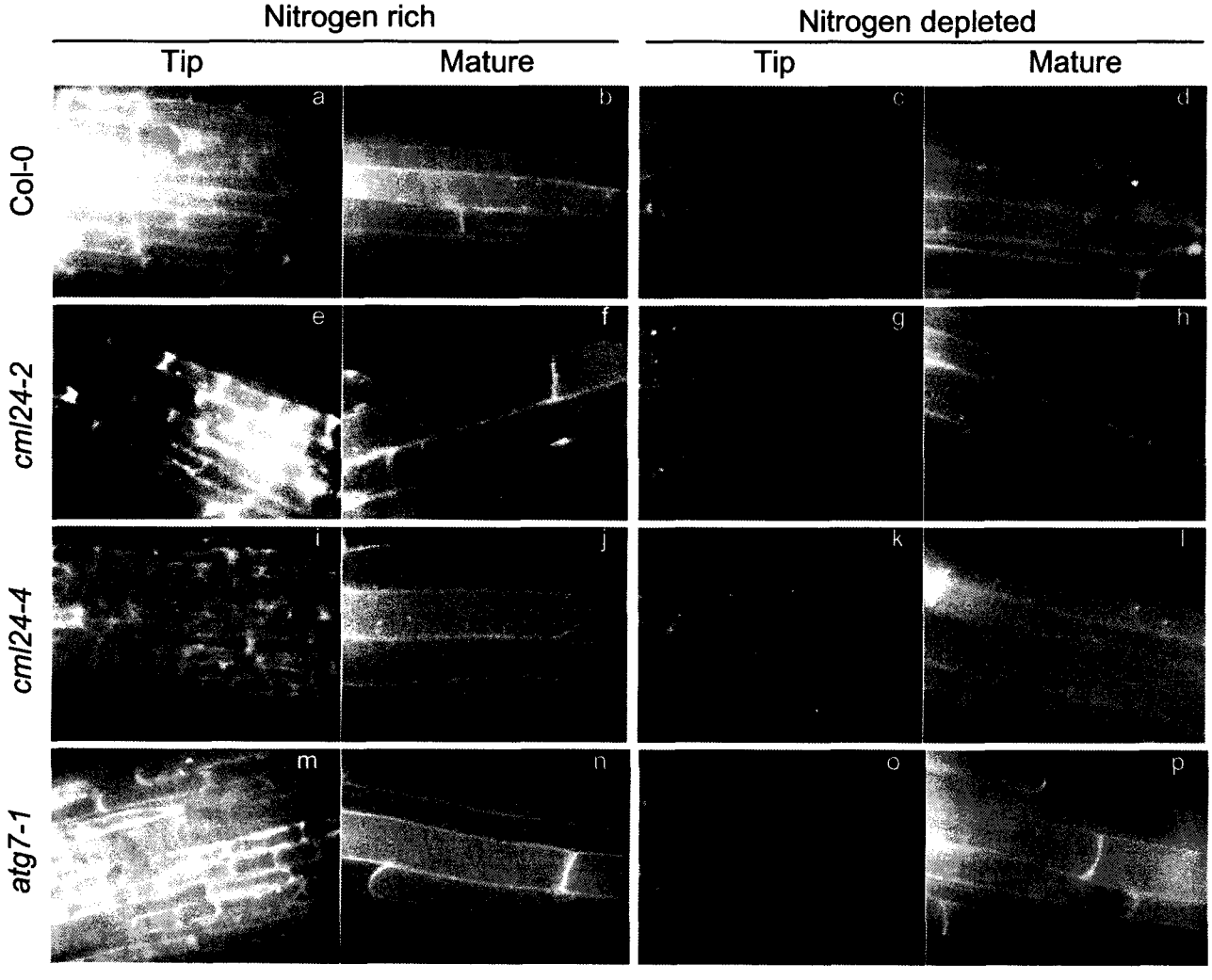

Fig 6.8 MDC staining of the root tips and mature root cells of wild type (Col-0), *cml24-2*, *cml24-4*, and *atg7-1*. Ten-day-old plants were transferred to nitrogen rich media (left panels) media lacking nitrogen (right panels) and grown in the light for three days. Roots were stained with MDC for 10 min and visualized by fluorescence microscopy.

root tips grown without nitrogen (Figure 6.8o). The results suggest that Col-0 root tips accumulate more punctate MDC fluorescence in response to nitrogen-depletion relative to *atg7-1*. However, these MDC staining particles in root tips may be produced independently of ATG7.

In Col-0 mature root cells, the punctate MDC fluorescence does not significantly increase after nitrogen starvation (Figure 6.8b), and *atg7-1* has no detectable fluorescence particles in mature root cells (Figure 6.8n and 6.8p). These results suggest that Col-0 mature roots cells have autophagosomes that stain with MDC and their formation depends on ATG7 function. However, three days of growth on media lacking nitrogen may not be sufficient to alter autophagosome abundance.

I compared MDC punctate fluorescence accumulation in *cml24-2* and *cml24-4* root tips grown in complete and nitrogen-depleted media (Figure 6.8). Overall, because punctate root tip MDC staining occurs in *atg7-1* at levels comparable to Col-0, differences in the *cml24* mutants are difficult to interpret. Therefore, I focused on MDC data in the mature root cells.

In *cml24-2* and *cml24-4* mature root cells, MDC fluorescent particles accumulated in both complete and nitrogen-depleted media (Figure 6.8f, 6.8h, 6.8j, and 6.8l). These punctate fluorescence particles showed random movement suggesting that they are free-floating within the vacuole as reported for autophagic bodies (Contento et al., 2005). There may be more MDC fluorescent particles in *cml24-2* and *cml24-4* mature root cells than in Col-0, but as yet I have not yet been able to quantify a difference. However, these data suggest that MDC-labeled autophagosome structure can form in the *cml24* mutants, and therefore, CML24 may not be required for autophagosome formation.

The effect of CML24 on autophagosome formation could also be assessed using plants with altered *CML24* expression levels. Overexpressing (*O1*) and underexpressing (*U1*) *CML24* transgenics of the RLD accession have increased and decreased CML24 protein accumulation, respectively (Delk et al., 2005). Seven-day-old seedlings were transferred to nitrogen-rich or nitrogen-depleted media for six days. Some of wild-type (RLD) mature root cells had low amounts of punctate MDC fluorescence in nitrogen-rich media (Figure 6.9, three left top panels), and the abundance of these fluorescent particles was increased after growth without nitrogen for 6 days (Figure 6.9, three left bottom panels). These results suggest that 6 days without nitrogen may be sufficient to increase autophagosome formation at least in the RLD background.

Both *O1* and *U1* had higher MDC fluorescence in nitrogen-rich media relative to wild type (Figure 6.9, MS). In addition, *O1* and *U1* MDC staining punctate structures appear less abundant than wild type after six days of nitrogen starvation (Figure 6.9). These results suggest that either increasing or decreasing CML24 protein accumulation may lead to enhanced basal autophagosome accumulation in mature root cells; therefore autophagy regulation may require wild-type levels of CML24. Reduced MDC staining in O1 and U1 transgenic roots after 6 days of growth without nitrogen relative to wild type may indicate that either the transgenics are unable to properly induce autophagosome formation in response to nutrient deprivation or that enhanced constitutive autophagy may exhaust available cellular components for recycling after a long-term starvation.

6.2.2 GFP-ATG8e fluorescence analysis

MDC staining has been reported to label only mature autophagosomes (Bampton et al., 2005). Autophagosome membrane expansion and ATG8 recycling would likely be

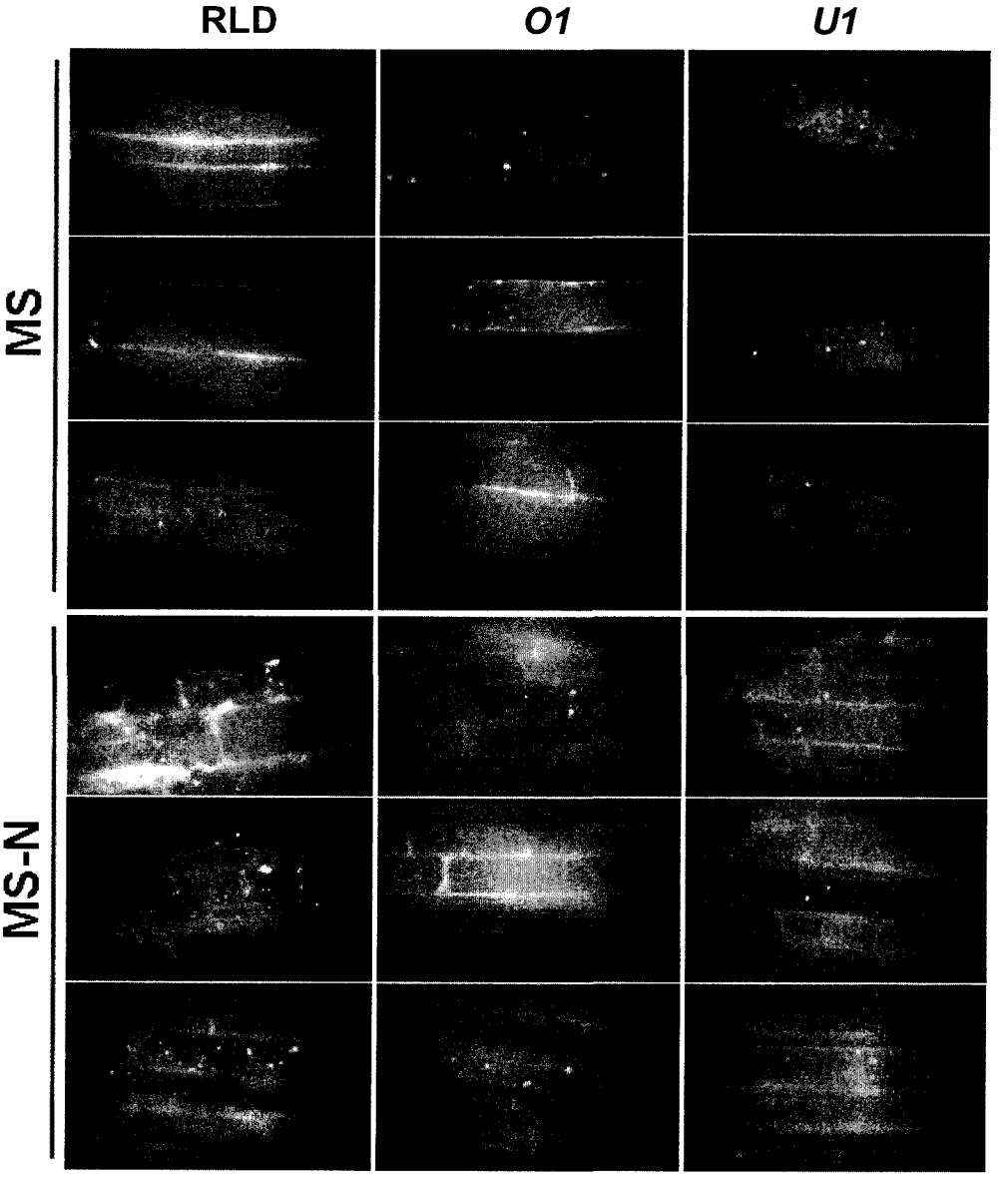

Fig 6.9 MDC staining of the root tips of wild type (RLD) and *CML24* overexpressing (*O1*) and underexpressing (*U1*) transgenics. One-week-old plants were transferred to media with (MS) or without nitrogen (MS-N) and grown in the light for 6 days. Roots were stained with MDC for 10 min and visualized by fluorescence microscopy.

affected by altered ATG4 activity levels (Kirisako et al., 2000b; Yoshimoto et al., 2004). To assess whether CML24 may affect early autophagosome membrane assembly and verify effects on mature autophagosome accumulation, I sought to follow autophagy progression using a Green Fluorescent Protein (GFP)-tagged ATG8. GFP-ATG8 is a well-characterized tool to monitor autophagy progression (Contento et al., 2005). I obtained CaMV35S:GFP-ATG8e transgenic plants from Dr. Bassham (U of Iowa). The CaMV35S regulatory region is thought to drive strong and relatively constitutive expression.

To avoid differences in GFP-ATG8e expression due to CaMV35S:GFP-ATG8e genomic insertion sites, I crossed the *GFP-ATG8e* reporter into *cml24-2* and *cml24-4* instead of introducing the transgene by transformation. The *cml24-4/GFP-ATG8e* transgenic line revealed comparable *GFP-ATG8e* transcript levels relative to the original *GFP-ATG8e* transgenic (data not show). However, *cml24-2/GFP-ATG8e* plants showed GFP fluorescence in only roots but not shoots; *GFP-ATG8e* transcript levels were also low in shoots (data not shown). The lower *GFP-ATG8e* transcript levels in *cml24-2/GFP-ATG8e* may be due to epigenetic silencing.

Autophagy induction has been reported under nitrogen-depleted, carbon-limited, and nitrogen/carbon ratio unbalanced conditions (Bassham et al., 2006; Rose et al., 2006). I monitored GFP-ATG8e fluorescence in the roots of wild type, *cml24-2*, and *cml24-4 CaMV35S:GFP-ATG8e* transgenics. Seven-day-old seedlings were transferred to media lacking nitrogen and incubated in the light or dark for two days (Figure 6.10). Darkness should result in fixed carbon deprivation.

In Col-0/*GFP-ATG8e* roots, most GFP signal is diffuse with some apparent

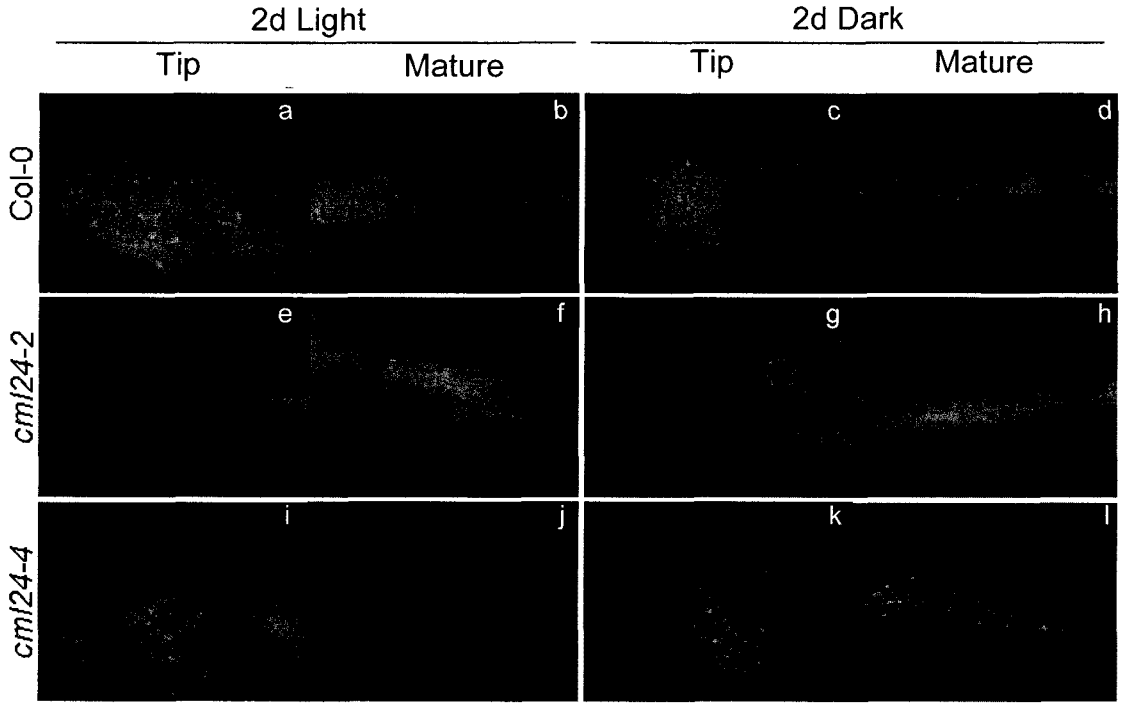

Fig 6.10 Effect of darkness on behavior of GFP-ATG8e fluorescence in stably transformed roots. One-week-old GFP-ATG8e transgenic seedlings of *Col-0*, *cml24-2*, and *cml24-4* genotypes, were transferred to nitrogen free media and incubated for two days light (left panels) or dark (right panels). Both root tips and mature root cells GFP fluorescence is visualized by fluorescence microscopy. $n \geq 4$.

nuclear staining in the root tips (Figure 6.10a) and punctate structures in mature roots (Figure 6.10b) after two days growth on media lacking nitrogen in the light. The abundance of punctate GFP fluorescence structures was increased in both root tips and mature roots in Col-0 after two days of darkness and nitrogen starvation (Figure 6.10c and d). These results suggest that GFP-ATG8e labeled structure accumulation can be induced by adding darkness stress to nitrogen-limited growth conditions.

Compared to Col-0/*GFP-ATG8e* root tips, *cml24-2/GFP-ATG8e* transgenic root tips had more abundant punctate GFP fluorescence after growth in the absence of nitrogen for two days in the light (Figure 6.10e). Only a few fluorescence particles were detected in mature root cells (Figure 6.10f), possibly fewer than seen in comparable Col-0 cells. Unlike Col-0/*GFP-ATG8e*, *cml24-2*/GFP-ATG8e transgenic root tips have comparable punctate GFP fluorescence under both light and dark conditions when grown on media lacking nitrogen (Figure 6.10g and h). In contrast to root tip cells, the *cml24-2* transgenic mature root cells may have fewer GFP labeled structures than the Col-0 transgenic under comparable conditions. Although the *cml24-2* transgenic differs from Col-0 in a root-region dependent manner, the most striking difference is that GFP-ATG8e labeled structures are abundant in *cml24-2* root tips after two days of light growth whereas few, if any, are detected in Col-0. This suggests that *cml24-2* forms autophagosome membranes under conditions when wild type does not.

cml24-4/GFP-ATG8e transgenics appeared to have more abundant punctate GFP fluorescence in mature root cells and root tips relative to Col-0/*GFP-ATG8e* under nitrogen-free and light-growth conditions (Figure 6.10i and 6.10j). The levels of punctate fluorescence in *cml24-4/GFP-ATG8e* did not change robustly in response to darkness

treatment (Figure 6.10k and l). These results suggest that both the *cml24-2* and *cml24-4* alleles cause increased abundance of GFP-ATG8e fluorescent structures relative to wild type transgenics under nitrogen-limited growth in the light. However, *cml24-2* and *cml24-4* may have opposite regulation of GFP-ATG8e labeled structure formation in mature root cells. *cml24-2* has reduced fluorescent structures in plants grown in absence of nitrogen and light, while *cml24-4* has higher abundance of fluorescence punctate structures even without the darkness treatment.

One possibility is that CML24 may affect ATG4 activity in a way that could influence the earliest events in autophagosome membrane assembly, therefore I investigated whether the *cml24* mutants have differences in GFP-ATG8e labeling early in autophagy induction. GFP-ATG8e transgenic seedlings were grown in nitrogen-rich media for 7 days, then transferred to nitrogen free media and incubated in the dark for 0, 12, 24, 38, and 48 hours (Figure 6.11). In Col-0 mature root cells, some diffuse GFP signal is detected at 0 hours (Figure 6.11a). After 12, 24, and 38 hours of treatment, GFP fluorescence begins to accumulate in a pattern that resembles cytosolic staining (Figure 6.11b, c, d, green arrows). This apparent change in GFP fluorescence localization suggests that ATG8 is remobilized after 12 to 38 hours of loss of light and nitrogen availability. GFP-ATG8e punctuate structures appear after 48 hours treatment in the wild type transgenic (Figure 6.11e). Although asimilar fluorescence relocation occurs in *cml24-2* mature root cells, the staining pattern changes are not as stark as in Col-0, nor does punctate staining occur at 48 hours post treatment (Figure 6.11f-j). At 0 hours, *cml24-4/GFP-ATG8e* transgenic mature root cells have GFP staining that largely resembles that of the Col-0 transgenics, except that they have more distinct nuclear and

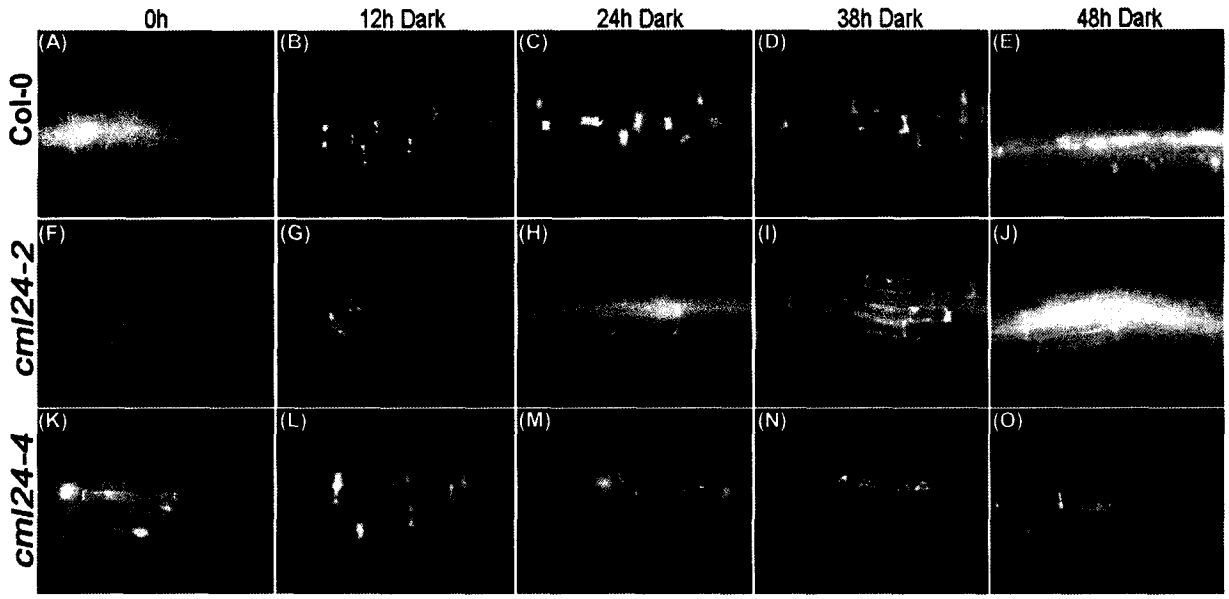

Fig 6.11 GFP-ATG8e fluorescence of darkness and nitrogen depleted treated mature root cells. One-week-old GFP-ATG8e transgenic seedlings of wild type (Col-0), *cml24-2* and *cml24-4* were transferred from nitrogen-rich media to nitrogen-free (MS-N) media and incubated in darkness for different time periods. Green arrows indicate GFP fluorescence consistent with cytosolic accumulation. GFP fluorescence is visualized by fluorescence microscopy.

possibly more punctate staining. The *cml24-4* root cells also resemble those of Col-0 in that GFP fluorescence relocalized after 12 and 24 hours or treatment (Figure 6.11l, m green arrows). However, *cml24-4* also developed small punctuate structures earlier than seen in Col-0 (Figure 6.11m,n); nearly all the GFP fluorescence is restricted to particulate form, without much diffuse fluorescence, at 48 hours post treatment. These data are consistent with the interpretation that the *cml24* mutant root cells respond to nutrient deprivation through changes in ATG8 localization similarly to Col-0, but the kinetics of these responses are altered in the mutants relative to wild type.

In addition, based on previous MDC and GFP fluorescence results (e.g., Figure 6.8, 6.10), autophagosome formation and/or accumulation may be variable depending upon the maturation stage of the root cells. Therefore, I imaged three different root regions, including the root tip and two portions of the differentiation zone (Figure 6.12, left to right columns). The age and maturation of root cells increase more proximally. GFP-ATG8e transgenic seedlings of Col-0, *cml24-2*, and *cml24-4* were grown on rich media for 7 days and roots were imaged (Figure 6.12, 0h). Col-0/*GFP-ATG8e* transgenics accumulated some GFP punctate structures, consistent with a low basal level of constitutive autophagy, both in root tips (Figure 6.12a) and mature root cells (Figure 6.12b, c, 0h), in addition to some diffuse GFP fluorescence.

cml24-2/GFP-ATG8e root tips had punctate GFP fluorescence and lower diffuse GFP fluorescence relative to Col-0 (Figure 6.12g, 0h). In mature root cells, *cml24-2/GFP-ATG8e* transgenics had fewer punctate GFP fluorescence structures than Col-0 (Figure 6.12h, i, 0h). *cml24-4/GFP-ATG8e* root tip GFP fluorescence was similar to Col-0/*GFP-ATG8e* (Figure 6.12m). However, more and/or larger GFP fluorescence structures

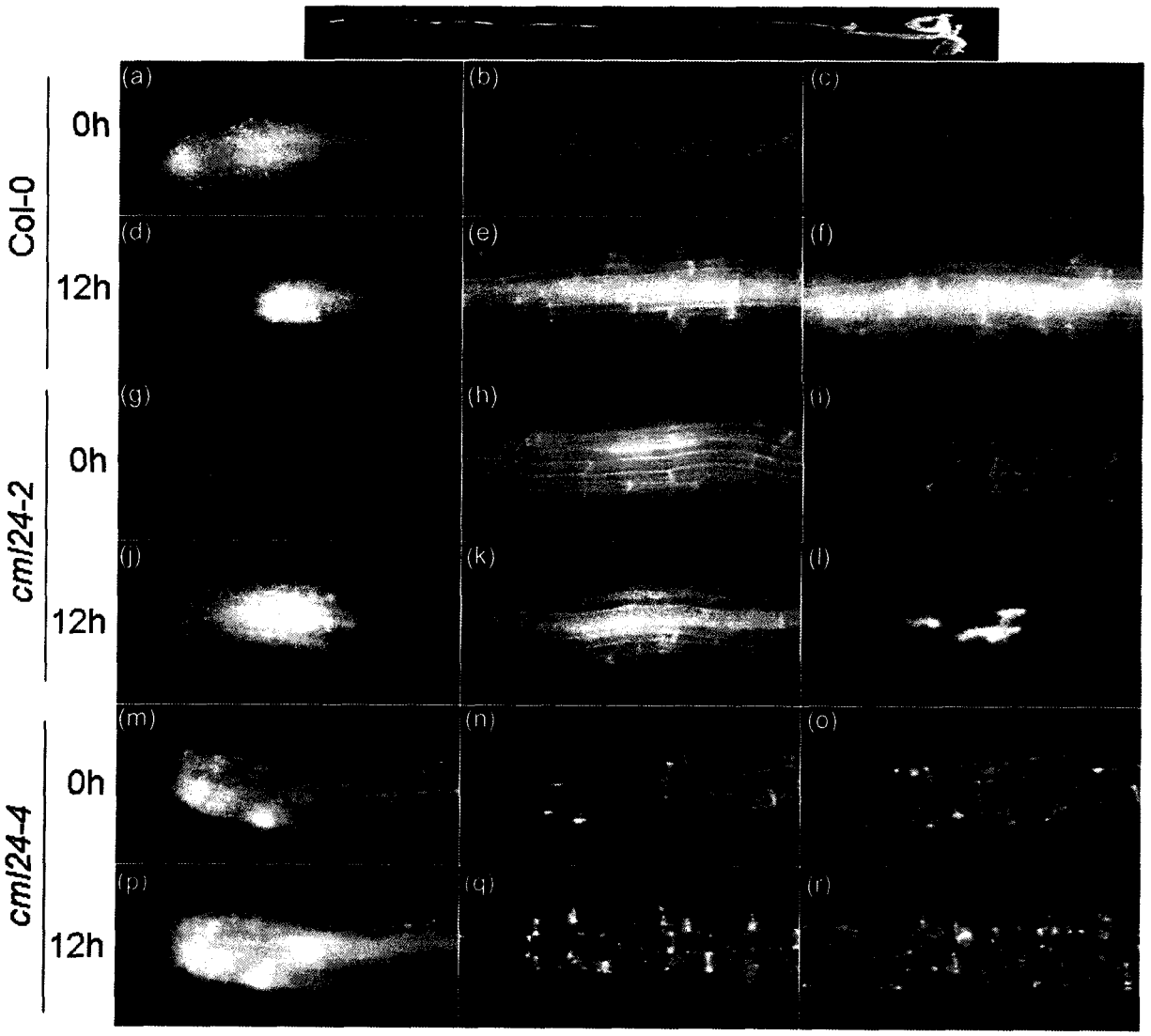

Fig 6.12 GFP-ATG8e fluorescence in control (0h) and nitrogen depleted and autophagy inhibitor, E64d, treated roots (12h). One-week-old GFP-ATG8e transgenic seedlings of wild type (Col-0), *cml24-2* and *cml24-4* were transferred from nitrogen-rich (MS) media to nitrogen-depleted media with E64d incubated for 12 hours. Images were taken from three different regions of roots (approximate regions indicated red boxes in the top image) from root tips toward mature zone (left to right panels). GFP fluorescence is visualized by fluorescence microscopy.

accumulated in *cml24-4/GFP-ATG8e* mature root cells in comparison to Col-0/*GFP-ATG8e* (Figure 6.12n, and 6.12o).

To try to improve visualization of ongoing autophagy, I treated roots with E64d, a protease inhibitor reported to inhibit autophagic body breakdown in the vacuole (Matsuoka, 2008; Moriyasu and Inoue, 2008). In wild type, after 12 hours of growth on nitrogen-free media with E64d, the overall GFP fluorescence increased in mature root cells but not root tips (Figure 6.12d, e, f). This may indicate that mature root cells, which have higher efficiency to take up media components, are more sensitive to nitrogen-depletion and/or E64d treatment. *cml24-2* has high fluorescence before and after the treatment (Figure 6.12h, k). In the mature zone of *cml24-2*, there is also some aggregate GFP labeled structures accumulation (Figure 6.12l). On the other hand, the GFP punctate structures appearing with nitrogen-free growth and E64d treatment in *cml24-4/GFP-ATG8e* appear larger (Figure 6.12p, q and r) relative to 0 hour non-treated roots (Figure, 6.12n and 6.12o). Some cytosolic GFP fluorescence also appears in mature root cells, consistent with previous data for 12-hour darkness treatment of *cml24-4/GFP-ATG8e* (Figure 6.11l). These results also confirm that GFP fluorescence is not uniform in different root regions.

These GFP-ATG8e transgenic data are consistent with the previous findings of reduced abundance of autophagosomes in *cml24-2*. *cml24-4* may have more autophagosome formation than wild type.

6.3 The *cml24* mutants have altered ATG8 protein accumulation

I hypothesize that CML24 interacts with and regulates ATG4b. Since ATG4 primes and recycles ATG8 (Figure 1.5) and such activities may affect overall ATG8

accumulation, I predict that mis-regulation or loss of ATG4 activity would affect ATG8 accumulation. To test these ideas, I investigated whether ATG8 levels are altered in the *atg4a4b* double mutant relative to Col-0. In addition, if CML24 affects ATG4 activity *in vivo*, I would predict that *cml24-2* and *cml24-4* may also have altered ATG8 levels.

6.3.1 The *cml24* mutants have altered endogenous ATG8 accumulation levels

To enable quantification of endogenous ATG8 levels in plants, I obtained an anti-ATG8a antibody from Dr. Ohsumi (National Institute for Basic Biology, Okazaki, Japan) for use on western blots. This antibody crossreacts with AtATG8a to AtATG8h isoforms produced in yeast (Yoshimoto et al., 2004). I purified recombinant ATG8e protein from bacteria and affinity purified the anti-ATG8e antibody before use. I also used the purified ATG8e protein as an antigen for antibody production. However, the initial attempt yielded a poor titer antibody that cross-reacts with other proteins. This antibody should be affinity purified and re-tested to determine whether it will be useful.

I used the anti-ATG8a antibody to monitor ATG8 accumulation in Col-0, *atg4a4b*, and the *cml24* mutants. Because the ATG4 activity levels may differentially affect soluble ATG8 versus membrane-associated, lipid-linked, ATG8e, I extracted both soluble protein and detergent-released protein from insoluble protein pellets after centrifugation. In Col-0, ATG8 was detected only in the aqueous-soluble protein fraction; no detectable ATG8 was found in the detergent-soluble fractions (Figure 6.13, Col-0). *atg4a4b* showed less ATG8 accumulation in the aqueous-soluble fraction and the protein detected displayed different mobility than that from Col-0. The overall decreased levels of aqueous-soluble ATG8 may be the consequence of ATG4 activity loss. Lack of ATG4 activity may also affect either which specific ATG8 isoforms accumulate or

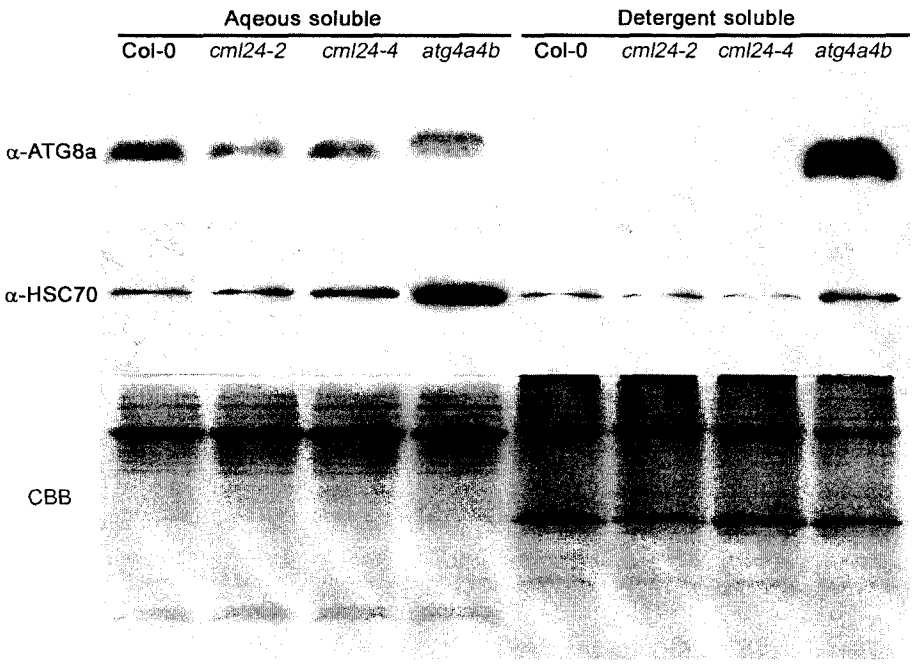

Fig 6.13 ATG8 protein accumulation in Col-0, *cml24-2*, *cml24-4*, and *atg4a4b*. Two-week-old plants were grown under constant light. Aqueous-soluble proteins are shown in left panel; detergent-soluble proteins are shown in right panel. Proteins were separated on 15% SDS-PAGE and immunoblotted with α-ATG8a (top panel) first and α-HSC70 (middle panel). Total proteins were stained with coomassie brilliant blue (CBB) (bottom panel) in the gel after transfer to verify similar protein amounts loaded in all lanes. The experiment has been repeated twice with similar results.

posttranslational ATG8 modifications, such as preservation of the ATG8 carboxyl-terminus; these differences may result in an altered SDS-PAGE migration. In detergent-soluble protein fractions of *atg4a4b*, ATG8 shows dramatic overaccumulation. This protein may represent ATG8 conjugated to phosphatidylethanolamine (PE) or other lipid due to loss of deconjugation activity by ATG4. Alternatively, loss of ATG4 activity, and thus autophagy, may lead to overaccumulation of ATG8 because ATG8 is no longer subjected to autophagy-mediated degradation. Overaccumulated ATG8 may be found in the insoluble protein fraction because of its tendency to self associate (Yoshimoto et al., 2004). If this accumulated protein is ATG8-PE, we would hypothesize that the protein is most likely ATG8h because ATG8h, which has a carboxyl terminal Gly, does not require ATG4 priming activity prior to PE conjugation. In addition, ATG8h is recognized by the anti-ATG8a antibody and therefore should be imaged by the western analysis. Similarly to wild type, ATG8 is found only in the soluble fraction of both *cml24* mutant extracts (Figure 6.13, "*cml24-2*" and "*cml24-4*"). However, both *cml24* mutants have reduced aqueous-soluble ATG8 levels relative to wild type. These results suggest that *cml24* mutants still have at least some ATG4 activity; however, the lower ATG8 accumulation may be a consequence of alterations in ATG4 regulation as a consequence of *cml24* mutations.

Figure 6.13 also shows unexpected HSC70 (Heat Shock protein Cognate 70) accumulation in *atg4a4b*. Anti-HSC70 was used originally as a control for protein loading. However, these data indicate that HSC70 accumulates to high levels in *atg4a4b* (Figure 6.13). Because HSC70 has a role in protein folding and turnover, HSC70 may be induced to accumulate when other cellular mechanisms of protein degradation, such as

autophagy, are defective, as expected in an *atg4a4b* mutant (Figure 6.13, compare middle and bottom panel). In addition, It has been reported that several HSCs are degraded through autophagy (Kirkin et al., 2009; Shen et al., 2009) and therefore HSC70 may accumulate in *atg4a4b* because of defective autophagy.

I sought to verify the result shown in Figure 6.13 and to determine whether ATG8 levels vary in wild type and the mutants under conditions, such as darkness, that induce autophagy. Three-week-old short photoperiod (8h light/16h dark) grown plants were harvested one hour after lights were turned on (Figure 6.4, "1L") or off (Figure 6.4, "1D"). I extracted aqueous- and detergent-soluble proteins for western analysis. In the aqueous-soluble protein fractions, Col-0 accumulated similar levels of ATG8 after shift from dark to light (Figure 6.14a, "Col-0", "1L") or light to dark (Figure 6.14a, "Col-0", "1D"). The abundance of detergent-soluble ATG8 was slightly lower after one hour darkness relative to levels after the shift to light (Figure 6.14b, "Col-0"). Since ATG8 was not present in detergent-soluble protein Col-0 grown in constant light period (Figure 6.13), but is present in detergent-soluble protein extracts of plants grown in short photoperiods, a greater fraction of ATG8 may be lipid-associated in short-day grown plants.

Aqueous-soluble ATG8 accumulates regardless of light conditions in *atg4a4b* but the band mobility pattern is again distinct from that seen for Col-0 (Figure 6.14a, "*atg4a4b*"). *atg4a4b* also accumulated high levels of detergent-soluble ATG8 under both light conditions (Figure 6.14b, "*atg4a4b*"), consistent with previous results found with plants grown under constant light (Figure 6.13). The ATG8 levels in *atg4a4b* are not affected by changes in light treatments.

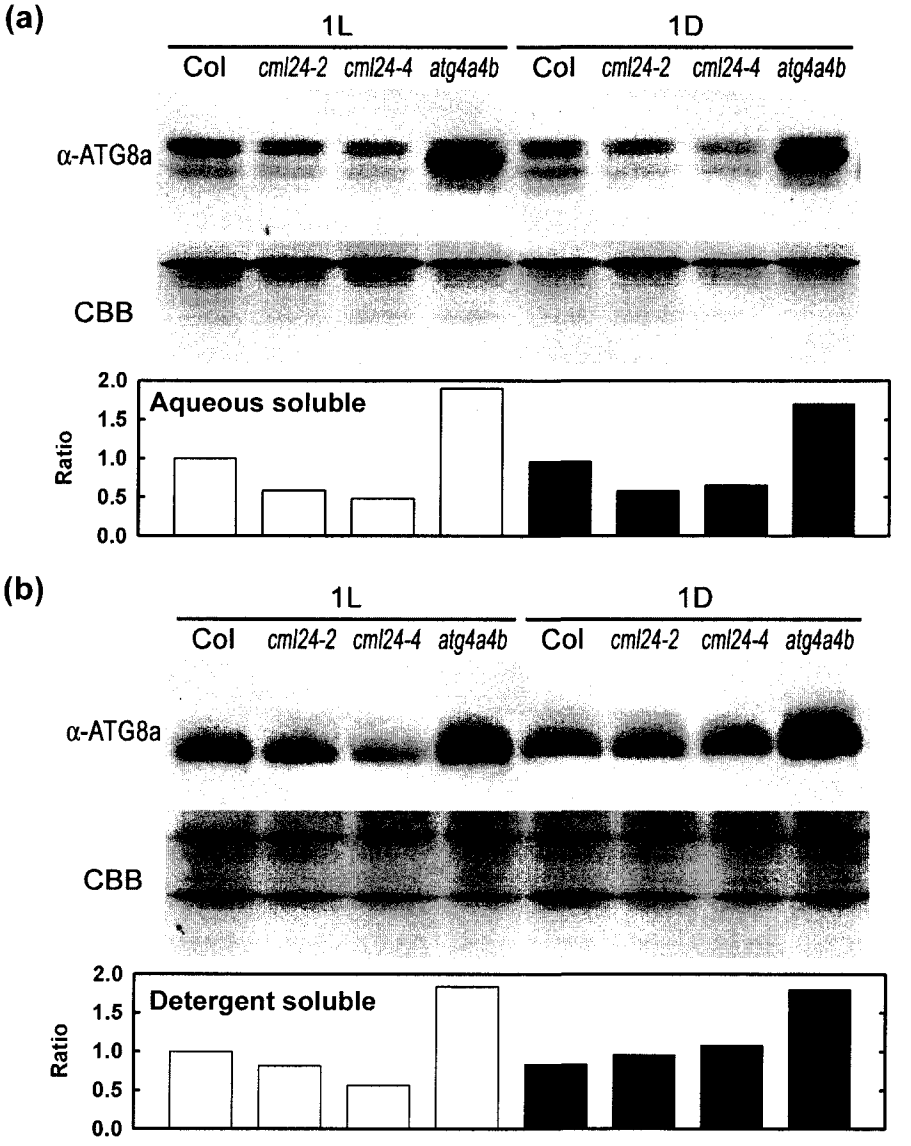

Fig 6.14 ATG8a protein accumulation in short photoperiod growth Col, *cml24-2*, *cml24-4*, and *atg4a4b* plants grown under short photoperiods. Plants were harvested one hour after the shift to light (1L) or dark (1D). Aqueous- (a) and detergent- (b) soluble proteins were extracted. Proteins were separated on 15% SDS-PAGE and followed by analysis with anti-ATG8a western blotting. Total proteins were stained with coomassie brilliant blue (CBB). The intensity of anti-ATG8a was normalized with CBB staining, and protein levels in light-harvested Col-0 was defined as 1 for quantification. The experiment has been repeated twice with similar results.

cml24-2 and *cml24-4* had decreased levels of aqueous-soluble ATG8 accumulation relative to Col-0 in extracts from plants harvested under both light and dark conditions (Figure 6.14a, "1L" and "1D"). Both *cml24-2* and *cml24-4* also had decreased levels of detergent-soluble ATG8 in plants harvested in the light; however, the detergent-soluble ATG8 levels were slightly increased in *cml24-2* and *cml24-4* dark-harvested plants relative to wild type (Figure 6.14b). These results confirm that *cml24* mutants may accumulate less aqueous-soluble ATG8. In addition, detergent-soluble ATG8 accumulation may be influenced by light conditions, and *cml24* mutants may have slower turnover rate of detergent-soluble ATG8 in darkness relative to Col-0.

6.3.2 The *cml24* mutants show altered GFP-ATG8e accumulation patterns

GFP-ATG8e is another well characterized marker useful for monitoring autophagy (Contento et al., 2005; Phillips et al., 2008; Slavikova et al., 2008; Yano et al., 2007; Yoshimoto et al., 2004). *cml24* mutants transformed with *GFP-ATG8e* revealed distinct fluorescence patterns relative to Col-0 (Figure 6.10, 6.11 and 6.12). To assess whether the visualized GFP-ATG8e fluorescence patterns reflect ATG8 progression through autophagy, I monitored GFP-ATG8e accumulation and breakdown by anti-GFP westerns. GFP is thought to be rapidly cleaved from the fusion protein upon entering the vacuole. The released GFP moiety is stabilized especially in the presence of Concanamycin A (ConA), which inhibits vacuolar ATPases (Flückiger et al., 2003). By using GFP-ATG8e transgenics, I sought to compare GFP-ATG8 progression to the vacuole in wild type and *cml24* mutant plants.

Based on previous GFP-ATG8e fluorescence transgenics results (Figure 6.11 and 6.12), I expect that 12 hours on nitrogen-free media may be long enough to induce the

onset of autophagy. Therefore, I transferred 7-day-old GFP-ATG8e transgenic plants to nitrogen rich or free media for 12 hours before harvesting. Immunoblotted proteins analyzed with anti-GFP revealed three different molecular weight bands (Figure 6.15). The slowest migrating band may be full length GFP-ATG8e. The faint band often present just below this major band may be a lipid-modified GFP-ATG8e. Phosphatidyl-ethanolamine (PE)-linked ATG8 runs faster than the unmodified ATG8 through SDS-PAGE (Fujioka et al., 2008; Yoshimoto et al., 2004). Alternatively, this band could result from partial breakdown of GFP-ATG8e. The low molecular weight band size is consistent with that of free GFP (Figure 6.15).

In Col-0/*GFP-ATG8e*, full length GFP-ATG8e remains relatively constant with and without 12-hr of nitrogen starvation (Figure 6.15, "Col-0", "N, +, -"). To attempt to slow vacuolar degradation of GFP-ATG8e, GFP-ATG8e transgenics were incubated with ConA to inhibit vacuolar proteases (Yoshimoto et al., 2004). In the presence of ConA, free GFP accumulates under both nitrogen-rich and -free media growth conditions (Figure 6.15, "Col", "+ConA"). The results reveal that autophagy likely occurs even in presence of nitrogen, but that degradation of free GFP is usually complete and so not detected. ConA treatment may delay this breakdown of GFP. Free GFP levels are elevated more in nitrogen-free ConA-treated plants consistent with the expectation that in response to reduced nitrogen autophagy is induced, leading to increased degradation of GFP-ATG8e.

cml24-2/GFP-ATG8e may have slightly lower levels of GFP-ATG8e relative to Col-0 in nitrogen rich media (Figure 6.15, "*cml24-2*"). However, *cml24-2* has very low GFP-ATG8e when grown on nitrogen-free media (Figure 6.15, "*cml24-2*", "N, -").

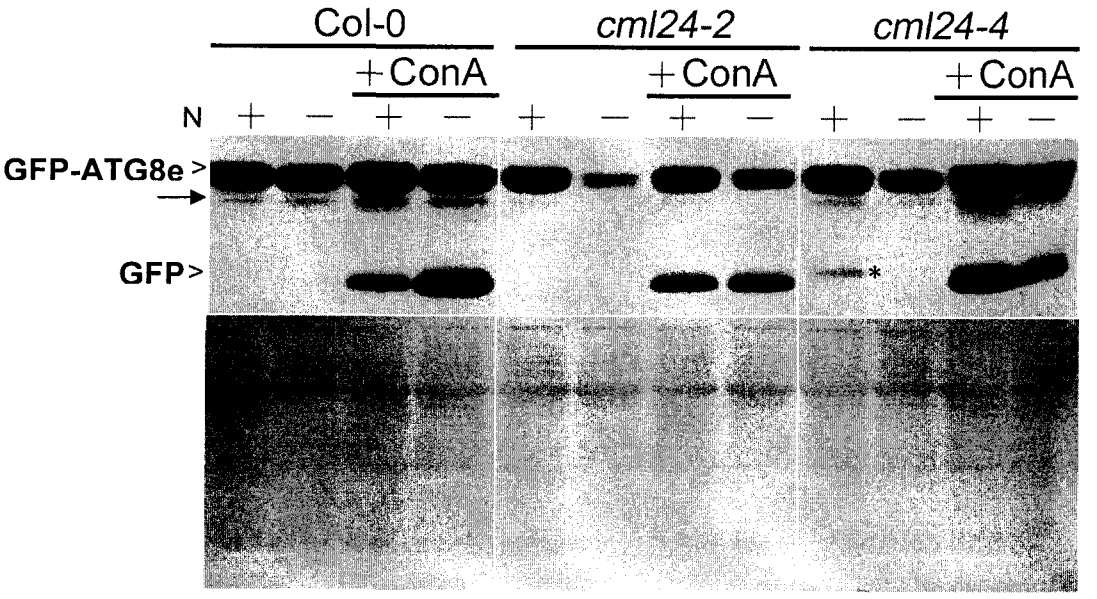

Fig 6.15 GFP-ATG8e accumulation in plants transferred to nitrogen-depleted media. 7-day-old seedlings were incubated with or without ConA for 12 hours in nitrogen rich (+) or depleted (-) media. Total proteins were extracted subjected to SDS-PAGE and immunoblotted with anti-GFP antibody (top panel).Full length GFP-ATG8e protein (GFP-ATG8e) and free GFP are labeled at left. Arrow labels lower molecular mass band; asterisks indicates small band of unknown origin. Bottom panel, total blotted proteins were stained by Ponceau S. The experiment has been performed once.

Similarly to Col-0, upon ConA treatment, free GFP accumulates in *cml24-2/GFP-ATG8e* transgenics. However, the relative abundance of the free GFP in *cml24-2* is higher than that seen for Col-0 (Figure 6.15, "+ConA, N+"), suggesting that basal autophagy may be higher in *cml24-2* than Col-0. In addition, in nitrogen-free media, ConA appears to slow the degradation of the GFP-ATG8e in *cml24-2*. This effect of ConA is consistent with the interpretation of *cml24-2*'s reduced GFP-ATG8e under low nitrogen may be the consequence of vacuole protease-dependent degradation, possibly autophagy. One interpretation of these results is that *cml24-2* has higher basal autophagy than Col-0 and, as a consequence, a nitrogen availability reduction can rapidly deplete available ATG8 by an induction of autophagy. However, it is difficult at this time to reconcile these data with that in Figure 6.12. While *cml24-2* may have higher basal autophagy than Col-0, the data are, as yet, unclear as to whether *cml24-2* displays increased autophagy in response to nitrogen deprivation.

cml24-4/GFP-ATG8e, like *cml24-2/GFP-ATG8e*, has less full-length GFP-ATG8e when grown on nitrogen-free media (Figure 6.15, "*cml24-4*") than when on nitrogen-rich media. On nitrogen-rich media in the presence of ConA, *cml24-4/GFP-ATG8e* accumulated higher free GFP levels than wild type, suggesting that *cml24-4*, in addition to *cml24-2*, may undergo higher rates of constitutive autophagy. Full length and free GFP accumulate in *cml24-4* when grown in nitrogen free media with ConA is similar to wild type. The minor band migrating just below the full-length GFP-ATG8e band is seen in most of the Col-0/*GFP-ATG8e* and *cml24-4/GFP-ATG8e* protein samples. *cml24-2* fails to accumulate this band to detectable levels. This could be because overall levels of GFP-ATG8e are reduced in *cml24-2* or that *cml24-2* fails to accumulate the lipid

linked form of GFP-ATG8e. Further analysis will be required to interpret these differences. Additionally, a band near the size of free GFP appears in *cml24-4* grown on nitrogen-rich media; the identity of this protein is undetermined as yet.

These results indicate that the *cml24* mutants can conduct degradation of GFP-ATG8e in a manner consistent with autophagy. The lower accumulation levels of GFP-ATG8e in the *cml24* mutants, especially *cml24-2*, may indicate accelerated degradation or reduced synthesis. The finding that ConA treatment leads to higher GFP-ATG8e accumulation is consistent with alterations in protein degradation regulation, potentially through a change in ATG4 activity and autophagy progression.

6.4 *cml24* mutants have aberrant root elongation

In response to limited nutrient growth conditions, autophagy is thought to play a role to re-mobilize nutrients by recycling organelle and protein components in cells (Bassham et al., 2006; Wada et al., 2009). In plants, failure to appropriately regulate autophagy would be expected to cause growth inhibition in nutrient-limited conditions. Indeed, relative to wild type, *atg4a4b* roots have been reported to be shorter when seedlings are grown under nitrogen-depleted conditions (Yoshimoto et al., 2004). Arabidopsis primary root elongation can be affected by low nutrient content or different nutrient ratios in the media. For example, primary root length is decreased relative to shoot dry weight as nitrate levels are increased in the media (Linkohr et al., 2002). Seedlings grown under nitrogen-limited conditions have altered root/shoot ratios with more growth targeted to the root (Linkohr et al., 2002). This differential growth may be an acclimation response enabling seedlings to access nutrients available at greater distances. On the other hand, root elongation also can be inhibited with high levels of

sucrose or glucose (Laetsch and Briggs, 1963). I hypothesized that autophagy would be activated under nitrogen-limited conditions to provide the recycled components necessary to allow enhanced root elongation.

If *CML24* has a role in regulating autophagy, *CML24* mutants would be expected to show altered growth under nutrient limitation. I compared *cml24* mutant and wild type root elongation after seedling transfer to nitrogen-free (MS-N) or -rich (MS) media with (Figure 16.16a) or without (Figure 16.16c) 0.5% sucrose under constant light. Root length was measured after three days. Wild type (Col-0) had longer root elongation under nitrogen-depleted media relative to rich media in both 0.5% and 0 sucrose (Figure 16.16a and c). The autophagy mutant, *atg4a4b*, had longer primarily roots relative to wild type in MS with sucrose media and the root length did not further increase in nitrogen-free media. These results are inconsistent with a previous report (Yoshimoto et al., 2004); the inconsistency may be because the two mutants examined are of different ecotype backgrounds. *cml24-2* had short roots on both MS and MS plus sucrose media relative to wild type and did not respond to nitrogen-free conditions (Figure 6.16a and c). *cml24-4* had a similar root elongation response to nitrogen-free media as wild type (Figure 6.16b and d). The wild type root length ratio on MS-N to MS is approximately 1.5 whereas *atg4a4b* is close to 1 (Figure 16.16b). This suggests that the autophagy mutant fails to respond to nitrogen limitation to promote root elongation. *cml24-2* MS-N to MS root length ratio is also close to 1, suggesting that it is unable to elongate roots in response to low nitrogen. However, the severe short roots in *cml24-2* may be related to other functions of CML24 because root growth is inhibited even in nutrient-rich conditions. Interestingly, although *cml24-4* demonstrates low nitrogen induced root elongation, the

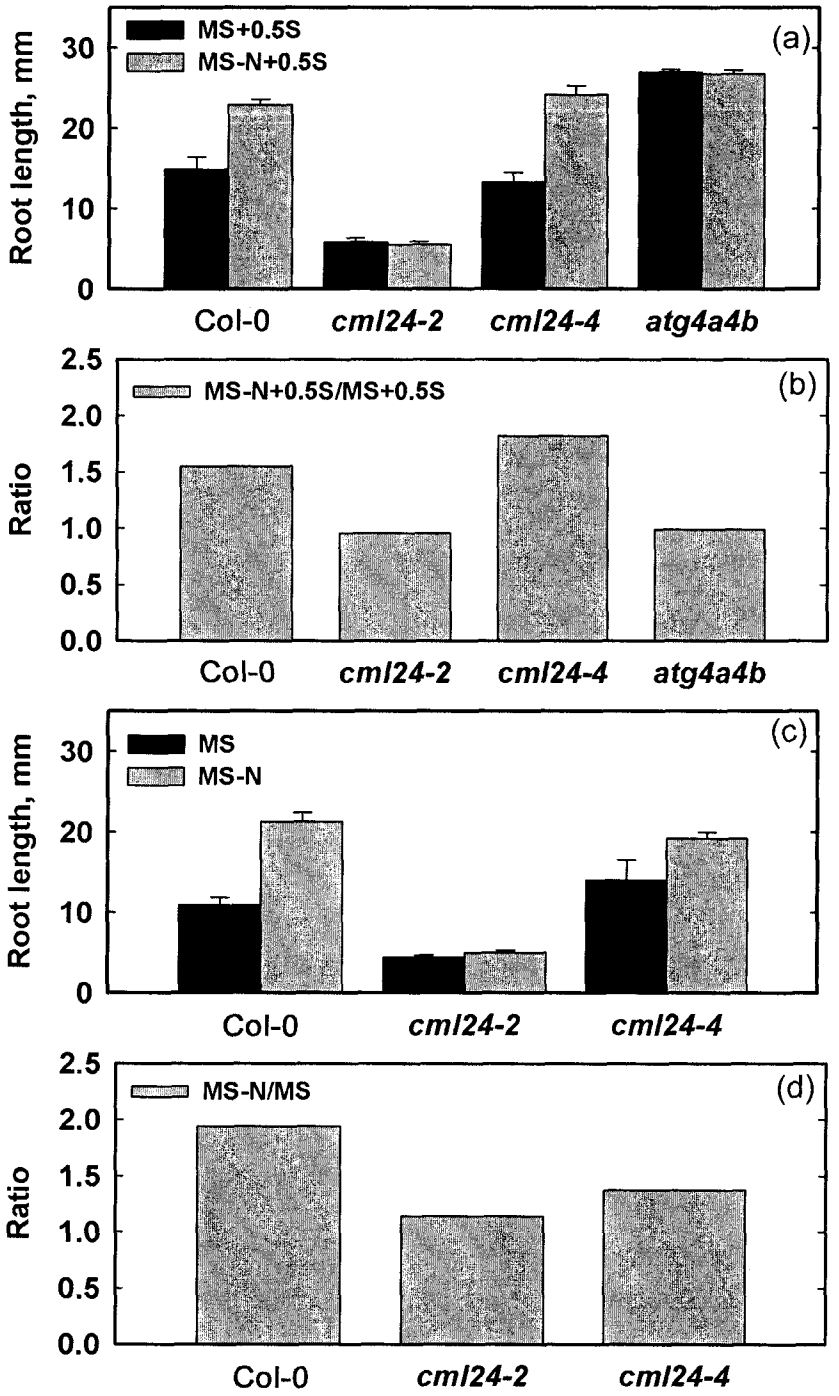

Fig 6.16 *cml24* and *atg4a4b* mutants have abnormal root growth in response to nitrogen and carbon availability media. Root length was measured for 5-day-old wild type (Col-0), *cml24-2*, *cml24-4*, and *atg4a4b* seedlings transferred to rich (MS) or nitrogen depleted (MS-N) media with (a) (b) or without (c) (d) 0.5% sucrose for three days. Error bars represent standard error, n≥12.

ratios of root length under different conditions were dependent on sucrose (Figure 16.16b and d). In the presence of sucrose, the root length ratios in *cml24-4* were slightly increased relative to wild type; whereas in the absence of sucrose *cml24-4* root ratios were significantly decreased relative to wild type. Thus, fixed carbon availability may also play a role in root elongation regulation.

These results suggest that *cml24-2* may have a defect in responding to nitrogen-depleted conditions, similarly to *atg4a4b*. However, *atg4a4b* in the Col-0 background has longer primary roots, not shorter, as published for Ws ecotype *atg4a4b* (Yoshimoto et al., 2004). The explanation for this ecotype difference is not yet clear. *cml24-4* may also fail to respond to nitrogen-limited conditions in the absence of sucrose. Overall, the role of autophagy and CML24 in root elongation regulation remains to be fully elucidated.

6.5 Conclusion

Autophagy has been implicated in several physiological processes, including survivability with limited nutrients and floral and embryonic development (Bassham et al., 2006; Chen et al., 2009a; Chung et al., 2009; Deprost et al., 2005; Fujiki et al., 2007; Harrison-Lowe and Olsen, 2008; Menand et al., 2004). Although plants and animals share highly conserved *ATG4* and *ATG8* gene families, the activity regulation of these proteins in plants is not yet clear. By studying the interaction partners of these autophagy proteins, we may reveal regulation mechanisms.

I confirmed a direct physical interaction between CML24 and ATG4b *in vitro*. This interaction is independent of Ca^{2+}. Plant ATG4 proteins do not have the conserved Cys redox sensor; instead a predicted plant specific CaM-binding domain was identified and, based on evolutionary trace computation, is predicted to be functionally important.

I performed *in vitro* activity assays with recombinant GST-ATG4b, His-ATG8e-HA, and CML24. The recombinant GST-ATG4b is able to modify the carboxyl-terminus of His-ATG8e-HA, and this activity may be elevated in presence of CML24. Apo-CML24 may enhance GST-ATG4b *in vitro* activity more than Ca^{2+}-bound CML24. ATG4-dependent cleavage of His-ATG8e-HA *in vitro* can detected in crude plant extracts. The *cml24-2* and *cml24-4* crude extracts have reduced His-ATG8e-HA cleavage activity levels upon shift to darkness, relative to that of Col-0. One possibility is that CML24 may be required to regulate ATG4 activity in response to change in light conditions. To further investigate this possible CML24 regulation of ATG4 activity, crude extract ATG4 activity levels will be assessed in plants harvested at multiple time points under distinct carbon- or nitrogen-limited conditions.

Distinct assays to evaluate autophagosome formation and autophagy progression were attempted to try to shed light on potential differences between the *cml24* mutants and wild type. Interpretation is complicated by the fact that different root regions show distinct responses and the kinetics of induced changes vary among genotypes. However, my hypothesis based on data obtained to date is that CML24 can affect autophagosome formation and accumulation and autophagy progression. Specifically, the *cml24-2* mutation leads increased punctate MDC and GFP-ATG8 fluorescence in root tips under basal conditions, consistent with enhanced autophagy in *cml24-2* root tips relative to wild type. Constitutive autophagy in *cml24-2* is also consistent with the elevated levels of GFP release from GFP-ATG8 in plants grown under nutrient rich conditions. However, in mutant root cells of seedlings subjected to nutrient limitation, *cml24-2* has fewer

autophagosome-like structures than wild type, consistent with the *cml24-2* mutation negatively affecting the ability to induce autophagy in response to nutrient limitation.

In mature root cells, the *cml24-4* mutation appears to enhance basal levels of autophagosome formation and accelerate autophagosome appearance in response to nutrient limitation relative to wild type.

Plants that either over or under accumulate CML24 have enhanced MDC-stained structures relative to wild type under basal conditions. Thus, alteration of either CML24 levels or CML24 functions, as a consequence of mutation, appear to affect the extent of autophagy.

I hypothesize that the effects on apparent autophagy levels in the *cml24* mutants are due to altered CML24 interaction with and activity regulation of ATG4. Additional ATG4 activity assays with crude extracts of wild type and mutant tissues will be necessary to clarity the effects of CML24 on ATG4 activity. Furthermore, examination of the ability of mutant cml24 isoforms to regulate ATG4 activity *in vitro* may help to elucidate the enzymatic basis of the *cml24* mutants.

To verify a genetic interaction between *CML24* and *ATG4*, it will be advantageous to characterize plants defective in both *CML24* and *ATG4*. If, for example, CML24 upregulates ATG4 activity, a *cml24/atg4* mutant should be more defective in autophagy than either single mutant, potentially approaching the phenotype of *atg4a4b*.

In summary, autophagy is a regulated cellular response that varies in magnitude depending upon cell type and growth conditions. ATG4 is a critical player that can both

promote and inhibit autophagy progression through its modifications of ATG8. CML24 interacts with and may regulate ATG4 activity, and thus autophagosome formation.

Chapter 7: Discussion and Future Perspectives

Fluctuations in cellular calcium (Ca^{2+}) are implicated in regulating plant growth, development, and responses to environmental stimuli (Reed et al., 1993; Yang and Poovaiah, 2003). The Arabidopsis genome encodes a large *CaM/CML* family, and this work sheds light on one Ca^{2+} sensor, CML24, and its potential functions in diverse aspects of plant physiology, including the regulation of the transition to flowering, nitric oxide (NO) accumulation, and autophagy. CML24 can interact with ATG4b, which may regulate ATG4 activity and autophagy (Chapter 5 and 6). ATG4b does not appear to interact with CaM and the *cml24* mutants have phenotypes even in the background of the remaining CaMs and CMLs. This suggests that individual CMLs may have specific and distinct functions. However, CML24 and CML23 do share some overlapping functions, both in NO accumulation and flowering regulation (Chapter 3). *CML24* regulates NO levels and may act downstream of or in parallel to *NOA1*, which encodes a mitochondrial and/or chloroplast protein (Chapter 4). CML24 binds to Ca^{2+} and may form a disulfide. These characteristics suggest that CML24 may act as both a Ca^{2+} and redox sensor (Chapter 5).

I provide the model illustrated in Figure 7.1 to propose a summary scheme that includes the diverse aspects of CML24 analysis. I hypothesize that CML24 acts as a Ca^{2+} and redox sensor and is involved in ROS and Ca^{2+} homeostasis (Figure 7.1). High and local accumulation of ROS and/or Ca^{2+} may be induced by starvation or different kinds of stress (Delledonne et al., 1998; Zeidler et al., 2004). Mitochondria and/or chloroplasts are a source of ROS (Maxwell et al., 1999) and Ca^{2+} (Logan and Knight, 2003)

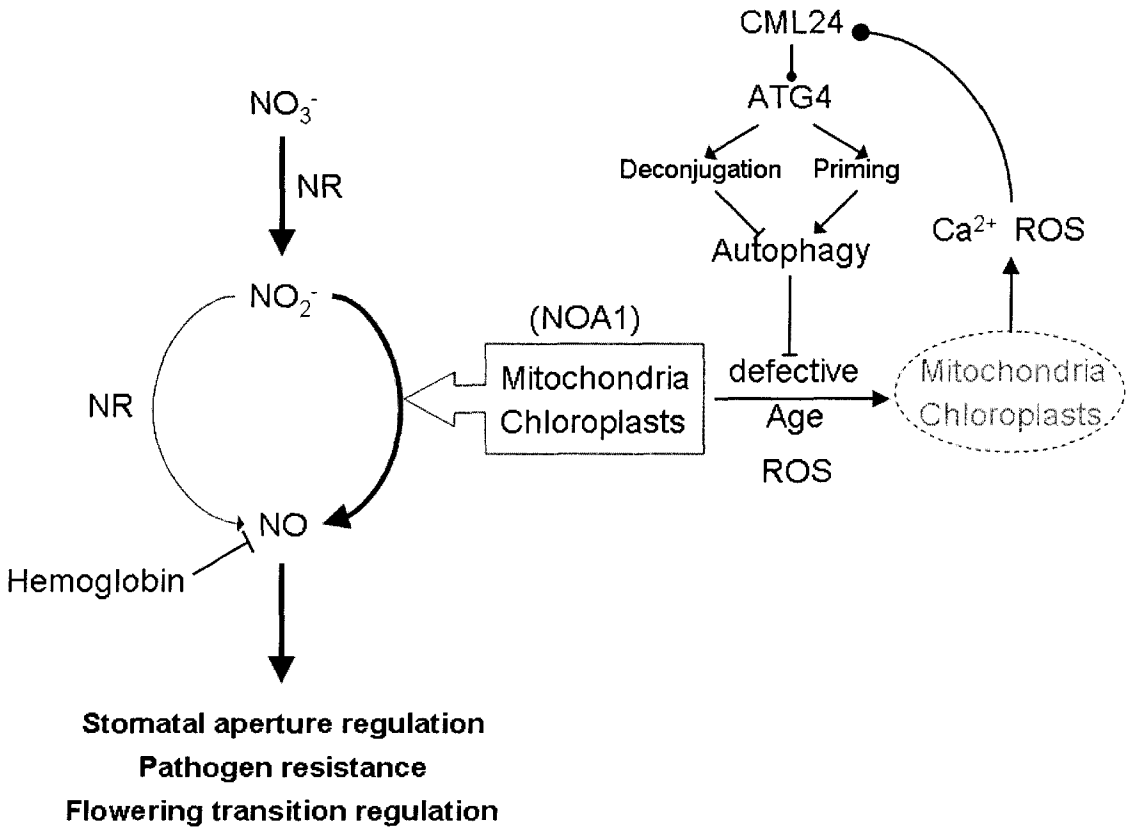

Fig 7.1 A proposed model for the function of CML24. CML24 regulates autophagy by directly interacting with ATG4b. Upon aging or stress conditions, mitochondria and/or chloroplasts may be attacked by ROS. Proper autophagy function autophagy is required for removing malfunction mitochondria or chloroplasts, which may release Ca^{2+} or ROS. CML24 can use EF-hands or disulfides to sense Ca^{2+} or ROS, which may impact ATG4 interaction. Autophagosome formation requires proper ATG4 activities in priming and/or lipid deconjugation of ATG8. Without proper autophagy regulation by CML24, mitochondria or chloroplasts, which contain NOA1, may also produce NO from NO_2^-. NO can also be produced by reduction of NO_2^- by nitrate reductase (NR) under hypoxia conditions. NO can be degraded by hemoglobin.

production in Arabidopsis. CML24 may detect increases in Ca^{2+} and ROS through binding Ca^{2+} or oxidation-induced Cys thiol modification, and these changes would lead to activated CML24. CML24 directly interacts with ATG4. Activated CML24 may differentially affect ATG4 activities in priming and/or lipid deconjugation of ATG8. ATG4 activity is necessary to prime ATG8, but too much ATG4 activity may block mature autophagosome formation. Thus, turning down ATG4 activity may be necessary for robust autophagy. Defective mitochondria and chloroplasts may release too much ROS or Ca^{2+}. Mitochondria and chloroplasts are also reported sources of NO production from nitrite in plants (Jasid et al., 2006; Planchet et al., 2005) (Figure 7.1). Thus, stress signals may trigger CML24 effects on ATG4, perhaps inhibition of deconjugation activity, enabling autophagy induction. Nitrate reductase is required to produce nitrite, and nitrite is likely to be the major source for NO production in plants. Nitrate reduction can also convert nitrite to NO under hypoxia conditions, which may contribute a small portion of NO accumulation (Figure 7.1). NO can trigger several downstream cell responses, like stomatal aperture regulation, pathogen resistance and flowering time transition regulation (Garcia-Mata et al., 2003; He et al., 2004b; Li et al., 2009; Ma et al., 2008).

In this study, CML24 has been shown to interact with ATG4b by yeast two-hybrid and GST pull-down. To gain more insight to CML24 functions and autophagy regulation, several future experiments are proposed.

There are two ATG4 isoforms in Arabidopsis genome, ATG4a and ATG4b. To test whether CML24 also interacts with ATG4a, GST-ATG4a protein will be generated and purified for GST pull-down assay with CML24. Additionally, to address CML24 and

ATG4a/4b *in vivo* interaction, CML24- and ATG4b-tag (e.g. myc, HA, FLAG and GST) transgenic plants will be generated and co-immunoprecipitation with anti-tag antibodies will be performed. Moreover, additional CML24 interaction partners could also be pulled down since many CaMs/CMLs may have multiple targets (Popescu et al., 2007a). ATG4 is known to interact with ATG8 (Fujioka et al., 2008; Fujita et al., 2008; Satoo et al., 2009; Tanida et al., 2004b; Yoshimoto et al., 2004). Preliminary GST pull-down assay did not show CML24 and ATG8e-ATG4b interaction (data not shown). This result may be because ATG4b may have higher binding affinity for ATG8e than CML24. To investigate whether the second functional region on ATG4b predicted by Evolution Trace analysis is important for ATG4b-CML24 interaction, amino acid substituted ATG4b mutants (Q184, R190, L191, G192, R193) proteins will be expressed and verified the interaction with CML24 assayed. Co-crystallization of CML24-ATG4b proteins and determination of structure could also shed light on the structure bases for ATG4 activity regulation.

Plant ATG4s lack the analogous Cys required for redox regulation of animal ATG4s (Scherz-Shouval et al. 2007). One possibility is that CML24, with the ability to form at least one disulfide between two of the four Cys residues, may act as a redox sensor and be responsible for plant ATG4 activity regulation. To assess whether the Cys residues on CML24 may act in redox sensing, CML24 protein pre-treated with H_2O_2 and DTT will be analyzed for disulfide bond formation with mass spectrometry. CML24 Cys mutants (C11, C126, C131 and C145) will also be generated and the disulfide bonds will be expected to be lost based on the mass spectrum. Additional CML24-ATG4 pull-down

assays will be performed in the present of H_2O_2 or DTT to imitate different redox environments.

The two distinct activities of ATG4 are priming ATG8 and releasing ATG8 from PE (Yoshimoto et al., 2004). Although the recombinant GST-ATG4b revealed the cysteine protease activity to cleave carboxyl-terminus of His-ATG8e-HA *in vitro*, the activity was low relative to previous report with animal ATG4s, which had full cleavage of ATG8 within one hour incubation (Fujioka et al., 2008; Scherz-Shouval et al., 2007; Tanida et al., 2004b). To overcome the low ATG4 activity, the GST tag will be removed from the recombinant GST-ATG4b with thrombin. Alternatively, another tagged fusion of ATG4b protein will be generated and analyzed for *in vitro* activity. ATG4 activity could also be analyzed with the tissue extract and incubated with exogenous His-ATG8e-HA. To analyze whether ATG4 activity could be regulated through CML24, wild-type, *cml24-2*, *cml24-4*, *atg4a4b*, and *cml24/atg4a4b* mutant tissues will be harvested at different conditions, e.g. darkness or light, nitrogen starvation, and tissue extract will be incubated with His-ATG8e-HA. The endogenous ATG4 activity will be determined based on the accumulation of processed His-ATG8e. Endogenous ATG8 protein and transcript levels will also be analyzed with western blots and Q-PCR, respectively.

CML24 may have different regulation on the two distinct activities of ATG4. Two of Arabidopsis ATG8s, ATG8h and ATG8i, which do not have the extended carboxyl-terminus after Gly, may only require ATG4 for releasing from the PE. *atg8h* and *atg8i* mutants will be identified and crossed with *cml24* and *atg4a4b* to analyze whether CML24 regulates autophagy by affecting the priming activity of ATG4. In

addition, ATG8-PE will be engineered to verify ATG4 deconjugation activity, which potentially is also regulated by CML24.

Proper ATG4 activity regulation is critical for autophagosome closure (Fujita et al., 2008). To monitor autophagosome number and autophagic flux, GFP-ATG8 has been wildely used (Contento et al., 2005; Mizushima et al., 2010; Slavikova et al., 2008). *cml24-2/GFP-ATG8a* and *cml24-4/GFP-ATG8a* transgenics revealed different punctate and diffused GFP fluorescence relative to Col-0/*GFP-ATG8a*, which may correlate to defective CML24 functions. However, some potential pitfalls may occur with the GFP-ATG8a transgenics driven by a constitutive promoter. An endogenous *ATG8a* promoter will be fused to *GFP-ATG8a* and transferred to *cml24* and *cml24/atg4a4b* mutants, which could prevent ectopic GFP fluorescence. To confirm the fluorescence structures observed by MDC and GFP, transmission electron microscopy (TEM) will also performed to detect the morphology of autophagosome double membranes.

In addition, CML24 may also interact with a protein (At1g72090) function in iron-sulfur cluster binding from yeast two-hybrid analysis. The interaction of CML24 and At1g72090 still needs to be verified and the cellular functions of At1g72090 remain unclear.

Bibliography

Aitken, A. (1996). 14-3-3 and its possible role in co-ordinating multiple signalling pathways. Trends Cell Biol *6*, 341-347.

Alderton, W.K., Cooper, C.E., and Knowles, R.G. (2001). Nitric oxide synthases: structure, function and inhibition. Biochem J *357*, 593-615.

Alonso, J.M., Stepanova, A.N., Leisse, T.J., Kim, C.J., Chen, H., Shinn, P., Stevenson, D.K., Zimmerman, J., Barajas, P., Cheuk, R., *et al.* (2003). Genome-wide insertional mutagenesis of Arabidopsis thaliana. Science *301*, 653-657.

Arnaud, N., Murgia, I., Boucherez, J., Briat, J.F., Cellier, F., and Gaymard, F. (2006). An iron-induced nitric oxide burst precedes ubiquitin-dependent protein degradation for Arabidopsis AtFer1 ferritin gene expression. J Biol Chem *281*, 23579-23588.

Bampton, E.T., Goemans, C.G., Niranjan, D., Mizushima, N., and Tolkovsky, A.M. (2005). The dynamics of autophagy visualized in live cells: from autophagosome formation to fusion with endo/lysosomes. Autophagy *1*, 23-36.

Barroso, J.B., Corpas, F.J., Carreras, A., Sandalio, L.M., Valderrama, R., Palma, J.M., Lupianez, J.A., and del Rio, L.A. (1999). Localization of nitric-oxide synthase in plant peroxisomes. J Biol Chem *274*, 36729-36733.

Bassham, D.C., Laporte, M., Marty, F., Moriyasu, Y., Ohsumi, Y., Olsen, L.J., and Yoshimoto, K. (2006). Autophagy in development and stress responses of plants. Autophagy *2*, 2-11.

Baum, G., Long, J.C., Jenkins, G.I., and Trewavas, A.J. (1999). Stimulation of the blue light phototropic receptor NPH1 causes a transient increase in cytosolic Ca2+. Proc Natl Acad Sci USA *96*, 13554-13559.

Baxter, I., Ouzzani, M., Orcun, S., Kennedy, B., Jandhyala, S.S., and Salt, D.E. (2007). Purdue ionomics information management system. An integrated functional genomics platform. Plant Physiol *143*, 600-611.

Benschop, J.J., Mohammed, S., O'Flaherty, M., Heck, A.J., Slijper, M., and Menke, F.L. (2007). Quantitative phosphoproteomics of early elicitor signaling in Arabidopsis. Mol Cell Proteomics *6*, 1198-1214.

Biederbick, A., Kern, H., and Elsasser, H. (1995). Monodansylcadaverine (MDC) is a specific in vivo marker for autophagic vacuoles. Eur J Cell Biol *66*, 3-14.

Bootman, M.D., and Berridge, M.J. (1995). The elemental principles of calcium signaling. Cell *83*, 675-678.

Braam, J. (1992). Regulated expression of the calmodulin-related TCH genes in cultured Arabidopsis cells: induction by calcium and heat shock. Proc Natl Acad Sci U S A *89*, 3213-3216.

Braam, J., and Davis, R.W. (1990). Rain-, wind-, and touch-induced expression of calmodulin and calmodulin-related genes in Arabidopsis. Cell *60*, 357-364.

Bright, J., Desikan, R., Hancock, J.T., Weir, I.S., and Neill, S.J. (2006). ABA-induced NO generation and stomatal closure in Arabidopsis are dependent on H2O2 synthesis. Plant J *45*, 113-122.

Chae, Y.K., Im, H., Zhao, Q., Doelling, J.H., Vierstra, R.D., and Markley, J.L. (2004). Prevention of aggregation after refolding by balanced stabilization-destabilization: production of the Arabidopsis thaliana protein APG8a (At4g21980) for NMR structure determination. Protein Expr Purif *34*, 280-283.

Chen, C.N., Chen, H.R., Yeh, S.Y., Vittore, G., and Ho, T.H. (2009a). Autophagy Is Enhanced and Floral Development Is Impaired in AtHVA22d RNA Interference Arabidopsis. Plant Physiol *149*, 1679-1689.

Chen, Y., Azad, M.B., and Gibson, S.B. (2009b). Superoxide is the major reactive oxygen species regulating autophagy. Cell Death Differ *16*, 1040-1052.

Chiasson, D., Ekengren, S.K., Martin, G.B., Dobney, S.L., and Snedden, W.A. (2005). Calmodulin-like proteins from Arabidopsis and tomato are involved in host defense against Pseudomonas syringae pv. tomato. Plant Mol Biol *58*, 887-897.

Chung, T., Suttangkakul, A., and Vierstra, R.D. (2009). The ATG autophagic conjugation system in maize: ATG transcripts and abundance of the ATG8-lipid adduct are regulated by development and nutrient availability. Plant Physiol *149*, 220-234.

Clapham, D.E. (1995). Calcium signaling. Cell *80*, 259-268.

Contento, A.L., Xiong, Y., and Bassham, D.C. (2005). Visualization of autophagy in Arabidopsis using the fluorescent dye monodansylcadaverine and a GFP-AtATG8e fusion protein. Plant J *42*, 598-608.

Corpas, F.J., Barroso, J.B., Carreras, A., Quiros, M., Leon, A.M., Romero-Puertas, M.C., Esteban, F.J., Valderrama, R., Palma, J.M., Sandalio, L.M., *et al.* (2004). Cellular and subcellular localization of endogenous nitric oxide in young and senescent pea plants. Plant Physiol *136*, 2722-2733.

Corpas, F.J., Hayashi, M., Mano, S., Nishimura, M., and Barroso, J.B. (2009a). Peroxisomes are required for in vivo nitric oxide (NO) accumulation in the cytosol following salinity stress of Arabidopsis plants. Plant Physiol.

Corpas, F.J., Palma, J.M., del Rio, L.A., and Barroso, J.B. (2009b). Evidence supporting the existence of L-arginine-dependent nitric oxide synthase activity in plants. New Phytol *184*, 9-14.

Crawford, N.M., Galli, M., Tischner, R., Heimer, Y.M., Okamoto, M., and Mack, A. (2006). Response to Zemojtel et al: Plant nitric oxide synthase: back to square one. Trends in Plant Science *11*, 526.

Cyert, M.S. (2001). Genetic analysis of calmodulin and its targets in Saccharomyces cerevisiae. Annu Rev Genet *35*, 647-672.

Day, I.S., Reddy, V.S., Shad Ali, G., and Reddy, A.S. (2002). Analysis of EF-hand-containing proteins in Arabidopsis. Genome Biol *3*, RESEARCH0056.

del Rio, L.A., Corpas, F.J., and Barroso, J.B. (2004). Nitric oxide and nitric oxide synthase activity in plants. Phytochemistry *65*, 783-792.

Delk, N.A. (2006). The Regulation and Function of CML23 and CML24: Arabidopsis thaliana Genes Encoding Ca2+-Binding Proteins Implicated in Abscisic Acid Response, Floral Transition, and Ion Homeostasis. In Biochemistry and Cell Biology (Houston, Rice University).

Delk, N.A., Johnson, K.A., Chowdhury, N.I., and Braam, J. (2005). CML24, regulated in expression by diverse stimuli, encodes a potential Ca2+ sensor that functions in responses to abscisic acid, daylength, and ion stress. Plant Physiol *139*, 240-253.

Delledonne, M., Xia, Y., Dixon, R.A., and Lamb, C. (1998). Nitric oxide functions as a signal in plant disease resistance. Nature *394*, 585-588.

Deprost, D., Truong, H.N., Robaglia, C., and Meyer, C. (2005). An Arabidopsis homolog of RAPTOR/KOG1 is essential for early embryo development. Biochem Biophys Res Commun *326*, 844-850.

Desikan, R., Cheung, M.K., Bright, J., Henson, D., Hancock, J.T., and Neill, S.J. (2004). ABA, hydrogen peroxide and nitric oxide signalling in stomatal guard cells. J Exp Bot *55*, 205-212.

Desikan, R., Griffiths, R., Hancock, J., and Neill, S. (2002). A new role for an old enzyme: nitrate reductase-mediated nitric oxide generation is required for abscisic acid-induced stomatal closure in Arabidopsis thaliana. Proc Natl Acad Sci U S A *99*, 16314-16318.

Dobney, S., Chiasson, D., Lam, P., Smith, S.P., and Snedden, W.A. (2009). The calmodulin-related calcium sensor CML42 plays a role in trichome branching. J Biol Chem *284*, 31647-31657.

Dodd, A.N., Love, J., and Webb, A.A. (2005). The plant clock shows its metal: circadian regulation of cytosolic free Ca(2+). Trends Plant Sci *10*, 15-21.

Doelling, J.H., Walker, J.M., Friedman, E.M., Thompson, A.R., and Vierstra, R.D. (2002). The APG8/12-activating enzyme APG7 is required for proper nutrient recycling and senescence in Arabidopsis thaliana. J Biol Chem *277*, 33105-33114.

Flückiger, R., De Caroli, M., Piro, G., Dalessandro, G., Neuhaus, J.M., and Di Sansebastiano, G.P. (2003). Vacuolar system distribution in Arabidopsis tissues, visualized using GFP fusion proteins. J Exp Bot *54*, 1577-1584.

Flores-Pérez, U., Sauret-Gueto, S., Gas, E., Jarvis, P., and Rodriguez-Concepcion, M. (2008). A mutant impaired in the production of plastome-encoded proteins uncovers a mechanism for the homeostasis of isoprenoid biosynthetic enzymes in Arabidopsis plastids. Plant Cell *20*, 1303-1315.

Fujiki, Y., Yoshimoto, K., and Ohsumi, Y. (2007). An Arabidopsis homolog of yeast ATG6/VPS30 is essential for pollen germination. Plant Physiol *143*, 1132-1139.

Fujioka, Y., Noda, N.N., Fujii, K., Yoshimoto, K., Ohsumi, Y., and Inagaki, F. (2008). In vitro reconstitution of plant Atg8 and Atg12 conjugation systems essential for autophagy. J Biol Chem *283*, 1921-1928.

Fujita, N., Hayashi-Nishino, M., Fukumoto, H., Omori, H., Yamamoto, A., Noda, T., and Yoshimori, T. (2008). An Atg4B mutant hampers the lipidation of LC3 paralogues and causes defects in autophagosome closure. Mol Biol Cell *19*, 4651-4659.

Gao, X.D., Wang, J., Keppler-Ross, S., and Dean, N. (2005). ERS1 encodes a functional homologue of the human lysosomal cystine transporter. FEBS J *272*, 2497-2511.

Garcia-Mata, C., Gay, R., Sokolovski, S., Hills, A., Lamattina, L., and Blatt, M.R. (2003). Nitric oxide regulates K+ and Cl- channels in guard cells through a subset of abscisic acid-evoked signaling pathways. Proc Natl Acad Sci U S A *100*, 11116-11121.

Gilroy, S. (1996). Signal Transduction in Barley Aleurone Protoplasts Is Calcium Dependent and Independent. Plant Cell *8*, 2193-2209.

Guo, F.Q., and Crawford, N.M. (2005). Arabidopsis nitric oxide synthase1 is targeted to mitochondria and protects against oxidative damage and dark-induced senescence. Plant Cell *17*, 3436-3450.

Guo, F.Q., Okamoto, M., and Crawford, N.M. (2003). Identification of a plant nitric oxide synthase gene involved in hormonal signaling. Science *302*, 100-103.

Gupta, K.J., Stoimenova, M., and Kaiser, W.M. (2005). In higher plants, only root mitochondria, but not leaf mitochondria reduce nitrite to NO, in vitro and in situ. J Exp Bot *56*, 2601-2609.

Harrison-Lowe, N.J., and Olsen, L.J. (2008). Autophagy Protein 6 (ATG6) is Required for Pollen Germination in Arabidopsis thaliana. Autophagy *4*.

Harrison, S.J., Mott, E.K., Parsley, K., Aspinall, S., Gray, J.C., and Cottage, A. (2006). A rapid and robust method of identifying transformed Arabidopsis thaliana seedlings following floral dip transformation. Plant Methods *2*, 19.

Haughn, G.W., and Somerville, C. (1986). Sulfonylurea-resistant mutants of Arabidopsis thaliana. Mol Gen Genet *204*, 430-434.

He, C., and Klionsky, D.J. (2009). Regulation mechanisms and signaling pathways of autophagy. Annu Rev Genet *43*, 67-93.

He, Y., Doyle, M.R., and Amasino, R.M. (2004a). PAF1-complex-mediated histone methylation of FLOWERING LOCUS C chromatin is required for the vernalization-responsive, winter-annual habit in Arabidopsis. Genes Dev *18*, 2774-2784.

He, Y., Michaels, S.D., and Amasino, R.M. (2003). Regulation of flowering time by histone acetylation in Arabidopsis. Science *302*, 1751-1754.

He, Y., Tang, R.H., Hao, Y., Stevens, R.D., Cook, C.W., Ahn, S.M., Jing, L., Yang, Z., Chen, L., Guo, F., *et al.* (2004b). Nitric oxide represses the Arabidopsis floral transition. Science *305*, 1968-1971.

Heazlewood, J.L., Verboom, R.E., Tonti-Filippini, J., Small, I., and Millar, A.H. (2007). SUBA: the Arabidopsis Subcellular Database. Nucleic Acids Res *35*, D213-218.

Hebelstrup, K.H., and Østergaard-Jensen, E. (2008). Expression of NO scavenging hemoglobin is involved in the timing of bolting in Arabidopsis thaliana. Planta *227*, 917-927.

Huang, S., Kerschbaum, H.H., Engel, E., and Hermann, A. (1997). Biochemical Characterization and Histochemical Localization of Nitric Oxide Synthase in the Nervous System of the Snail, Helix pomatia. Journal of Neurochemistry *69*, 2516-2528.

Imaizumi, T., Tran, H.G., Swartz, T.E., Briggs, W.R., and Kay, S.A. (2003). FKF1 is essential for photoperiodic-specific light signalling in Arabidopsis. Nature *426*, 302-306.

Inoue, Y., Suzuki, T., Hattori, M., Yoshimoto, K., Ohsumi, Y., and Moriyasu, Y. (2006). AtATG genes, homologs of yeast autophagy genes, are involved in constitutive autophagy in Arabidopsis root tip cells. Plant Cell Physiol *47*, 1641-1652.

Jack, T. (2004). Molecular and genetic mechanisms of floral control. Plant Cell *16 Suppl*, S1-17.

Jasid, S., Simontacchi, M., Bartoli, C.G., and Puntarulo, S. (2006). Chloroplasts as a nitric oxide cellular source. Effect of reactive nitrogen species on chloroplastic lipids and proteins. Plant Physiol *142*, 1246-1255.

Johanson, U., West, J., Lister, C., Michaels, S., Amasino, R., and Dean, C. (2000). Molecular analysis of FRIGIDA, a major determinant of natural variation in Arabidopsis flowering time. Science *290*, 344-347.

Joshi, V., Laubengayer, K.M., Schauer, N., Fernie, A.R., and Jander, G. (2006). Two Arabidopsis threonine aldolases are nonredundant and compete with threonine deaminase for a common substrate pool. Plant Cell *18*, 3564-3575.

Kaiser, W., Weiner, H., and Huber, S.C. (1999). Nitrate reductase in higher plants: A case study for transduction of environmental stimuli into control of catalytic activity. PHYSIOLOGIA PLANTARUM *105*, 385-390.

Kaiser, W.M., Kandlbinder, A., Stoimenova, M., and Glaab, J. (2000). Discrepancy between nitrate reduction rates in intact leaves and nitrate reductase activity in leaf extracts: what limits nitrate reduction in situ? Planta *210*, 801-807.

Kardailsky, I., Shukla, V.K., Ahn, J.H., Dagenais, N., Christensen, S.K., Nguyen, J.T., Chory, J., Harrison, M.J., and Weigel, D. (1999). Activation tagging of the floral inducer FT. Science *286*, 1962-1965.

Khan, A.R., Johnson, K.A., Braam, J., and James, M.N. (1997). Comparative modeling of the three-dimensional structure of the calmodulin-related TCH2 protein from Arabidopsis. Proteins *27*, 144-153.

Kim, E., Goraksha-Hicks, P., Li, L., Neufeld, T.P., and Guan, K.L. (2008). Regulation of TORC1 by Rag GTPases in nutrient response. Nat Cell Biol *10*, 935-945.

Kim, I., Rodriguez-Enriquez, S., and Lemasters, J.J. (2007). Selective degradation of mitochondria by mitophagy. Arch Biochem Biophys *462*, 245-253.

Kim, J., Lee, M., Chalam, R., Martin, M.N., Leustek, T., and Boerjan, W. (2002). Constitutive overexpression of cystathionine gamma-synthase in Arabidopsis leads to accumulation of soluble methionine and S-methylmethionine. Plant Physiol *128*, 95-107.

Kim, M.C., Chung, W.S., Yun, D.J., and Cho, M.J. (2009). Calcium and calmodulin-mediated regulation of gene expression in plants. Mol Plant *2*, 13-21.

Kirisako, T., Ichimura, Y., Okada, H., Kabeya, Y., Mizushima, N., Yoshimori, T., Ohsumi, M., Takao, T., Noda, T., and Ohsumi, Y. (2000a). The Reversible Modification Regulates the Membrane-Binding State of Apg8/Aut7 Essential for Autophagy and the Cytoplasm to Vacuole Targeting Pathway. J Cell Biol *151*, 263-276.

Kirisako, T., Ichimura, Y., Okada, H., Kabeya, Y., Mizushima, N., Yoshimori, T., Ohsumi, M., Takao, T., Noda, T., and Ohsumi, Y. (2000b). The reversible modification regulates the membrane-binding state of Apg8/Aut7 essential for autophagy and the cytoplasm to vacuole targeting pathway. J Cell Biol *151*, 263-276.

Kirkin, V., McEwan, D.G., Novak, I., and Dikic, I. (2009). A role for ubiquitin in selective autophagy. Mol Cell *34*, 259-269.

Klimyuk, V.I., Carroll, B.J., Thomas, C.M., and Jones, J.D. (1993). Alkali treatment for rapid preparation of plant material for reliable PCR analysis. Plant J *3*, 493-494.

Kobayashi, Y., Kaya, H., Goto, K., Iwabuchi, M., and Araki, T. (1999). A pair of related genes with antagonistic roles in mediating flowering signals. Science *286*, 1960-1962.

Kolbert, Z., Bartha, B., and Erdei, L. (2008). Exogenous auxin-induced NO synthesis is nitrate reductase-associated in Arabidopsis thaliana root primordia. J Plant Physiol *165*, 967-975.

Kolbert, Z., and Erdei, L. (2008). Involvement of nitrate reductase in auxin-induced NO synthesis. Plant Signal Behav *3*, 972-973.

Komatsu, M., Waguri, S., Chiba, T., Murata, S., Iwata, J., Tanida, I., Ueno, T., Koike, M., Uchiyama, Y., Kominami, E., *et al.* (2006). Loss of autophagy in the central nervous system causes neurodegeneration in mice. Nature *441*, 880-884.

Koornneef, M., Hanhart, C.J., and van der Veen, J.H. (1991). A genetic and physiological analysis of late flowering mutants in Arabidopsis thaliana. Mol Gen Genet *229*, 57-66.

López-Figueroa, M.O., Caamaño, C., Morano, M.I., Rønn, L.C., Akil, H., and Watson, S.J. (2000). Direct evidence of nitric oxide presence within mitochondria. Biochem Biophys Res Commun *272*, 129-133.

Laetsch, W.M., and Briggs, W.R. (1963). Correlative Inhibition and the Primary Organs of Marsilea vestita Botanical Gazette *124*, 317-324.

Lamotte, O., Courtois, C., Barnavon, L., Pugin, A., and Wendehenne, D. (2005). Nitric oxide in plants: the biosynthesis and cell signalling properties of a fascinating molecule. Planta *221*, 1-4.

Larkin, M.A., Blackshields, G., Brown, N.P., Chenna, R., McGettigan, P.A., McWilliam, H., Valentin, F., Wallace, I.M., Wilm, A., Lopez, R., *et al.* (2007). Clustal W and Clustal X version 2.0. Bioinformatics *23*, 2947-2948.

Lee, M., Martin, M.N., Hudson, A.O., Lee, J., Muhitch, M.J., and Leustek, T. (2005). Methionine and threonine synthesis are limited by homoserine availability and not the activity of homoserine kinase in Arabidopsis thaliana. Plant J *41*, 685-696.

Li, J.H., Liu, Y.Q., Lu, P., Lin, H.F., Bai, Y., Wang, X.C., and Chen, Y.L. (2009). A signaling pathway linking nitric oxide production to heterotrimeric G protein and hydrogen peroxide regulates extracellular calmodulin induction of stomatal closure in Arabidopsis. Plant Physiol *150*, 114-124.

Liang, L., Flury, S., Kalck, V., Hohn, B., and Molinier, J. (2006). CENTRIN2 interacts with the Arabidopsis homolog of the human XPC protein (AtRAD4) and contributes to efficient synthesis-dependent repair of bulky DNA lesions. Plant Mol Biol *61*, 345-356.

Lillo, C., Meyer, C., Lea, U.S., Provan, F., and Oltedal, S. (2004). Mechanism and importance of post-translational regulation of nitrate reductase. J Exp Bot *55*, 1275-1282.

Linkohr, B.I., Williamson, L.C., Fitter, A.H., and Leyser, H.M. (2002). Nitrate and phosphate availability and distribution have different effects on root system architecture of Arabidopsis. Plant J *29*, 751-760.

Logan, D.C., and Knight, M.R. (2003). Mitochondrial and cytosolic calcium dynamics are differentially regulated in plants. Plant Physiol *133*, 21-24.

Love, J., Dodd, A.N., and Webb, A.A. (2004). Circadian and diurnal calcium oscillations encode photoperiodic information in Arabidopsis. Plant Cell *16*, 956-966.

Ma, W., Smigel, A., Tsai, Y.C., Braam, J., and Berkowitz, G.A. (2008). Innate immunity signaling: cytosolic Ca2+ elevation is linked to downstream nitric oxide generation through the action of calmodulin or a calmodulin-like protein. Plant Physiol *148*, 818-828.

Madabushi, S., Yao, H., Marsh, M., Kristensen, D.M., Philippi, A., Sowa, M.E., and Lichtarge, O. (2002). Structural clusters of evolutionary trace residues are statistically significant and common in proteins. J Mol Biol *316*, 139-154.

Matsuoka, K. (2008). Chimeric fluorescent fusion proteins to monitor autophagy in plants. Methods Enzymol *451*, 541-555.

Maxwell, D.P., Wang, Y., and McIntosh, L. (1999). The alternative oxidase lowers mitochondrial reactive oxygen production in plant cells. Proc Natl Acad Sci U S A *96*, 8271-8276.

McCormack, E., and Braam, J. (2003). Calmodulins and related potential calcium sensors of Arabidopsis. New Phytol *159*, 585-598.

McCormack, E., Tsai, Y.C., and Braam, J. (2005). Handling calcium signaling: Arabidopsis CaMs and CMLs. Trends Plant Sci *10*, 383-389.

Menand, B., Desnos, T., Nussaume, L., Berger, F., Bouchez, D., Meyer, C., and Robaglia, C. (2002). Expression and disruption of the Arabidopsis TOR (target of rapamycin) gene. Proc Natl Acad Sci U S A *99*, 6422-6427.

Menand, B., Meyer, C., and Robaglia, C. (2004). Plant growth and the TOR pathway. Curr Top Microbiol Immunol *279*, 97-113.

Meyer, C., Lea, U.S., Provan, F., Kaiser, W.M., and Lillo, C. (2005). Is nitrate reductase a major player in the plant NO (nitric oxide) game? Photosynth Res *83*, 181-189.

Michael, T.P., Mockler, T.C., Breton, G., McEntee, C., Byer, A., Trout, J.D., Hazen, S.P., Shen, R., Priest, H.D., Sullivan, C.M., *et al.* (2008). Network discovery pipeline elucidates conserved time-of-day-specific cis-regulatory modules. PLoS Genet *4*, e14.

Mizoguchi, T., Wright, L., Fujiwara, S., Cremer, F., Lee, K., Onouchi, H., Mouradov, A., Fowler, S., Kamada, H., Putterill, J., *et al.* (2005). Distinct roles of GIGANTEA in promoting flowering and regulating circadian rhythms in Arabidopsis. Plant Cell *17*, 2255-2270.

Mizushima, N., Yoshimori, T., and Levine, B. (2010). Methods in mammalian autophagy research. Cell *140*, 313-326.

Molinier, J., Ramos, C., Fritsch, O., and Hohn, B. (2004). CENTRIN2 modulates homologous recombination and nucleotide excision repair in Arabidopsis. Plant Cell *16*, 1633-1643.

Moon, J., Suh, S.S., Lee, H., Choi, K.R., Hong, C.B., Paek, N.C., Kim, S.G., and Lee, I. (2003). The SOC1 MADS-box gene integrates vernalization and gibberellin signals for flowering in Arabidopsis. Plant J *35*, 613-623.

Moreau, M., Lee, G.I., Wang, Y., Crane, B.R., and Klessig, D.F. (2008). AtNOS/AtNOA1 Is a Functional Arabidopsis thaliana cGTPase and Not a Nitric-oxide Synthase. J Biol Chem *283*, 32957-32967.

Moriyasu, Y., and Inoue, Y. (2008). Use of protease inhibitors for detecting autophagy in plants. Methods Enzymol *451*, 557-580.

Mouradov, A., Cremer, F., and Coupland, G. (2002). Control of flowering time: interacting pathways as a basis for diversity. Plant Cell *14 Suppl*, S111-130.

Murashige, T., and Skoog, F. (1962). A Revised Medium for Rapid Growth and Bio Assays with Tobacco Tissue Cultures. Physiologia Plantarum *15*, 473-479.

Perkins, D.N., Pappin, D.J., Creasy, D.M., and Cottrell, J.S. (1999). Probability-based protein identification by searching sequence databases using mass spectrometry data. Electrophoresis *20*, 3551-3567.

Petty, K.J. (1996). Metal-Chelate Affinity Chromatography. Current Protocols in Molecular Biology, 10.11.10-10.11.24.

Phillips, A.R., Suttangkakul, A., and Vierstra, R.D. (2008). The ATG12-conjugating enzyme ATG10 Is essential for autophagic vesicle formation in Arabidopsis thaliana. Genetics *178*, 1339-1353.

Planchet, E., Jagadis Gupta, K., Sonoda, M., and Kaiser, W.M. (2005). Nitric oxide emission from tobacco leaves and cell suspensions: rate limiting factors and evidence for the involvement of mitochondrial electron transport. Plant J *41*, 732-743.

Polisensky, D.H., and Braam, J. (1996). Cold-shock regulation of the Arabidopsis TCH genes and the effects of modulating intracellular calcium levels. Plant Physiol *111*, 1271-1279.

Popescu, S.C., Popescu, G.V., Bachan, S., Zhang, Z., Seay, M., Gerstein, M., Snyder, M., and Dinesh-Kumar, S.P. (2007a). Differential binding of calmodulin-related proteins to their targets revealed through high-density Arabidopsis protein microarrays. Proc Natl Acad Sci U S A *104*, 4730-4735.

Popescu, S.C., Snyder, M., and Dinesh-Kumar, S. (2007b). Arabidopsis protein microarrays for the high-throughput identification of protein-protein interactions. Plant Signal Behav *2*, 416-420.

Putterill, J., Laurie, R., and Macknight, R. (2004). It's time to flower: the genetic control of flowering time. Bioessays *26*, 363-373.

Reddy, A.S. (2001). Calcium: silver bullet in signaling. Plant Sci *160*, 381-404.

Reddy, V.S., Ali, G.S., and Reddy, A.S. (2002). Genes encoding calmodulin-binding proteins in the Arabidopsis genome. J Biol Chem *277*, 9840-9852.

Reed, J.W., Nagpal, P., Poole, D.S., Furuya, M., and Chory, J. (1993). Mutations in the gene for the red/far-red light receptor phytochrome B alter cell elongation and physiological responses throughout Arabidopsis development. Plant Cell *5*, 147-157.

Rhoads, A.R., and Friedberg, F. (1997). Sequence motifs for calmodulin recognition. Faseb J *11*, 331-340.

Rice, R.H., Means, G.E., and Brown, W.D. (1977). Stabilization of bovine trypsin by reductive methylation. Biochim Biophys Acta *492*, 316-321.

Robinson, D., Galili, G., Herman, E., and Hillmer, S. (1998). Topical aspects of vacuolar protein transport: autophagy and prevacuolar compartments. J Exp Bot *49*, 1263-1270.

Rockel, P., Strube, F., Rockel, A., Wildt, J., and Kaiser, W.M. (2002). Regulation of nitric oxide (NO) production by plant nitrate reductase in vivo and in vitro. J Exp Bot *53*, 103-110.

Rose, T.L., Bonneau, L., Der, C., Marty-Mazars, D., and Marty, F. (2006). Starvation-induced expression of autophagy-related genes in Arabidopsis. Biol Cell *98*, 53-67.

Rost, B., Yachdav, G., and Liu, J. (2004). The PredictProtein server. Nucleic Acids Res *32*, W321-326.

Sancak, Y., Peterson, T.R., Shaul, Y.D., Lindquist, R.A., Thoreen, C.C., Bar-Peled, L., and Sabatini, D.M. (2008). The Rag GTPases bind raptor and mediate amino acid signaling to mTORC1. Science *320*, 1496-1501.

Sarrobert, C., Thibaud, M.C., Contard-David, P., Gineste, S., Bechtold, N., Robaglia, C., and Nussaume, L. (2000). Identification of an Arabidopsis thaliana mutant accumulating threonine resulting from mutation in a new dihydrodipicolinate synthase gene. Plant J *24*, 357-367.

Satoo, K., Noda, N.N., Kumeta, H., Fujioka, Y., Mizushima, N., Ohsumi, Y., and Inagaki, F. (2009). The structure of Atg4B-LC3 complex reveals the mechanism of LC3 processing and delipidation during autophagy. Embo J.

Scherz-Shouval, R., Shvets, E., Fass, E., Shorer, H., Gil, L., and Elazar, Z. (2007). Reactive oxygen species are essential for autophagy and specifically regulate the activity of Atg4. Embo J *26*, 1749-1760.

Schmelzle, T., Beck, T., Martin, D.E., and Hall, M.N. (2004). Activation of the RAS/cyclic AMP pathway suppresses a TOR deficiency in yeast. Mol Cell Biol *24*, 338-351.

Seligman, K., Saviani, E.E., Oliveira, H.C., Pinto-Maglio, C.A., and Salgado, I. (2008). Floral transition and nitric oxide emission during flower development in Arabidopsis thaliana is affected in nitrate reductase-deficient plants. Plant Cell Physiol *49*, 1112-1121.

Shen, S., Zhang, P., Lovchik, M.A., Li, Y., Tang, L., Chen, Z., Zeng, R., Ma, D., Yuan, J., and Yu, Q. (2009). Cyclodepsipeptide toxin promotes the degradation of Hsp90 client proteins through chaperone-mediated autophagy. J Cell Biol *185*, 629-639.

Simpson, G.G., and Dean, C. (2002). Arabidopsis, the Rosetta stone of flowering time? Science *296*, 285-289.

Singh, R., Kaushik, S., Wang, Y., Xiang, Y., Novak, I., Komatsu, M., Tanaka, K., Cuervo, A.M., and Czaja, M.J. (2009). Autophagy regulates lipid metabolism. Nature *458*, 1131-1135.

Slavikova, S., Shy, G., Yao, Y., Glozman, R., Levanony, H., Pietrokovski, S., Elazar, Z., and Galili, G. (2005). The autophagy-associated Atg8 gene family operates both under favourable growth conditions and under starvation stresses in Arabidopsis plants. J Exp Bot *56*, 2839-2849.

Slavikova, S., Ufaz, S., Avin-Wittenberg, T., Levanony, H., and Galili, G. (2008). An autophagy-associated Atg8 protein is involved in the responses of Arabidopsis seedlings to hormonal controls and abiotic stresses. J Exp Bot.

Stuehr, D.J., Santolini, J., Wang, Z.Q., Wei, C.C., and Adak, S. (2004). Update on mechanism and catalytic regulation in the NO synthases. J Biol Chem *279*, 36167-36170.

Suarez-Lopez, P., Wheatley, K., Robson, F., Onouchi, H., Valverde, F., and Coupland, G. (2001). CONSTANS mediates between the circadian clock and the control of flowering in Arabidopsis. Nature *410*, 1116-1120.

Sudhamsu, J., Lee, G.I., Klessig, D.F., and Crane, B.R. (2008). The Structure of YqeH: AN AtNOS1/AtNOA1 ORTHOLOG THAT COUPLES GTP HYDROLYSIS TO MOLECULAR RECOGNITION. J Biol Chem *283*, 32968-32976.

Sze, H., Liang, F., Hwang, I., Curran, A.C., and Harper, J.F. (2000). Diversity and regulation of plant Ca2+ pumps: insights from expression in yeast. Annu Rev Plant Physiol Plant Mol Biol *51*, 433-462.

Tanida, I., Sou, Y.-s., Ezaki, J., Minematsu-Ikeguchi, N., Ueno, T., and Kominami, E. (2004a). HsAtg4B/HsApg4B/Autophagin-1 Cleaves the Carboxyl Termini of Three Human Atg8 Homologues and Delipidates Microtubule-associated Protein Light Chain 3- and GABAA Receptor-associated Protein-Phospholipid Conjugates. J Biol Chem *279*, 36268-36276.

Tanida, I., Sou, Y.S., Ezaki, J., Minematsu-Ikeguchi, N., Ueno, T., and Kominami, E. (2004b). HsAtg4B/HsApg4B/autophagin-1 cleaves the carboxyl termini of three human Atg8 homologues and delipidates microtubule-associated protein light chain 3- and GABAA receptor-associated protein-phospholipid conjugates. J Biol Chem *279*, 36268-36276.

Thompson, A.R., Doelling, J.H., Suttangkakul, A., and Vierstra, R.D. (2005). Autophagic nutrient recycling in Arabidopsis directed by the ATG8 and ATG12 conjugation pathways. Plant Physiol *138*, 2097-2110.

Till, B.J., Reynolds, S.H., Greene, E.A., Codomo, C.A., Enns, L.C., Johnson, J.E., Burtner, C., Odden, A.R., Young, K., Taylor, N.E., *et al.* (2003). Large-scale discovery of induced point mutations with high-throughput TILLING. Genome Res *13*, 524-530.

Tsai, Y.C., Delk, N.A., Chowdhury, N.I., and Braam, J. (2007). Arabidopsis Potential Calcium Sensors Regulate Nitric Oxide Levels and the Transition to Flowering. Plant Signaling & Behavior *2*, 446-454.

Tun, N.N., Livaja, M., Kieber, J.J., and Scherer, G.F. (2008). Zeatin-induced nitric oxide (NO) biosynthesis in Arabidopsis thaliana mutants of NO biosynthesis and of two-component signaling genes. New Phytol *178*, 515-531.

Valverde, F., Mouradov, A., Soppe, W., Ravenscroft, D., Samach, A., and Coupland, G. (2004). Photoreceptor regulation of CONSTANS protein in photoperiodic flowering. Science *303*, 1003-1006.

Vardi, A., Bidle, K.D., Kwityn, C., Hirsh, D.J., Thompson, S.M., Callow, J.A., Falkowski, P., and Bowler, C. (2008). A diatom gene regulating nitric-oxide signaling and susceptibility to diatom-derived aldehydes. Curr Biol *18*, 895-899.

Wada, S., Ishida, H., Izumi, M., Yoshimoto, K., Ohsumi, Y., Mae, T., and Makino, A. (2009). Autophagy plays a role in chloroplast degradation during senescence in individually darkened leaves. Plant Physiol *149*, 885-893.

White, P.J., and Broadley, M.R. (2003). Calcium in plants. Ann Bot *92*, 487-511.

Wilkinson, J.Q., and Crawford, N.M. (1993). Identification and characterization of a chlorate-resistant mutant of Arabidopsis thaliana with mutations in both nitrate reductase structural genes NIA1 and NIA2. Mol Gen Genet *239*, 289-297.

Wilson, R.N., Heckman, J.W., and Somerville, C.R. (1992). Gibberellin Is Required for Flowering in Arabidopsis thaliana under Short Days. Plant Physiol *100*, 403-408.

Winter, D., Vinegar, B., Nahal, H., Ammar, R., Wilson, G.V., and Provart, N.J. (2007). An "electronic fluorescent pictograph" browser for exploring and analyzing large-scale biological data sets. PLoS One *2*, e718.

Wullschleger, S., Loewith, R., and Hall, M.N. (2006). TOR signaling in growth and metabolism. Cell *124*, 471-484.

Xiong, Y., Contento, A.L., and Bassham, D.C. (2007). Disruption of autophagy results in constitutive oxidative stress in Arabidopsis. Autophagy *3*, 257-258.

Yamasaki, H., and Sakihama, Y. (2000). Simultaneous production of nitric oxide and peroxynitrite by plant nitrate reductase: in vitro evidence for the NR-dependent formation of active nitrogen species. FEBS Lett *468*, 89-92.

Yang, T., and Poovaiah, B.W. (2003). Calcium/calmodulin-mediated signal network in plants. Trends Plant Sci *8*, 505-512.

Yano, K., Suzuki, T., and Moriyasu, Y. (2007). Constitutive autophagy in plant root cells. Autophagy *3*, 360-362.

Yanovsky, M.J., and Kay, S.A. (2002). Molecular basis of seasonal time measurement in Arabidopsis. Nature *419*, 308-312.

Yoshimoto, K., Hanaoka, H., Sato, S., Kato, T., Tabata, S., Noda, T., and Ohsumi, Y. (2004). Processing of ATG8s, ubiquitin-like proteins, and their deconjugation by ATG4s are essential for plant autophagy. Plant Cell *16*, 2967-2983.

Young, R.J., Beams, R.M., Carter, K., Clark, H.A., Coe, D.M., Chambers, C.L., Davies, P.I., Dawson, J., Drysdale, M.J., Franzman, K.W., *et al.* (2000). Inhibition of inducible nitric oxide synthase by acetamidine derivatives of hetero-substituted lysine and homolysine. Bioorg Med Chem Lett *10*, 597-600.

Yu, L., Strandberg, L., and Lenardo, M.J. (2008). The selectivity of autophagy and its role in cell death and survival. Autophagy *4*, 567-573.

Zeidler, D., Zahringer, U., Gerber, I., Dubery, I., Hartung, T., Bors, W., Hutzler, P., and Durner, J. (2004). Innate immunity in Arabidopsis thaliana: lipopolysaccharides activate nitric oxide synthase (NOS) and induce defense genes. Proc Natl Acad Sci U S A *101*, 15811-15816.

Zemojtel, T., Frohlich, A., Palmieri, M.C., Kolanczyk, M., Mikula, I., Wyrwicz, L.S., Wanker, E.E., Mundlos, S., Vingron, M., Martasek, P., *et al.* (2006a). Plant nitric oxide synthase: a never-ending story? Trends Plant Sci *11*, 524-525; author reply 526-528.

Zemojtel, T., Kolanczyk, M., Kossler, N., Stricker, S., Lurz, R., Mikula, I., Duchniewicz, M., Schuelke, M., Ghafourifar, P., Martasek, P., *et al.* (2006b). Mammalian mitochondrial nitric oxide synthase: characterization of a novel candidate. FEBS Lett *580*, 455-462.

Zhao, M.G., Chen, L., Zhang, L.L., and Zhang, W.H. (2009). Nitric reductase-dependent nitric oxide production is involved in cold acclimation and freezing tolerance in Arabidopsis. Plant Physiol *151*, 755-767.

Zottini, M., Costa, A., De Michele, R., Ruzzene, M., Carimi, F., and Lo Schiavo, F. (2007). Salicylic acid activates nitric oxide synthesis in Arabidopsis. J Exp Bot *58*, 1397-1405.

Appendix A1. Amino acid content in wild type and *cml* mutants.

	Amino acid content	Relative amino acid content (% of Col-0)				
	Col-0	*cml23-2*	*cml24-2*	*cml24-4*	*cml23\cml24-1*	*cml23\cml24-4*
Ala	3243	48.08*	101.91	81.00	107.36	47.00
Arg	14774	62.33	60.56	84.79	129.26	78.22
Asn	51553	73.27	74.60	70.58	112.99	76.46
Asp	2468	123.99	55.94	79.94	91.69	67.06
Cit	3661	47.81	68.13	66.51	104.28	54.21
Cys2**	0**	0**	255**	111**	509**	426**
Cyst	179	134.36	129.61	141.06	116.76	105.31
Cysteine	8538	166.15	132.42	187.16	136.29	129.35
Gln	55759	45.96	256.12	126.14	146.51	102.67
Glu	9061	101.25	81.15	77.76	99.26	74.41
Gly	747	95.11	145.01	122.91	114.20	155.93
His	937	64.62	160.51	81.54	151.81	89.11
Ile	62	214.52	72.58	92.74	108.87	83.87
Leu	63	169.84	145.24	131.75	123.81	106.35
Lys	528	87.97	62.97	61.65	136.65	83.90
Met	52	259.22	189.32	114.56	165.05	84.47
Orn	699	228.61	30.54	82.76	87.55	205.08
Phe	57	101.77	156.64	109.73	236.28	162.83
Pro	323	57.43	165.33	108.67	140.87	151.08
Ser	1516	242.51	159.63	169.43	109.70	202.80
Thr	501	130.54	4052.20	3987.33	105.09	2035.73
Tyr	545	53.49	419.63	184.50	80.28	45.60
Val	278	117.12	127.75	130.09	122.88	104.14
MetSO2	(stander) 800	100.00	100.00	100.00	100.00	100.00
Norleu	(stander) 666	104.81	110.59	107.66	102.63	105.41

*Relative amino acid changed more or less than 2 times of Col are label with red

**Absolute amino acid content

Appendix A2. Ion Accumulations in *cml23* and *cml24* mutants. Ion levels in *cml23* and *cml24* mutants were determine by ICP-MS (PiiMS, Purdue University). * P<0.05, **P<0.01.